



UNIVERSIDADE FEDERAL DE SANTA CATARINA  
CAMPUS TRINDADE  
PROGRAMA DE PÓS-GRADUAÇÃO EM ENGENHARIA MECÂNICA

Rafael Carreira Oliveira

**A NUMERICAL ANALYSIS OF THE BIOMECHANICS OF THE  
THORACOLUMBAR SPINE AND THE EFFECTS OF VERTEBRAL BODY  
TETHERING INSTRUMENTATION**

Florianópolis

2024

Rafael Carreira Oliveira

**A NUMERICAL ANALYSIS OF THE BIOMECHANICS OF THE  
THORACOLUMBAR SPINE AND THE EFFECTS OF VERTEBRAL BODY  
TETHERING INSTRUMENTATION**

Dissertação submetida ao Programa de Pós-Graduação em Engenharia Mecânica da Universidade Federal de Santa Catarina como requisito parcial para a obtenção do título de Mestre em Análise e Projeto Mecânico.

Orientador: Prof. Eduardo Alberto Fancello, Dr.  
Coorientador: Prof. Luis Fernando Nicolini, Dr.  
Coorientador: Prof. C. Rodrigo de M. Roesler, Dr.

Florianópolis  
2024

Carreira Oliveira, Rafael

A numerical analysis of the biomechanics of the thoracolumbar spine and the effects of vertebral body tethering instrumentation / Rafael Carreira Oliveira ; Orientador: Eduardo Alberto Fancello, Coorientador: Luis Fernando Nicolini, Coorientador: Carlos Rodrigo de Mello Roesler, 2024.

127 p.

Dissertação (mestrado) - Universidade Federal de Santa Catarina, Centro Tecnológico, Programa de Pós-Graduação em Engenharia Mecânica, Florianópolis, 2024.

Inclui referências.

1. Engenharia Mecânica. 2. Amarração de Corpo Vertebral . 3. Coluna. 4. Escoliose. 5. Método dos Elementos Finitos.. I. Alberto Fancello, Eduardo . II. Fernando Nicolini, Luis . III. de M. Roesler, Carlos Rodrigo IV. Universidade Federal de Santa Catarina. Programa de PósGraduação em Engenharia Mecânica. V. Título.

Rafael Carreira Oliveira

**A Numerical Analysis of the Biomechanics of the Thoracolumbar Spine and the  
Effects of Vertebral Body Tethering Instrumentation**

O presente trabalho em nível de Mestrado foi avaliado e aprovado, em 21 de junho de 2024,  
pela banca examinadora composta pelos seguintes membros:

Prof. Eduardo Alberto Fancello, Dr.  
Universidade Federal de Santa Catarina (UFSC)

Prof. Paulo de Tarso da Rocha Mendonça, Dr.  
Universidade Federal de Santa Catarina (UFSC)

Prof. Bruno Agostinho Hernandez, Dr.  
Universidade Estadual Paulista (UNESP)

Antonio Eulalio Pedrosa Araujo Junior, Dr.  
Instituto Nacional de Traumatologia e Ortopedia (INTO)

Certificamos que esta é a versão original e final do trabalho de conclusão que foi julgado  
adequado para obtenção do título de Mestre em Engenharia Mecânica.

---

Coordenação do Programa de Pós-Graduação

---

Prof. Eduardo Alberto Fancello, Dr.  
Orientador

Florianópolis, 2024.

Dedico este trabalho à minha família, que é meu tesouro,  
e às crianças, que são o tesouro do mundo.

## **AGRADECIMENTOS**

Gostaria de expressar, em primeiro lugar, minha gratidão a Deus, pela dádiva da vida e pela força concedida para superar os desafios desta jornada acadêmica. Agradeço profundamente à minha esposa, que foi meu alicerce durante o mestrado, apoiando-me incondicionalmente em cada etapa do percurso.

Minha gratidão se estende aos meus pais, cujos valores, amor e sacrifícios tornaram possível que eu perseguisse o sonho de obter o título de mestre. Agradeço ao professor Eduardo Fancello pela oportunidade de trabalhar com ele em um projeto relacionado à biomecânica e por sua orientação valiosa. Atuar na área da saúde é um sonho pessoal, e sou profundamente grato por ter tido a chance de realizar esse sonho ao contribuir para o campo da cirurgia de coluna.

Ao professor Luis Nicolini, devo meu sincero agradecimento pela orientação e amizade, que foram fundamentais para a ampliação do meu conhecimento e para a conclusão desta dissertação. Aprendi imensamente com nossa colaboração e serei eternamente grato por isso. Expresso também minha gratidão ao professor Rodrigo Roesler, cujo apoio e orientação enriqueceram minha compreensão da engenharia aplicada à saúde.

Agradeço de coração ao Marx Ribeiro, pela amizade e parceria ao longo deste projeto. Suas contribuições, tanto acadêmicas quanto pessoais, foram inestimáveis para mim.

Finalmente, minha gratidão à Universidade Federal de Santa Catarina, por proporcionar acesso gratuito ao conhecimento. A formação de excelência que obtive tanto na graduação quanto no mestrado é algo que valorizo profundamente e espero refletir em minha trajetória profissional.

“Deixai os pequeninos, e não os impeçais de vir a mim; porque dos tais é o reino dos céus.” (Bíblia [...], 2013, Mt 19, 14, p. 1484)]

## RESUMO

A amarração de corpo vertebral (Vertebral Body Tethering - VBT) é uma técnica cirúrgica emergente para o tratamento da escoliose idiopática adolescente que tem ganhado popularidade entre os cirurgiões nos últimos anos. Devido à sua relativa novidade, muitos aspectos relacionados à biomecânica da coluna instrumentada permanecem desconhecidos, e a taxa de eventos adversos, incluindo o rompimento da corda, é elevada. O compromisso entre a correção da curva escoliótica e a preservação da mobilidade da coluna do paciente é um fator crucial a ser considerado no planejamento cirúrgico. O presente trabalho tem como objetivo calibrar e validar um modelo de elementos finitos da coluna toracolombar (T10-S1) e realizar um estudo de caso para avaliar os efeitos de diferentes configurações de pré-tensão de um sistema de VBT na biomecânica da coluna. O modelo foi calibrado e validado com base em dados experimentais provenientes de testes *in vitro*. O sistema de VBT foi incorporado ao modelo, que foi submetido a flexão, extensão, flexão lateral e rotação axial com uma magnitude de 5 Nm. Os resultados indicam que a correção pós-cirúrgica e a amplitude de movimento da coluna instrumentada são, respectivamente, diretamente e inversamente proporcionais à tensão nas cordas. Além disso, a introdução da VBT na coluna gerou movimentos acoplados não naturais significativos que podem influenciar na reabilitação dos pacientes, sendo um aspecto que deve ser cuidadosamente considerado pelos fisioterapeutas no processo pós-cirúrgico. As forças desenvolvidas nas cordas durante o movimento analisado são significativamente inferiores às necessárias para ocasionar falha estática, permitindo inferir que outros mecanismos de rompimento das cordas devem estar presentes, requerendo estudos adicionais.

**Palavras-chave:** Amarração de Corpo Vertebral; Escoliose; Coluna; Método dos Elementos Finitos.



## ABSTRACT

Vertebral Body Tethering (VBT) is an emerging surgical technique for the treatment of adolescent idiopathic scoliosis that has gained popularity among surgeons in recent years. Due to its relative novelty, many aspects related to the biomechanics of the instrumented spine remain unknown, and the rate of adverse events, including tether breakage, is high. The balance between scoliosis curve correction and the preservation of the patient's spinal mobility is a crucial factor to be considered in surgical planning. This study aims to calibrate and validate a finite element model of the thoracolumbar spine (T10-S1) and conduct a case study to evaluate the effects of different pre-tension configurations of a VBT system on spinal biomechanics. The model was calibrated and validated based on experimental data from *in vitro* tests. The VBT system was incorporated into the model, which was subjected to flexion, extension, lateral bending, and axial rotation with a magnitude of 5 Nm. The results indicate that postoperative correction and the range of motion of the instrumented spine are, respectively, directly and inversely proportional to the tension in the tethers. Furthermore, the introduction of VBT in the spine generated significant unnatural coupled motion that may influence patient rehabilitation, which should be carefully considered by physiotherapists in the postoperative process. The forces developed in the tethers during the analyzed movement are significantly lower than those required to cause static failure, suggesting that other mechanisms of tether breakage must be present, requiring further studies.

**Keywords:** Vertebral Body Tethering; Scoliosis; Spine; Finite Element Method.

## RESUMO EXPANDIDO

### Introdução

A escoliose idiopática adolescente (AIS) é a deformidade de coluna mais comum em pacientes pediátricos, ocorrendo entre as idades de 10 e 18 anos. O tratamento cirúrgico é recomendado para casos severos, com curvatura superior a 45°, e o padrão ouro para esse tipo de tratamento é a fusão espinhal. No entanto, esse procedimento apresenta várias desvantagens para pacientes pediátricos, como interferência no crescimento, limitação da mobilidade e degeneração do disco intervertebral (IVD). Para evitar esses eventos adversos, técnicas alternativas estão sendo estudadas para realizar a correção cirúrgica da coluna escoliótica em casos de AIS.

A amarração de corpo vertebral (Vertebral Body Tethering - VBT) é uma técnica emergente para a correção cirúrgica de AIS, aprovada pelo FDA em 2019 e pela ANVISA em 2024. Esta técnica envolve a colocação de parafusos no lado convexo da curva escoliótica e a fixação de uma corda a esses parafusos, que, quando tensionada, corrige parte da curva. A VBT baseia-se no efeito da Lei de Hueter-Volkman, que estabelece que ossos submetidos a forças compressivas maiores tendem a crescer mais lentamente.

Embora estudos recentes indiquem que a VBT é uma técnica promissora para corrigir a AIS, a taxa de complicações é elevada devido à sua novidade. As complicações mais comuns incluem o rompimento da corda e a correção excessiva. Portanto, mais estudos são necessários para caracterizar adequadamente os efeitos da VBT na biomecânica da coluna e na recuperação dos pacientes.

### Objetivos

Os objetivos deste trabalho são calibrar e validar um modelo robusto de elementos finitos da coluna toracolombar (T10-S1) utilizando dados provenientes de ensaios *in vitro* e realizar um estudo de caso para avaliar os efeitos de diferentes configurações de pré-tensão de um sistema de VBT na biomecânica da coluna.

### Metodologia

A geometria do modelo da coluna toracolombar foi previamente obtida através de uma tomografia computadorizada de um homem saudável, com ajustes antropométricos pertinentes para representar a anatomia de um adolescente. A malha foi definida anteriormente por meio de uma análise de convergência. A calibração do modelo da coluna toracolombar foi realizada utilizando as propriedades mecânicas dos tecidos moles calibradas para o modelo L1-L2 empregado em trabalhos anteriores (NICOLINI, 2022; NICOLINI et al., 2022a; OLIVEIRA, 2022; OLIVEIRA et al., 2023). A validação final do modelo foi feita comparando os resultados numéricos com estudos *in vitro* da literatura, a fim de reduzir o viés dos resultados.

Com o modelo calibrado e validado, o implante de VBT foi inserido e as propriedades mecânicas da corda pré-tensionada foram ajustadas para representar adequadamente a realidade. Finalmente, o modelo de coluna instrumentada foi submetido a um momento de 5 Nm em flexão, extensão, rotação axial e flexão lateral. Essas simulações permitiram a obtenção de resultados sobre a correção pós-cirúrgica, preservação da amplitude de movimento (ROM), forças atuantes na corda e movimento acoplado.

## **Resultados e Discussão**

Os resultados numéricos obtidos para a coluna em flexão, extensão, rotação axial e flexão lateral estão dentro do intervalo estabelecido pelo espectro de dados do comportamento *in vitro* da coluna obtidos na literatura. Dessa forma, o modelo da coluna toracolombar foi calibrado e validado com sucesso e será utilizado em estudos futuros. Os resultados de correção pós-cirúrgica global obtidos numericamente estão entre 11° e 21°, o que está dentro do esperado, considerando os dados experimentais da literatura. Também se verificou que o aumento da pré-tensão da corda aumenta a correção da curva escoliótica.

Os resultados de ROM estiveram próximos aos obtidos na literatura, constatando-se que a mobilidade é inversamente proporcional à tensão na corda, o que está de acordo com estudos anteriores (NICOLINI et al., 2022a; 2024). Na configuração de pré-tensão mais próxima do caso clínico, verificou-se uma preservação global da mobilidade entre 60% e 80% em flexão-extensão e rotação axial, e entre 26% e 32% em flexão lateral. As forças desenvolvidas na corda durante a análise não foram suficientes para ocasionar falha estática, sugerindo que outros mecanismos estão associados ao rompimento da corda. Essa conclusão também foi alcançada por Guldeniz et al. (2023). Mais estudos são necessários para determinar com precisão o mecanismo de falha que leva ao rompimento da corda.

Os resultados deste trabalho indicam que o movimento acoplado na coluna varia de acordo com o segmento analisado, o que é coerente com as conclusões de outros estudos na literatura (SHIN et al., 2013; WIDMER et al., 2019). Além disso, constatou-se que o VBT gera movimento acoplado não natural na coluna, um fenômeno significativo para os profissionais de saúde envolvidos no processo de reabilitação de pacientes. Mais estudos são necessários para caracterizar de forma mais completa a biomecânica acoplada da coluna instrumentada com VBT. No futuro, pretende-se inserir a geometria de uma coluna escoliótica no modelo para realizar mais estudos sobre os efeitos do VBT na biomecânica da coluna. Também é necessário realizar uma análise sobre os efeitos do posicionamento dos parafusos na biomecânica da coluna instrumentada com VBT.

## **Considerações Finais**

Um modelo robusto e complexo da coluna toracolombar (T10-S1) foi calibrado e validado, e um estudo de caso sobre os efeitos do VBT na biomecânica da coluna foi realizado. A partir deste estudo, concluiu-se que os cirurgiões precisam considerar a relação inversa entre mobilidade e correção da coluna para determinar o procedimento ideal para cada paciente. Além disso, mais estudos são necessários para identificar o mecanismo de falha que leva ao rompimento da corda, e constatou-se que a instrumentação com VBT gera um movimento acoplado não natural na coluna. Os objetivos do trabalho foram atingidos, e novas possibilidades de estudo e tecnologias estão sendo exploradas para avançar o entendimento atual sobre os efeitos do VBT na coluna.

**Palavras-chave:** Amarração de Corpo Vertebral; Escoliose; Coluna; Método dos Elementos Finitos.

## LIST OF FIGURES

Figure 1 – The figure on the left shows an anterior view of the spine, displaying the numbering of each vertebra in the five regions of the spine: cervical, thoracic, lumbar, sacral, and coccygeal. The figure on the right shows a lateral view of the spine, where it is possible to see the natural curves of the spine, namely the cervical and lumbar lordosis and the thoracic and sacral kyphosis.....	21
Figure 2 – Schematic representation of the manner of measuring the Cobb angle in the spine. The Cobb angles, both of the thoracic and the lumbar curves, are measured as the angle between the lines parallel to the top of the superior end vertebra and to the bottom of the inferior end vertebra. ....	22
Figure 3 – Representations and pictures of the most common abnormal curves of the spine. a) Shows a patient with scoliosis, b) shows a patient with hyperkyphosis, and c) shows a patient with hyperlordosis. ....	23
Figure 4 – Images of a typical thoracic vertebra with the main structures signalized. a) Lateral view; b) superior view; c) inferior view. ....	24
Figure 5 – Anterosuperior view of a set IVD-vertebra with the anterior half of the IVD removed. It is possible to observe the positioning of all structures of the disc. ....	27
Figure 6 – Lateral view of the thoracolumbar spine (T11-L3) showing all ligaments and other relevant spinal structures. T11-T12 are sectioned in the midsagittal plane. ....	30
Figure 7 – Anterosuperior view of a male pelvis showing all ligaments and relevant pelvic structures. The iliolumbar ligament the only one in this region that connects with the spine at the L5 vertebra. ....	30
Figure 8 – Main motions of the spine described with an arbitrary coordinate system. ....	31
Figure 9 – Range of motion of each segment of the thoracic spine in (starting from the left) axial rotation, lateral bending, flexion, and extension.....	33
Figure 10 – Range of motion of each segment of the lumbar spine in (starting from the left) axial rotation, lateral bending, flexion, and extension.....	34
Figure 11 – Different finite element models published in literature. ....	36
Figure 12 – 3D computed tomography (CT) scan reconstruction of a severe case of scoliotic thoracic spine. ....	38

Figure 13 – Patient wearing a Charleston nighttime bending brace. ....	40
Figure 14 – AIS patient with posterior spinal fusion instrumentation. a) Preoperative radiographs showing the scoliotic curves; b) 2-year follow-up radiograph; c) Postoperative clinical photo. ....	41
Figure 15 – Representation of a scoliotic spine prior to surgery, immediately after VBT surgery, and at the 2-year postoperative follow-up. The scoliotic curve is corrected over time due to growth modulation. ....	42
Figure 16 – Thoracoscopic views of tether placement during VBT surgery. .	43
Figure 17 – Left lateral view of cadaveric samples (T10-L3) instrumented with different VBT configurations. a) single-cord construct; b) double-cord construct; c) hybrid construct. ....	46
Figure 18 – MIScoli tethering device, belonging to DePuy Spine. It shows a) the association between the anchor and screw; b) the locking screw; c) the UHMWPE tether. ....	47
Figure 19 – a) Front lateral view and b) back lateral view of the L1-L2 segment model, with all ligaments highlighted. ....	49
Figure 20 – Division of the annulus fibrosus in 25 regions to accommodate variation in the mechanical properties. Circumferentially, regions were named from A to E starting from the anterior side. Radially, they were named from 1 to 5 starting from the external surface. ....	52
Figure 21 – Thoracolumbar spine model (T10-S1) without tether. ....	54
Figure 22 – Screw positioning in the thoracolumbar spine model (T10-S1) instrumented with VBT. ....	55
Figure 23 – Thoracolumbar spine model (T10-S1) instrumented with VBT in a tension gradient configuration. The tension at the apex is higher, while it decreases as it approaches the extremities. ....	57
Figure 24 – Boundary condition of the thoracolumbar spine model (T10-S1) instrumented with VBT. The sacrum was constrained with fixed degrees of freedom. ....	58
Figure 25 – Comparison of the Moment-ROM curve of the L2-L3 and L3-L4 segments of the model with literature data in flexion-extension. ....	60
Figure 26 – Comparison of the Moment-ROM curve of the L2-L3 and L3-L4 segments of the model with literature data in axial rotation. ....	60

Figure 27 – Comparison of the Moment-ROM curve of the L2-L3 and L3-L4 segments of the model with literature data in lateral bending. ....	61
Figure 28 – Preservation of range of motion compared to the native spine when segments T10-L3 are instrumented with VBT in flexion-extension. Four different configurations of instrumentation are compared to the native spine. Negative values indicate extension and positive values indicate flexion. ....	64
Figure 29 – Preservation of range of motion compared to the native spine when segments T10-L3 are instrumented with VBT in axial rotation. Four different configurations of instrumentation are compared to the native spine. Negative values indicate right axial rotation and positive values indicate left axial rotation. ....	64
Figure 30 – Preservation of range of motion compared to the native spine when segments T10-L3 are instrumented with VBT in lateral bending. Four different configurations of instrumentation are compared to the native spine. Negative values indicate left lateral bending and positive values indicate right lateral bending. ....	65
Figure 31 – Moment-ROM curves of the T12-L1 and L1-L2 segments of the spine in different pre-tension configurations under pure lateral bending moment loading. ....	66
Figure 32 – Tether Force-ROM graphs in flexion-extension. Each graph presents all instrumented segments in a specific configuration. ....	67
Figure 33 – Tether Force-ROM graphs in axial rotation. Each graph presents all instrumented segments in a specific configuration. ....	67
Figure 34 – Tether Force-ROM graphs in lateral bending. Each graph presents all instrumented segments in a specific configuration. ....	68
Figure 35 – Coupled Axial Rotation Motion versus Flexion-Extension Moment curves of the T10-L3 and T10-S1 segments of the spine in different pre-tension configurations. ....	69
Figure 36 – Coupled Lateral Bending Motion versus Flexion-Extension Moment curves of the T10-L3 and T10-S1 segments of the spine in different pre-tension configurations. ....	69
Figure 37 – Coupled Flexion-Extension Motion versus Axial Rotation Moment curves of the T10-L3 and T10-S1 segments of the spine in different pre-tension configurations. ....	70

Figure 38 – Coupled Lateral Bending Motion versus Axial Rotation Moment curves of the T10-L3 and T10-S1 segments of the spine in different pre-tension configurations.....	70
Figure 39 – Coupled Axial Rotation Motion versus Lateral Bending Moment curves of the T10-L3 and T10-S1 segments of the spine in different pre-tension configurations.....	70
Figure 40 – Coupled Flexion-Extension Motion versus Lateral Bending Moment curves of the T10-L3 and T10-S1 segments of the spine in different pre-tension configurations. ....	71
Figure 41 – Comparison of the Moment-ROM curve of the T10-T11 and T11-T12 segments of the model with literature data in flexion-extension.....	103
Figure 42 – Comparison of the Moment-ROM curve of the T12-L1 and L1-L2 segments of the model with literature data in flexion-extension.....	103
Figure 43 – Comparison of the Moment-ROM curve of the L2-L3 and L3-L4 segments of the model with literature data in flexion-extension.....	104
Figure 44 – Comparison of the Moment-ROM curve of the L4-L5 and L5-S1 segments of the model with literature data in flexion-extension.....	104
Figure 45 – Comparison of the Moment-ROM curve of the T10-T11 and T11-T12 segments of the model with literature data in lateral bending. ....	104
Figure 46 – Comparison of the Moment-ROM curve of the T12-L1 and L1-L2 segments of the model with literature data in lateral bending. ....	105
Figure 47 – Comparison of the Moment-ROM curve of the L2-L3 and L3-L4 segments of the model with literature data in lateral bending. ....	105
Figure 48 – Comparison of the Moment-ROM curve of the L4-L5 and L5-S1 segments of the model with literature data in lateral bending. ....	105
Figure 49 – Comparison of the Moment-ROM curve of the T10-T11 and T11-T12 segments of the model with literature data in axial rotation. ....	106
Figure 50 – Comparison of the Moment-ROM curve of the T12-L1 and L1-L2 segments of the model with literature data in axial rotation. ....	106
Figure 51 – Comparison of the Moment-ROM curve of the L2-L3 and L3-L4 segments of the model with literature data in axial rotation. ....	106
Figure 52 – Comparison of the Moment-ROM curve of the L4-L5 and L5-S1 segments of the model with literature data in axial rotation. ....	107

Figure 53 – Moment-ROM curves of the T10-T11 and T11-T12 segments of the spine in different pre-tension configurations under pure flexion-extension moment loading. ....	108
Figure 54 – Moment-ROM curves of the T12-L1 and L1-L2 segments of the spine in different pre-tension configurations under pure flexion-extension moment loading. ....	108
Figure 55 – Moment-ROM curves of the L2-L3 segment of the spine and the whole instrumented spine (T10-L3) in different pre-tension configurations under pure flexion-extension moment loading. ....	109
Figure 56 – Moment-ROM curves of the T10-T11 and T11-T12 segments of the spine in different pre-tension configurations under pure axial rotation moment loading. ....	109
Figure 57 – Moment-ROM curves of the T12-L1 and L1-L2 segments of the spine in different pre-tension configurations under pure axial rotation moment loading. ....	109
Figure 58 – Moment-ROM curves of the L2-L3 segment of the spine and the whole instrumented spine (T10-L3) in different pre-tension configurations under pure axial rotation moment loading. ....	110
Figure 59 – Moment-ROM curves of the T10-T11 and T11-T12 segments of the spine in different pre-tension configurations under pure lateral bending moment loading. ....	110
Figure 60 – Moment-ROM curves of the T12-L1 and L1-L2 segments of the spine in different pre-tension configurations under pure lateral bending moment loading. ....	110
Figure 61 – Moment-ROM curves of the L2-L3 segment of the spine and the whole instrumented spine (T10-L3) in different pre-tension configurations under pure lateral bending moment loading. ....	111
Figure 62 – Moment-ROM curves of the whole thoracolumbar spine model (T10-S1) in different pre-tension configurations under pure flexion-extension moment loading. ....	111
Figure 63 – Moment-ROM curves of the whole thoracolumbar spine model (T10-S1) in different pre-tension configurations under pure axial rotation moment loading. ....	111



Figure 64 – Moment-ROM curves of the whole thoracolumbar spine model (T10-S1) in different pre-tension configurations under lateral bending moment loading. ....	112
Figure 65 – Tether Force-ROM curves of the T10-T11 segment of the spine in different pre-tension configurations under pure flexion-extension moment loading. ....	113
Figure 66 – Tether Force-ROM curves of the T11-T12 segment of the spine in different pre-tension configurations under pure flexion-extension moment loading. ....	113
Figure 67 – Tether Force-ROM curves of the T12-L1 segment of the spine in different pre-tension configurations under pure flexion-extension moment loading. ....	114
Figure 68 – Tether Force-ROM curves of the L1-L2 segment of the spine in different pre-tension configurations under pure flexion-extension moment loading. ....	114
Figure 69 – Tether Force-ROM curves of the L2-L3 segment of the spine in different pre-tension configurations under pure flexion-extension moment loading. ....	114
Figure 70 – Tether Force-ROM curves of the T10-T11 segment of the spine in different pre-tension configurations under pure axial rotation moment loading. ..	115
Figure 71 – Tether Force-ROM curves of the T11-T12 segment of the spine in different pre-tension configurations under pure axial rotation moment loading. ..	115
Figure 72 – Tether Force-ROM curves of the T12-L1 segment of the spine in different pre-tension configurations under pure axial rotation moment loading. ....	115
Figure 73 – Tether Force-ROM curves of the L1-L2 segment of the spine in different pre-tension configurations under pure axial rotation moment loading. ....	116
Figure 74 – Tether Force-ROM curves of the L2-L3 segment of the spine in different pre-tension configurations under pure axial rotation moment loading. ....	116
Figure 75 – Tether Force-ROM curves of the T10-T11 segment of the spine in different pre-tension configurations under pure lateral bending moment loading. ....	116
Figure 76 – Tether Force-ROM curves of the T11-T12 segment of the spine in different pre-tension configurations under pure lateral bending moment loading. ....	117
Figure 77 – Tether Force-ROM curves of the T12-L1 segment of the spine in different pre-tension configurations under pure lateral bending moment loading. ....	117
Figure 78 – Tether Force-ROM curves of the L1-L2 segment of the spine in different pre-tension configurations under pure lateral bending moment loading. ....	117

Figure 79 – Tether Force-ROM curves of the L2-L3 segment of the spine in different pre-tension configurations under pure lateral bending moment loading. ...	118
Figure 80 – Coupled Axial Rotation Motion versus Flexion-Extension Moment curves of the T10-T11 and T11-T12 segments of the spine in different pre-tension configurations.....	119
Figure 81 – Coupled Axial Rotation Motion versus Flexion-Extension Moment curves of the T12-L1 and L1-L2 segments of the spine in different pre-tension configurations.....	119
Figure 82 – Coupled Axial Rotation Motion versus Flexion-Extension Moment curves of the L2-L3 and L3-L4 segments of the spine in different pre-tension configurations.....	120
Figure 83 – Coupled Lateral Bending Motion versus Flexion-Extension Moment curves of the T10-T11 and T11-T12 segments of the spine in different pre-tension configurations. ....	120
Figure 84 – Coupled Lateral Bending Motion versus Flexion-Extension Moment curves of the T12-L1 and L1-L2 segments of the spine in different pre-tension configurations. ....	120
Figure 85 – Coupled Lateral Bending Motion versus Flexion-Extension Moment curves of the L2-L3 and L3-L4 segments of the spine in different pre-tension configurations.....	121
Figure 86 – Coupled Flexion-Extension Motion versus Axial Rotation Moment Coupled Flexion-Extension Motion curves of the T10-T11 and T11-T12 segments of the spine in different pre-tension configurations. ....	121
Figure 87 – Coupled Flexion-Extension Motion versus Axial Rotation Moment curves of the T12-L1 and L1-L2 segments of the spine in different pre-tension configurations.....	122
Figure 88 – Coupled Flexion-Extension Motion versus Axial Rotation Moment curves of the L2-L3 and L3-L4 segments of the spine in different pre-tension configurations.....	122
Figure 89 – Coupled Lateral Bending Motion versus Axial Rotation Moment curves of the T10-T11 and T11-T12 segments of the spine in different pre-tension configurations.....	122

Figure 90 – Coupled Lateral Bending Motion versus Axial Rotation Moment curves of the T12-L1 and L1-L2 segments of the spine in different pre-tension configurations.....	123
Figure 91 – Coupled Lateral Bending Motion versus Axial Rotation Moment curves of the L2-L3 and L3-L4 segments of the spine in different pre-tension configurations.....	123
Figure 92 – Coupled Axial Rotation Motion versus Lateral Bending Moment curves of the T10-T11 and T11-T12 segments of the spine in different pre-tension configurations.....	123
Figure 93 – Coupled Axial Rotation Motion versus Lateral Bending Moment curves of the T12-L1 and L1-L2 segments of the spine in different pre-tension configurations.....	124
Figure 94 – Coupled Axial Rotation Motion versus Lateral Bending Moment curves of the L2-L3 and L3-L4 segments of the spine in different pre-tension configurations.....	124
Figure 95 – Coupled Flexion-Extension Motion versus Lateral Bending Moment curves of the T10-T11 and T11-T12 segments of the spine in different pre-tension configurations. ....	124
Figure 96 – Coupled Flexion-Extension Motion versus Lateral Bending Moment curves of the T12-L1 and L1-L2 segments of the spine in different pre-tension configurations. ....	125
Figure 97 – Coupled Flexion-Extension Motion versus Lateral Bending Moment curves of the L2-L3 and L3-L4 segments of the spine in different pre-tension configurations.....	125
Figure 98 – Coupled Axial Rotation Motion versus Flexion-Extension Moment curve of the native L4-L5 and L5-S1 segments of the spine. ....	125
Figure 99 – Coupled Lateral Bending Motion versus Flexion-Extension Moment curve of the native L4-L5 and L5-S1 segments of the spine. ....	126
Figure 100 – Coupled Flexion-Extension Motion versus Axial Rotation Moment curve of the native L4-L5 and L5-S1 segments of the spine. ....	126
Figure 101 – Coupled Lateral Bending Motion versus Axial Rotation Moment curve of the native L4-L5 and L5-S1 segments of the spine.....	126
Figure 102 – Coupled Axial Rotation Motion versus Lateral Bending Moment curve of the native L4-L5 and L5-S1 segments of the spine.....	127

Figure 103 – Coupled Flexion-Extension Motion versus Lateral Bending  
Moment curve of the native L4-L5 and L5-S1 segments of the spine. .... 127

## LIST OF TABLES

Table 1 – Comparison of the major structural features of cervical, thoracic, and lumbar vertebrae. ....	26
Table 2 – Ligaments of the thoracolumbar spine, their positions and function. ....	29
Table 3 – Ranges of motion of the thoracic spine. ....	32
Table 4 – Ranges of motion of the lumbar spine. ....	33
Table 5 – Curve correction data of VBT surgery as reported in several studies [degrees]. The final curve is measured at least 2 years after surgery. ....	44
Table 6 – Details of the mesh for each individual structure of the thoracolumbar spine model. ....	50
Table 7 – General characteristics of the mesh for the thoracolumbar spine model. ....	50
Table 8 – Material properties of each IVD in the thoracolumbar spine model (T10-S5) considering the Holzapfel-Gasser-Ogden Hyperelastic constitutive model for the annulus fibrosus and the Hyperelastic Mooney-Rivlin model for the nucleus pulposus. ....	59
Table 9 – Immediate post-surgical correction (in degrees) of the scoliotic curve with different VBT pre-tensioning configurations for each segment of the instrumented spine and the whole thoracolumbar spine model. ....	62
Table 10 – Range of motion (in degrees) of the spine at pure moment loading of 5 Nm in flexion-extension, lateral bending, and axial rotation measured from the immediate post-surgery position. The data of the native spine has been published by Oliveira et al. (2023). ....	63
Table 11 – Maximum coupled motion (in degrees) of the spine at pure moment loading of 5 Nm in flexion-extension, lateral bending, and axial rotation measured in degrees from the immediate post-surgery position. ....	72
Table 12 – Coupled motion (in degrees) of the L4-S1 segments of the native spine at pure moment loading of 5 Nm in flexion-extension, lateral bending, and axial rotation measured in degrees. ....	74

## LIST OF ABBREVIATIONS AND ACRONYMS

AI	Artificial intelligence
AIS	Adolescent idiopathic scoliosis
ALL	Anterior Longitudinal Ligament
ANVISA	Brazilian Health Regulatory Agency
ASTM	American Society for Testing and Materials
CLL	Facet capsular ligament
FDA	U.S. Food and Drug Administration
FE	Finite Element
FEA	Finite Element Analysis
FEM	Finite Element Method
FVL	Ligamenta flava
ILL	Iliolumbar ligament
ISL	Interspinous ligament
ITL	Intertransverse ligaments
IVD	Intervertebral disc
PET	Polyethylene Terephthalate
PLL	Posterior longitudinal ligament
ROM	Range of Motion
SSL	Supraspinous ligament
SUS	Brazilian Unified Health System
UHMWPE	Ultra-high molecular weight polyethylene
VBT	Vertebral Body Tethering
WK	ASTM's Work Item

## SUMÁRIO

<b>1</b>	<b>INTRODUCTION</b> .....	<b>16</b>
1.1	MOTIVATION.....	16
1.2	OBJECTIVES.....	17
1.3	SUMMARY OF SECTIONS.....	18
<b>2</b>	<b>LITERATURE REVIEW</b> .....	<b>20</b>
2.1	ANATOMY AND CHARACTERISTICS OF THE SPINE.....	20
<b>2.1.1</b>	<b>General anatomy</b> .....	<b>20</b>
<b>2.1.2</b>	<b>Vertebral body</b> .....	<b>23</b>
<b>2.1.3</b>	<b>Intervertebral discs (IVD)</b> .....	<b>26</b>
<b>2.1.4</b>	<b>Biomechanics of the spine</b> .....	<b>31</b>
2.2	FINITE ELEMENT MODELS OF THE SPINE IN LITERATURE .....	34
2.3	SCOLIOSIS AND CONVENTIONAL TREATMENTS .....	38
2.4	VERTEBRAL BODY TETHERING .....	42
2.5	DESCRIPTION OF THE FINITE ELEMENT MODEL .....	48
<b>3</b>	<b>METODOLOGY</b> .....	<b>53</b>
3.1	GENERAL ASPECTS .....	53
3.2	CALIBRATION AND VALIDATION OF THE THORACOLUMBAR SPINE MODEL 53	
3.3	CALIBRATION OF THE PRE-TENSIONED TETHERS IN EACH TEST CONFIGURATION.....	55
3.4	SIMULATIONS OF DIFFERENT VBT CONFIGURATIONS IN THE SPINE UNDER PURE MOMENT LOADING.....	56
<b>4</b>	<b>RESULTS</b> .....	<b>59</b>
4.1	CALIBRATION AND VALIDATION OF THE THORACOLUMBAR SPINE MODEL 59	
4.2	IMMEDIATE POST-SURGICAL CURVE CORRECTION .....	61
4.3	RANGE OF MOTION .....	62
4.4	FORCES ACTING ON THE TETHER .....	66
4.5	COUPLED MOTION .....	68
<b>5</b>	<b>DISCUSSION</b> .....	<b>76</b>
5.1	LIMITATIONS AND FUTURE WORK.....	81
<b>6</b>	<b>CONCLUSION</b> .....	<b>85</b>

REFERENCES .....	87
APPENDIX A – GRAPHS PERTAINING TO THE VALIDATION OF THE THORACOLUMBAR SPINE MODEL .....	103
APPENDIX B – MOMENT-ROM GRAPHS OF THE INSTRUMENTED SPINE UNDER DIFFERENT PRE-TENSION CONFIGURATIONS .....	108
APPENDIX C – TETHER FORCE-ROM GRAPHS OF EACH SEGMENT OF THE INSTRUMENTED SPINE UNDER DIFFERENT PRE-TENSION CONFIGURATIONS .....	113
APPENDIX D – COUPLED MOTION-MOMENT GRAPHS OF EACH INDIVIDUAL SEGMENT OF THE SPINE UNDER DIFFERENT PRE-TENSION CONFIGURATIONS.....	119



## 1 INTRODUCTION

Adolescent idiopathic scoliosis (AIS) is a three-dimensional deformity of the spine characterized by a “C” or “S” shaped curve in the frontal plane. It is the most common spinal deformity, affecting children between 10 and 18 years of age (CRAMER; DARBY, 2014; HERRING, 2022; MORAMARCO et al., 2020; WEINSTEIN et al., 2021). The prevalence of AIS is between 2 and 3%, with a high probability of curve progression if left untreated. Curves higher than 30° tend to extend into adulthood (HERRING, 2022).

The current gold standard treatment for AIS is external bracing for curves smaller than 40° and spinal fusion for curves bigger than 45°, which require surgical treatment. However, these treatments present several limitations and adverse effects; thus new technologies are being developed to better treat AIS surgically (ASHER; BURTON, 2006; BAKER et al., 2020b; HERRING, 2022; KIM et al., 2008; MORAMARCO et al., 2020; O'DONNELL et al., 2023; ROACH, 1999; WEINSTEIN et al., 2001, 2021).

Vertebral Body Tethering (VBT) is a relatively new fusionless surgical approach to treating AIS. In 2019 the first VBT device was approved for sale by the U.S. Food and Drug Administration (FDA), and in 2024 it was approved in Brazil by the Brazilian Health Regulatory Agency (ANVISA). So far, VBT has shown great promise in effectively treating AIS (MARISCAL et al., 2022; RAITIO et al., 2022).

### 1.1 MOTIVATION

AIS is a serious condition among pediatric population, not only physically, but psychologically. Sanders et al. (2018) have reported that 32% of patients with AIS experience psychological and emotional distress. Moreover, current surgical practice, needed for severe cases, currently has many disadvantages that impact the patients' quality of life (O'DONNELL et al., 2023; YUCEKUL et al., 2021).

The prevalence of back pain among patients with AIS is significant, which may result in increased health care system utilization and have a negative impact on patient's physical, psychological and family well-being (THÉROUX et al., 2015). This hinders quality of life for patients and their family, while also increasing public spending with healthcare. For instance, it is reported that the direct cost of low back

pain treatment for the Brazilian Unified Health System (SUS) between 2013 and 2018 was about R\$ 24.5 million, showing an increasing trend over the years (MENDONÇA et al., 2021). A more comprehensive study revealed that the direct cost associated to the treatment of all spinal disorders for SUS in 2016 was US\$ 71.4 million (CARREGARO et al., 2018). Carregaro et al. (2020) reported that the societal cost of low back pain between 2012 and 2016 was of US\$ 2.2 billion, with productivity losses caused by work absences due to low back pain representing 79% of this amount. Total healthcare expenses were estimated to be close to US\$ 460 million. Unsurprisingly, the study concluded that these costs were excessively high, and measures needed to be taken to improve this situation.

Despite the high promise that VBT shows, currently the main problem with the technique is the high complication and revision surgery rates. One of the main adverse events is tether breakage, along with overcorrection (BIZZOCA et al., 2022; MARISCAL et al., 2022; RAITIO et al., 2022; ROSER et al., 2023; SHIN et al., 2021; VATKAR et al., 2023; ZHU et al., 2022). The mechanism of this failure is directly related to the stresses acting on the tether during the patient's daily life. Thus, it is crucial to better understand how stress levels evolve in the tether during motion so that engineers and physicians may better design and use the implant.

Oliveira (2022) has presented data on the evolution of the forces acting on the tether with motion at the L1-L2 segment of the spine. However, since this study was limited to a single segment, it is necessary to expand this understanding to include other segments while considering clinical conditions, such as the influence of adjacent instrumented segments. To the best of the author's knowledge, no more numerical studies have been conducted in which the evolution of tether forces during motion has been evaluated. Thus, this data is of great importance to further understand the effects of VBT on the biomechanics of the spine in order to properly characterize the causes of adverse events, which in turn will allow designers to develop better products and surgeons to optimize surgery parameters.

## 1.2 OBJECTIVES

This work aims to calibrate and validate a reliable model of the thoracolumbar spine and evaluate its biomechanics in both an intact state and when instrumented with different pre-tension configurations of VBT. The thoracolumbar spine model will

be used in the future for studies involving different kinds of spinal implants as well. The study encompasses a numerical evaluation of the effects of VBT on the biomechanics of different segments of the model. Thus, the following specific objectives are fulfilled:

- To calibrate and validate a reliable model of the thoracolumbar spine (T10-S1) based on experimental data from cadaveric studies;
- To evaluate the effects of different pre-tension configurations of VBT on the immediate postoperative correction, range of motion (ROM), tether force, and coupled motion of various segments of the thoracolumbar spine for flexion-extension, lateral bending, and axial rotation, comparing the results with the native spine and inferring clinical interpretation.

### 1.3 SUMMARY OF SECTIONS

This section offers a summary of what is discussed in each of the following sections.

Sections 2.1 and 2.2 mainly discuss aspects related to the anatomy of the spine, its biomechanics, and how it has been studied using the Finite Element Method (FEM), to establish a baseline of understanding regarding the features of the spine and the potential that numeric analysis has in evaluating clinical phenomena.

Section 2.3 discusses what is AIS, the state of the art regarding AIS treatment, and current trends and challenges. Section 2.4 introduces data about the efficacy of VBT surgery, including clinical results and current limitations of the technique.

Section 2.5 then makes a summary of the development of the Finite Element (FE) model and its characteristics that have already been published.

Section 3 explains the methodology adopted to perform this study, including the calibration and validation of the FE model, the calibration of pre-tensioned tether properties, and the conduction of *in silico* experiments to evaluate the effects of VBT on the biomechanics of the spine.

Section 4 presents the results of this work, including the material properties and validation curves of the thoracolumbar spine model, and the following information regarding the VBT instrumented spine: the immediate postoperative curve correction, ROM, force acting in the tether during motion, and coupled motion.

Section 5 offers a discussion on the results of this work, its limitations, and the potential for future development of VBT design in general.

Finally, Section 6 presents the conclusion of this work, along with the advancements that are in the horizon of this research group regarding the study of VBT.

## 2 LITERATURE REVIEW

The development of this study involved knowledge from a range of fields, including medicine, anatomy, continuum mechanics, and the FEM. This section provides a literature review encompassing all aspects relevant to the proper understanding of this work's development.

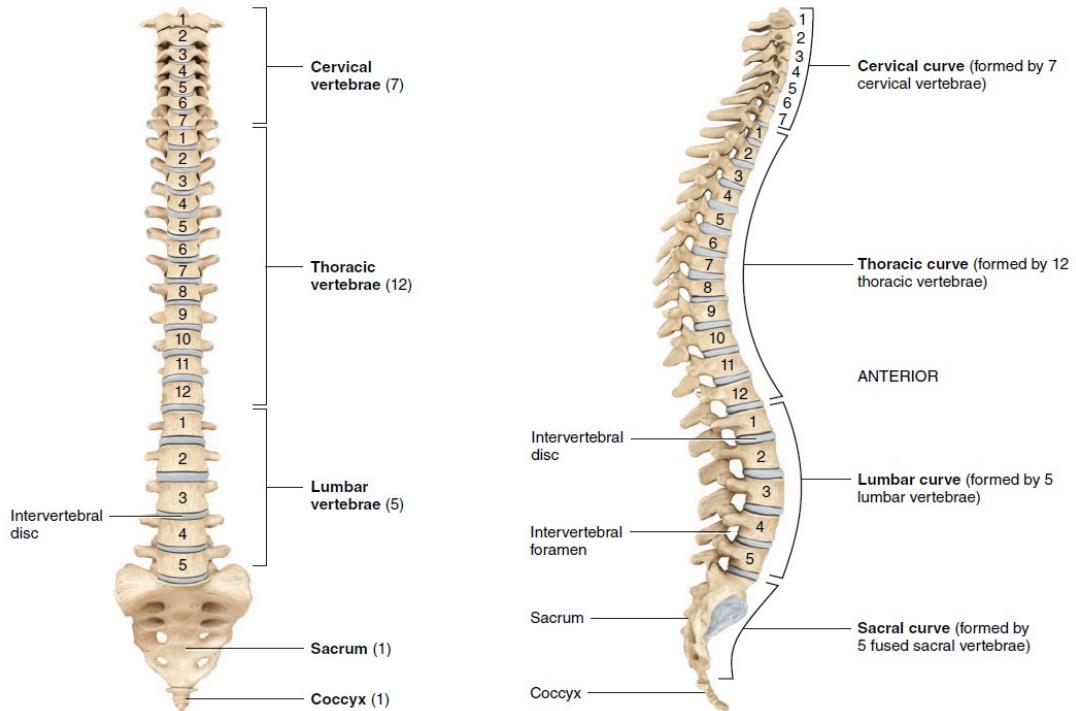
### 2.1 ANATOMY AND CHARACTERISTICS OF THE SPINE

#### 2.1.1 General anatomy

The spine is a complex structure formed by bone, joints, and ligaments in association with several muscles, nerves, and blood vessels (HALDEMAN et al., 2002; TORTORA; DERRICKSON, 2017). The purpose of the spine is to support the body, especially the head, protect the spinal cord, and provide movement to the trunk (CRAMER; DARBY, 2014).

There are 5 different regions in the spine containing different numbers of vertebrae: 7 cervical (C1-C7), 12 thoracic (T1-T12), 5 lumbar (L1-L5), 5 sacral (S1-S5), and 4 coccygeal (Co1-Co4). As the spine matures, the sacral and coccygeal vertebrae fuse together generating the sacrum and the coccyx, which are not mobile. The spine, while straight from an anterior view and bilaterally symmetric, possesses natural curves in the sagittal plane which are fully developed by age 10 – the cervical and lumbar lordosis and the thoracic and sacral kyphosis (CRAMER; DARBY, 2014; TORTORA; DERRICKSON, 2017). A lordosis is a curve which is concave to the posterior side of the body, while a kyphosis is concave to the anterior side. These curves increase the strength of the spine, help maintain balance in the upright position, absorb shocks during walking, and help protect the vertebrae from fracture (CRAMER; DARBY, 2014; TORTORA; DERRICKSON, 2017). A representation of the spine with its regions and natural curves is shown in Figure 1.

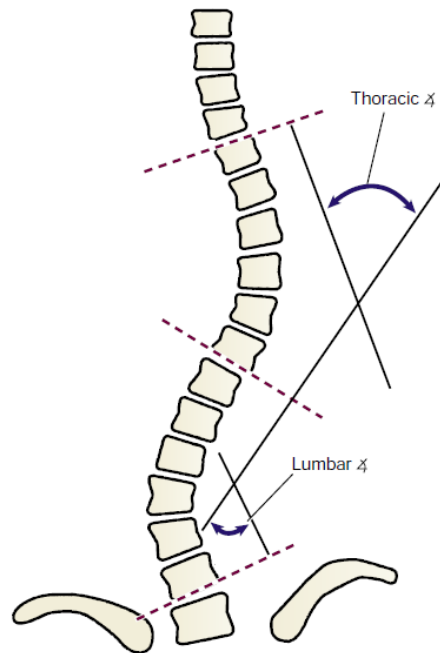
Figure 1 – The figure on the left shows an anterior view of the spine, displaying the numbering of each vertebra in the five regions of the spine: cervical, thoracic, lumbar, sacral, and coccygeal. The figure on the right shows a lateral view of the spine, where it is possible to see the natural curves of the spine, namely the cervical and lumbar lordosis and the thoracic and sacral kyphosis.



Source: Cramer and Darby (2014).

There are many methods to measure the curvature of the spine, but the most used is called the Cobb angle due to its high reproducibility and ease of application. As shown in Figure 2, Cobb angle is defined by the angle between the two straight lines that are tangent to the top endplate of the superior end vertebra of the curve and to the bottom endplate of the inferior end vertebra (FORSBERG et al., 2013; VRTOVEC et al., 2009). It is usually measured in degrees.

Figure 2 – Schematic representation of the manner of measuring the Cobb angle in the spine. The Cobb angles, both of the thoracic and the lumbar curves, are measured as the angle between the lines parallel to the top of the superior end vertebra and to the bottom of the inferior end vertebra.

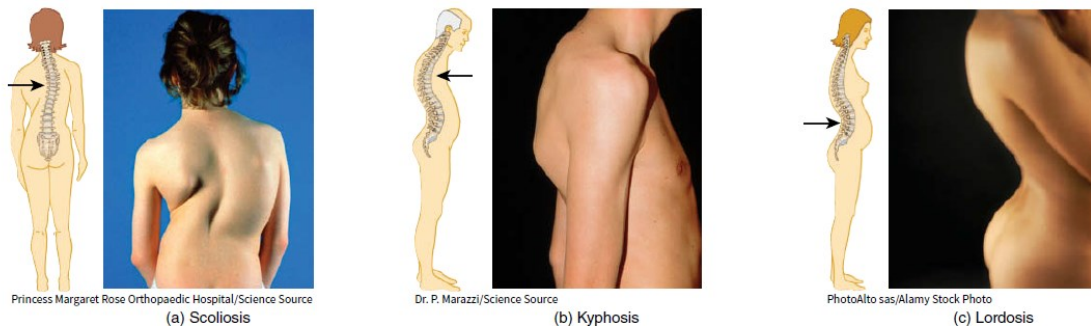


Source: Herring (2022).

There are cases where the spine presents abnormal curves. The most common types of abnormal curves are hyperkyphosis, hyperlordosis, and scoliosis (Figure 3). The normal range of thoracic kyphosis is between 20 and 40°, and hyperkyphosis is characterized by a curvature greater than that (HERRING, 2022; MAGEE; MANSKE, 2021). It includes a range of deformities, such as round back, Scheuermann's disease, humpback, and Dowager's hump. Lumbar lordosis is expected to have a curvature between 45 and 60°, and higher curves characterize hyperlordosis (WEINSTEIN et al., 2021).

Scoliosis is the most common abnormal curve of the spine and is characterized by the existence of one or two curves in the coronal plane, forming a "C" or "S" shape along with anomalies in spine alignment in the sagittal and transverse planes (MAGEE; MANSKE, 2021; MORAMARCO et al., 2020). More details about scoliosis are found in Section 2.3.

Figure 3 – Representations and pictures of the most common abnormal curves of the spine. a) Shows a patient with scoliosis, b) shows a patient with hyperkyphosis, and c) shows a patient with hyperlordosis.



Source: Tortora and Derrickson (2017).

### 2.1.2 Vertebral body

The vertebrae are composed of an outer layer of hard, compact bone, called cortical bone, and a core of softer trabecular bone, also known as cancellous or spongy bones (CRAMER; DARBY, 2014). Each vertebra is different, and they vary in size, shape, and detail, but there are some common structures between them: the vertebral body, the vertebral arch, and the seven processes that arise from the arch (TORTORA; DERRICKSON, 2017).

The vertebral body is the large disc-like anterior portion that supports the weight of the human frame. They are also the part of the vertebra which are connected to the intervertebral discs (IVDs), which form fibrocartilaginous joints (symphyses) and have the function of connecting and allowing movement between the vertebrae. The top and bottom of the vertebral bodies are known as the bony endplates, and that is where growth happens during spine maturation.

The vertebral arch is formed by the two pedicles that are projected posteriorly in the vertebra and close in an arch shape. Inside this arch is the vertebral foramen, whose function is to protect the spinal cord. Collectively, the vertebral foramina of all vertebrae form the spinal canal that contains the spinal cord.

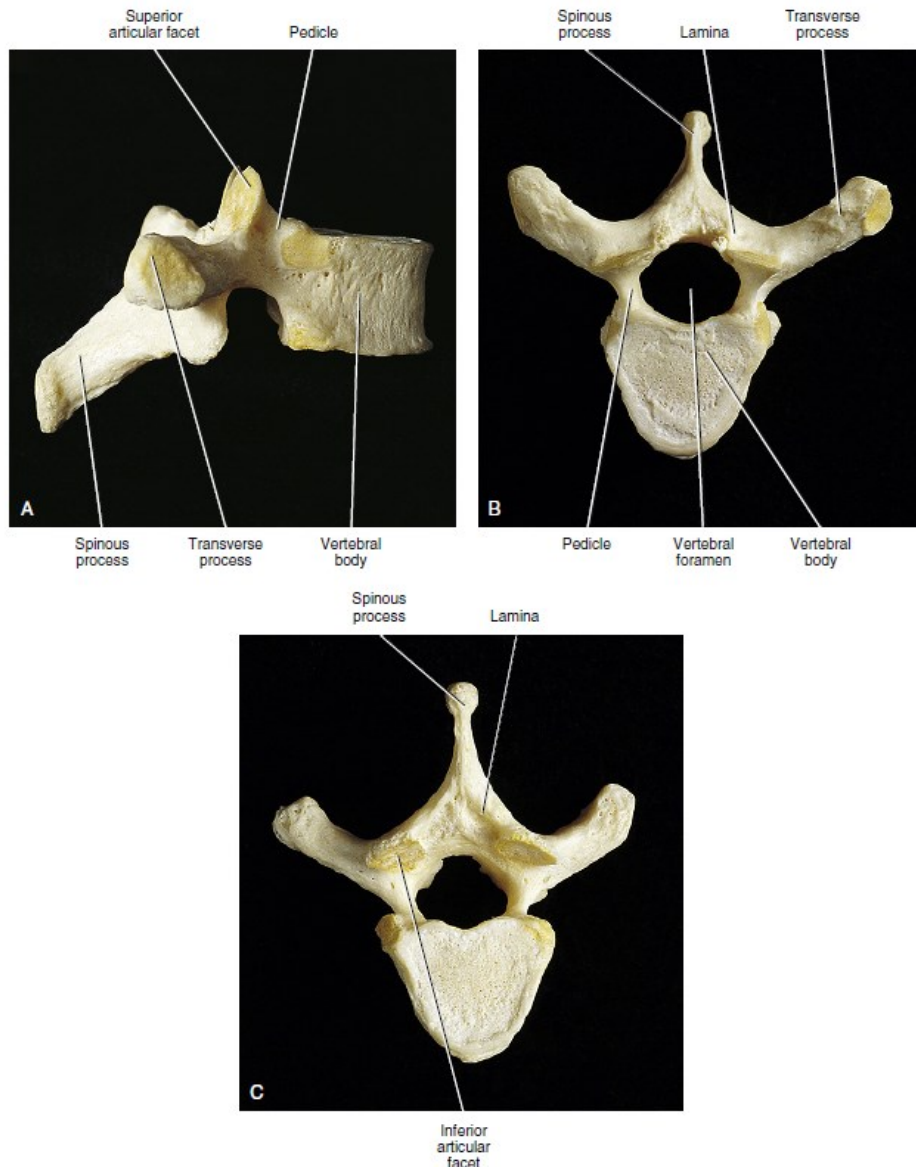
The seven processes are the two transverse processes which extend laterally, the spinous process that extends posteriorly, the two superior articular processes and the two inferior articular processes. The articular surfaces at which the superior processes of a vertebra articulate with the inferior processes of another are made of hyaline cartilage and called facet joints, or zygapophysial joints. These facet joints are symmetrical synovial-lined joints with fibrous capsule that connect the



articular facets of the vertebrae and have the functions of guiding motion of the vertebrae as well as restricting axial rotation (ALMEER et al., 2020; CRAMER; DARBY, 2014; HALDEMAN et al., 2002; TORTORA; DERRICKSON, 2017). Figure 4 shows a typical thoracic vertebra to illustrate these structures.

Figure 4 – Images of a typical thoracic vertebra with the main structures signaled.

a) Lateral view; b) superior view; c) inferior view.



Source: Cramer and Darby (2014).

Despite the common structures, vertebrae belonging to different regions of the spine are very different from each other due to the different functions and necessity for load bearing. Cervical vertebrae's main function is to house the cervical enlargement of the spinal cord while supporting and providing mobility to the head.

Thus, considering the low loads to which these vertebrae are subjected, the vertebral body are the smallest in the spine (not considering the coccygeal region), and the vertebral arch is the largest in the whole spine. Cervical vertebrae also present bifid spinous processes and two transverse foramina that allow passage for the vertebral arteries, several vertebral veins, and nerve fibers. The more unique cervical vertebrae are C1, C2, and C7, also known as Atlas, Axis, and Vertebra Prominens. C1 does not possess a vertebral body and is formed by an anterior arch and a posterior arch with large lateral masses that are connected to the transverse processes. Its function is to support the weight of the head. C2 possesses a vertebral body from which a process called dens or odontoid process extends superiorly and provides a pivot on which the atlas and the head can rotate. C7 does not present a bifid spinous process, but a longer one that can be seen and felt at the base of the head and is often used as an anatomical reference (CRAMER; DARBY, 2014; GILROY et al., 2020; TORTORA; DERRICKSON, 2017).




The thoracic vertebrae have larger vertebral bodies to support the extra load they are under when compared to the cervical vertebrae, as well as the longest spinous processes of all the regions of the spine. These vertebrae also present articular surfaces in the vertebral body to articulate with the ribs, and all but T11 and T12 – and sometimes T10 - also have costal faces that articulate with the tubercles of the ribs in the transverse processes. The attachment of the ribs to the sternum limits movement in the thoracic spine, so they are important elements to consider when studying the biomechanics of the thoracic spine (CRAMER; DARBY, 2014; TORTORA; DERRICKSON, 2017).

The lumbar vertebrae have the largest and strongest vertebral bodies of the whole spine to support the loads they are subjected to. All the processes of these vertebrae are short and thick. The intervertebral bodies grow from L1 to L3, but L4 and L5 are relatively variable in width (CRAMER; DARBY, 2014; TORTORA; DERRICKSON, 2017). Table 1 shows the main anatomical differences between the cervical, thoracic and lumbar vertebrae.

The sacrum is a large triangular bone formed by five fused sacral vertebrae. It provides a foundation for the spine and is positioned at the posterior portion of the pelvic cavity. Between S2 and S3, the female sacrum tends to be shorter, wider, and more curved than the male sacrum. The coccyx is also a triangular bone usually formed from four fused coccygeal vertebrae. It articulates superiorly with the apex of

the sacrum through a small disc of fibrocartilage. The ossification of both the sacrum and the coccyx is extremely complex due to the large number of the ossification centers in both structures. While fusion of the primary center typically occurs between 3 months and 7 years, many other ossification centers may not fuse until about 30 years of age. While assessing skeletal maturity, clinicians often use either the Risser scale, which categorizes ossification from 0 (no ossification) to 5 (full skeletal maturity), or the Sanders scale, which assesses bone growth from 1 (slow growth in early adolescence) to 8 (full skeletal maturity). These parameters are important when deciding which treatments to consider for a specific patient (CRAMER; DARBY, 2014; KIM et al., 2008; TORTORA; DERRICKSON, 2017).

Table 1 – Comparison of the major structural features of cervical, thoracic, and lumbar vertebrae.

CHARACTERISTIC	CERVICAL	THORACIC	LUMBAR
Overall structure			
Size	Small.	Larger.	Largest.
Foramina	One vertebral and two transverse.	One vertebral.	One vertebral.
Spinous processes	Slender, often bifid (C2–C6).	Long, fairly thick (most project inferiorly).	Short, blunt (project posteriorly rather than inferiorly).
Transverse processes	Small.	Fairly large.	Large and blunt.
Articular facets for ribs	Absent.	Present.	Absent.
Direction of articular facets			
Superior	Posterosuperior.	Posterolateral.	Medial.
Inferior	Anteroinferior.	Anteromedial.	Lateral.
Size of intervertebral discs	Thick relative to size of vertebral bodies.	Thin relative to size of vertebral bodies.	Thickest.

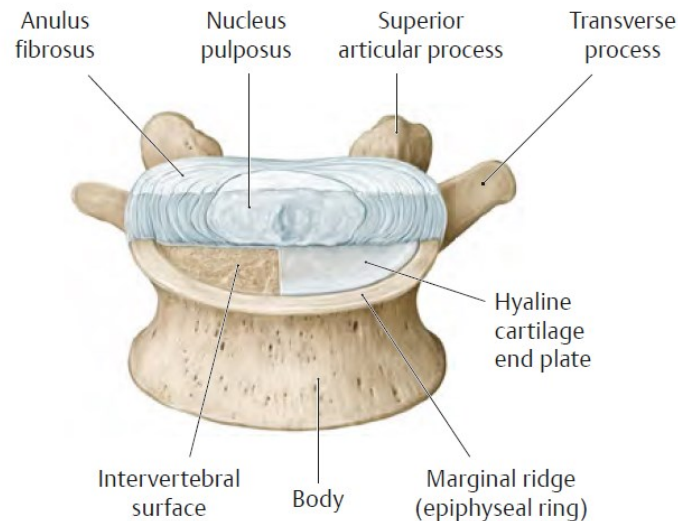
Source: Tortora and Derrickson (2017).

### 2.1.3 Intervertebral discs (IVD)

The intervertebral discs are located between the vertebral bodies, and account for 20% to 33% of the height of the spine. They are fibrocartilaginous joints (symphyses) formed of an outer fibrocartilaginous ring called annulus fibrosus, an inner gelatinous substance called the nucleus pulposus, and cartilaginous endplates located at the top and bottom. The IVDs have many functions, such as maintaining the stability between vertebrae, providing mobility to the spine, and assisting in load

bearing and shock absorption (CRAMER; DARBY, 2014; TORTORA; DERRICKSON, 2017). Figure 5 shows a representation of an intervertebral disc and its components.

Figure 5 – Anterosuperior view of a set IVD-vertebra with the anterior half of the IVD removed. It is possible to observe the positioning of all structures of the disc.



Source: Gilroy et al. (2020).

The annulus fibrosus is the ring-like structure that surrounds the IVD circumferentially. It consists of several fibrocartilaginous concentric lamellae formed by a non-fibrous matrix - the ground substance made of water, proteoglycans, and non-collagenous proteins - and aligned collagen fiber bundles. These bundles are usually oriented with a mean fiber angle of  $30^\circ$  or  $150^\circ$  in relation to the transverse plane, and these angles vary both circumferentially and radially within the annulus fibrosus. The fibrocartilaginous nature of the annulus fibrosus allows it to sustain different types of common loading related to motion and daily activities, such as compression, traction, axial rotation, lateral bending, and flexion-extension. The mechanical performance of the annulus is highly dependent on the tensile properties of its lamellae, their fibers' orientation, and the circumferential and radial gradients of these properties. Concisely, the role of the annulus fibrosus is to contribute and stabilize spinal motion, limit motion to a certain extent, act as an enclosure for the nucleus pulposus, and dampen spinal loads (CRAMER; DARBY, 2014; HOLZAPFEL et al., 2004; KOWALSKI et al., 2005; TORTORA; DERRICKSON, 2017).

The nucleus pulposus consists of a soft, viscoelastic, and highly hydrated substance. It is contained by the annulus fibrosus and the cartilaginous endplates, and its main functions are to absorb acting loads and exchange liquid between the IVD and vertebral capillaries. With age, the IVD tends to lose hydration, which leads to a loss of elasticity and hardening (CRAMER; DARBY, 2014; TORTORA; DERRICKSON, 2017; NATOUR et al., 2004). The cartilaginous endplates separate the other structures of the IVD, especially the nucleus pulposus, from the vertebral bony endplates both superiorly and inferiorly. They are made of hyaline cartilage and play a very important role in the nutrition of the disc, as it allows nutrient transport into the IVD from adjacent blood vessels (CRAMER; DARBY, 2014; MOON et al., 2013).

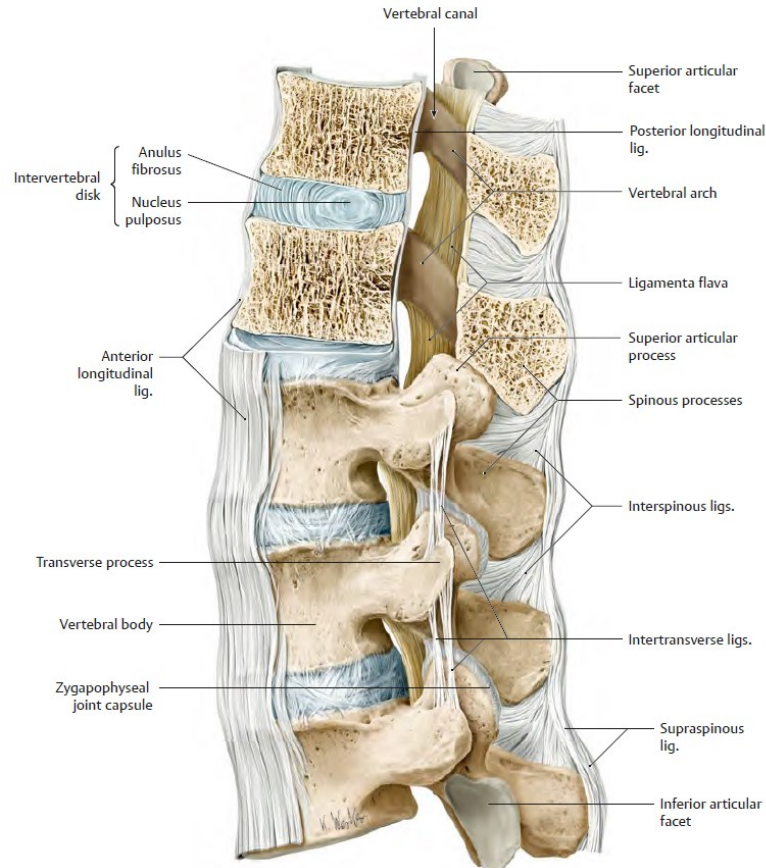
Ligaments are a type of connective tissue that attaches bone to bone. They are formed by collagen fibers aligned in parallel bundles possessing great tensile strength, providing strong attachment between bones and withstanding tension to limit excessive motion. The spinal ligaments in particular allow smooth motion of the spine within its normal ROM and help provide protection to the spinal cord by limiting excessive motion and absorbing part of the load during trauma. Stretching a ligament beyond its capacity may lead to a sprain, which is a stretched or torn ligament. Since ligaments resist tension, but not compression or loading in other directions, their functional properties depend on both the mechanical properties and positioning – namely, location and orientation – of the ligament with respect to the moving vertebrae (CRAMER; DARBY, 2014; KIM et al., 2008; TORTORA; DERRICKSON, 2017). There are many ligaments in the thoracolumbar spine, as shown by Table 2. Figure 6 and Figure 7 show representations of a segment of the thoracolumbar spine and the pelvis, pointing out each ligament.

Table 2 – Ligaments of the thoracolumbar spine, their positions and function.

<b>Ligament</b>	<b>Position</b>	<b>Function</b>
Anterior longitudinal ligament (ALL)	Anterior to the vertebral bodies throughout the whole thoracolumbar spine	Limits extension of the spine
Posterior longitudinal ligament (PLL)	Posterior to the vertebral bodies throughout the whole thoracolumbar spine	Limits flexion of the spine; may help limit posterior IVD protusion
Ligamenta flava (FVL)	Connects the laminae of adjacent vertebrae	Slows spinal flexion close to the ROM limit
Supraspinous ligament (SSL)	Connects the posterior-most aspects of the spinous processes of adjacent vertebrae	Limits flexion of the spine
Interspinous ligament (ISL)	Connects the spinous processes of adjacent vertebrae	Limits flexion of the spine
Intertransverse ligaments (ITL)	Connects the transverse processes of adjacent vertebrae	Limits contralateral lateral bending of the spine
Facet capsular ligament (CLL)	Connects the facets in each of the facet joints	Constrains synovial fluid and helps manage joint motion
Iliolumbar ligament (ILL)	Connects the iliac crest to the vertebral body and transverse processes of L5. Part of it (lumbosacral ligaments) attaches to the anterior and superior part of the sacrum.	Limits contralateral lateral bending of the spine

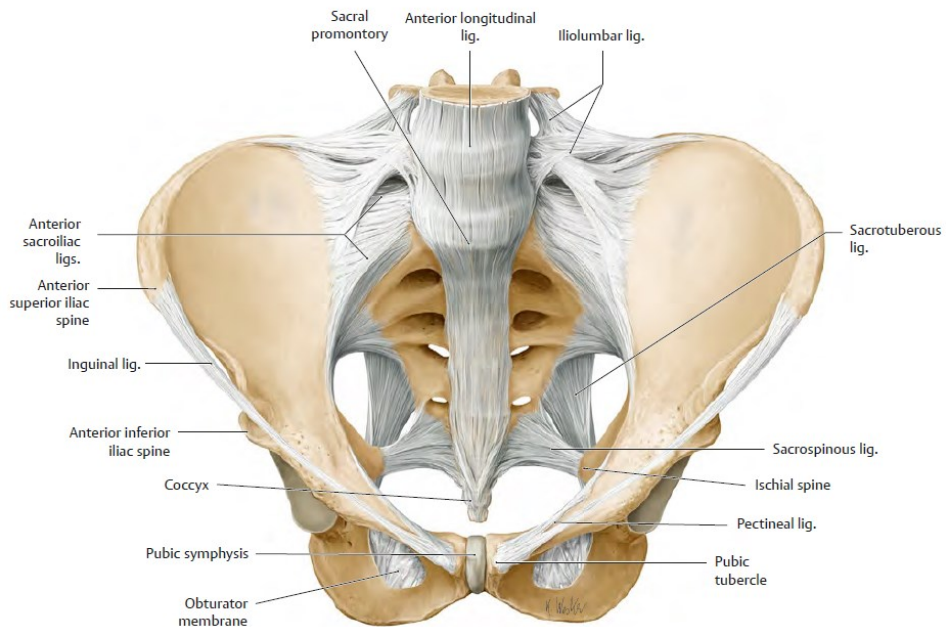
Source: Adapted from Bermel et al. (2018) and Cramer and Darby (2014).

Figure 6 – Lateral view of the thoracolumbar spine (T11-L3) showing all ligaments and other relevant spinal structures. T11-T12 are sectioned in the midsagittal plane.



Source: Gilroy et al. (2020).

Figure 7 – Anterosuperior view of a male pelvis showing all ligaments and relevant pelvic structures. The iliolumbar ligament the only one in this region that connects with the spine at the L5 vertebra.

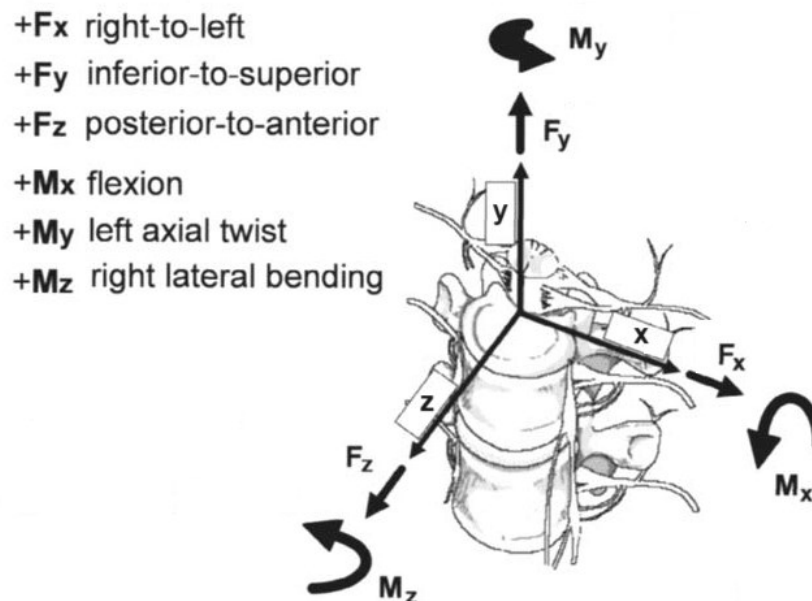


Source: Gilroy et al. (2020).

### 2.1.4 Biomechanics of the spine

Biomechanics is the science which analyzes the effects of mechanical loads on the behavior of biological tissue. The biomechanics of the spine is influenced by a series of structures, such as the IVDs, vertebrae geometry, facet joints, and ligaments. Usually, the motions of clinical and engineering interest are rotation about the frontal axis (flexion-extension), rotation about the longitudinal axis (axial rotation), and rotation about the sagittal axis (lateral bending). These motions occur due to the contraction of the muscles attached to the bony vertebrae, causing relative displacement around the joints. Several structures of the spine act to limit excessive motion and prevent injury, such as ligaments, IVDs' annulus fibrosus, and certain joints. Translational displacement along the anatomical axis can also be studied and can be extremely important in specific applications (CRAMER; DARBY, 2014; KIM et al., 2008; MORAMARCO et al., 2020; WEINSTEIN et al., 2001). Figure 8 shows the main motions of the spine in the coordinate system used in this work.

Figure 8 – Main motions of the spine described with an arbitrary coordinate system.



Source: Adapted from Kim et al. (2008).

Angular displacement in the spine is measured by its range of motion, which is the amplitude of angular motion that the spine can achieve under specific conditions.



This allows direct comparisons between the biomechanical behavior of a healthy and native spine with a pathological spine, or a spine instrumented with some type of implant or prosthesis. Many researchers study not only the kinematics of the spine, but also its kinetics, analyzing the loads and stresses acting on the spine. These stresses can be studied in all spinal structures, such as IVDs, ligaments, or joints, and they are very important in assessing the risk of pathology development, such as disc or joint degeneration and ligament strain. Spinal biomechanics is highly non-linear, which requires advanced analysis methods in order to perform accurate studies (CRAMER; DARBY, 2014; KIM et al., 2008; MORAMARCO et al., 2020; WEINSTEIN et al., 2001).

Another relevant parameter while analyzing the biomechanics of the spine is coupled motion. The main motions of the spine, namely, flexion-extension, lateral bending, and axial rotation, often are accompanied by a subtle motion about another axis. That is called coupled motion. It is very difficult to predict coupling biomechanics due to the complexity of the spinal structures and wide anatomical variety and thus there is no consensus on literature regarding the matter, but it is well established that coupled motion varies across spinal segments. Coupled motion is considered by many physiotherapists to be highly important in the decision-making process for treatment of patients, therefore it is necessary to perform further studies on the matter (CRAMER; DARBY, 2014; LEGASPI; EDMOND, 2007; SHIN et al., 2013; WIDMER et al., 2019).

The ROM of the spine is a highly important clinical parameter, and many authors in literature have studied it. Table 3 and Table 4 show the ROM of the thoracic and lumbar spines, respectively, in flexion-extension, axial rotation, and lateral bending according to two different research teams.

Table 3 – Ranges of motion of the thoracic spine.

<b>Motion</b>	<b>Mean ROM [degrees] Cramer and Darby (2014)</b>	<b>Mean ROM [degrees] Magee and Manske (2021)</b>
Flexion-Extension	Combined: 34	Flexion: 20-45 Extension: 25-45
Axial Rotation	35	35-50
Lateral Bending	15	20-40

Source: Adapted from Cramer and Darby (2014) and Magee and Manske (2021).

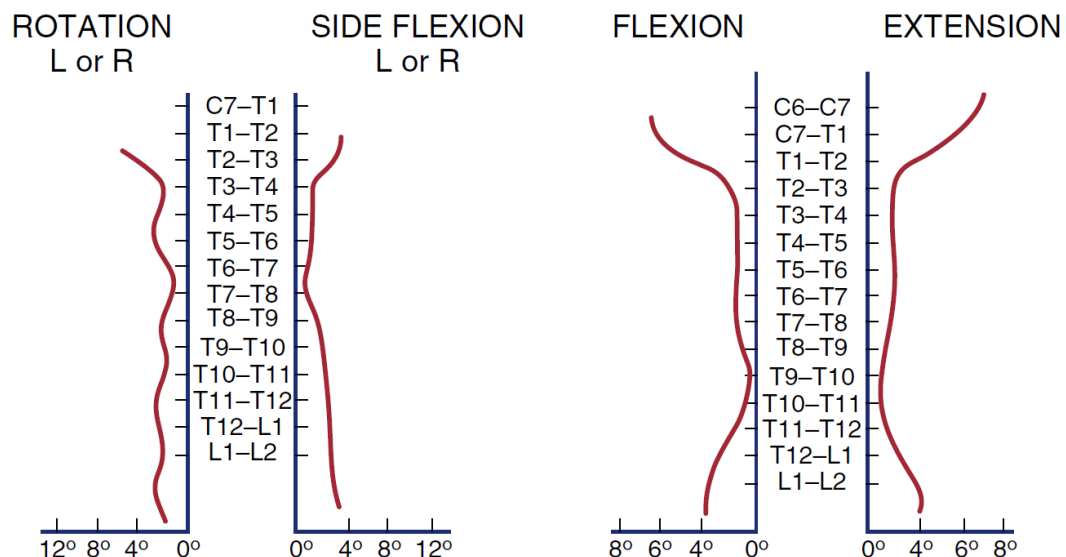
Table 4 – Ranges of motion of the lumbar spine.

Motion	Mean ROM [degrees] Cramer and Darby (2014)	Mean ROM [degrees] Magee and Manske (2021)
Flexion-Extension	Flexion: 39-60 Extension: 16-20	Flexion: 40-60 Extension: 20-35
Axial Rotation	5-15	3-18
Lateral Bending	25-30	15-20

Source: Adapted from Cramer and Darby (2014) and Magee and Manske (2021).

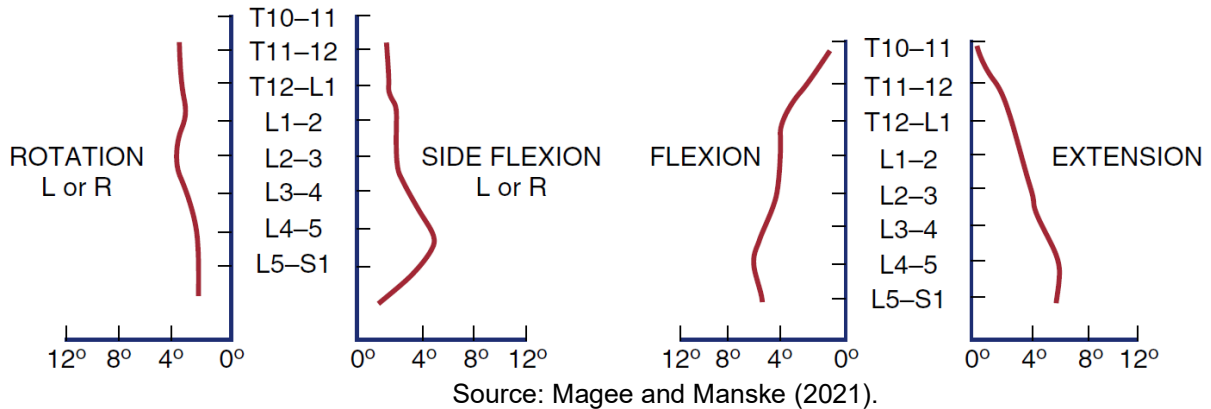
While data on the whole region of the spine is significant, often the ROM of each individual segment is important to perform a thorough biomechanical analysis. This work has researched many papers that evaluate the ROM of different spinal segments and used those results for the validation of the thoracolumbar spine model. They are presented in the Moment-ROM graphs of Section 4.1. Figure 9 and Figure 10 show the ROM for each segment of the thoracic and lumbar spines, respectively, as observed in clinical practice for flexion, extensions, lateral bending, and axial rotation.

Figure 9 – Range of motion of each segment of the thoracic spine in (starting from the left) axial rotation, lateral bending, flexion, and extension.



Source: Magee and Manske (2021).

Figure 10 – Range of motion of each segment of the lumbar spine in (starting from the left) axial rotation, lateral bending, flexion, and extension.



When dealing with pediatric patients, it is important to recognize that the immature pediatric spine presents both biomechanical and physiological differences to the adult spine. For one, it is mainly formed by soft bone and cartilage, leading to higher flexibility, not to mention continued growth (KIM et al., 2008). Weinstein et al. (2001) listed a few features that differ in the pediatric spine when compared to the adult spine: growth capacity, adaptability to applied stresses or pathologic conditions, higher malleability due to intrinsic elasticity of ligaments and modulus of bone, hypermobility, weaker endplates, changing in the spinal contour during childhood, changes in applied forces as body proportions change with growth, and immature neuromuscular control system. While practically most of these aspects may be very difficult to quantify, it is still important to keep them in mind when studying treatment techniques for pediatric patients.

## 2.2 FINITE ELEMENT MODELS OF THE SPINE IN LITERATURE

While studying biomechanics and investigating practices and products related to clinical practice, it is always ideal to conduct experimental studies *in vivo*. In other words, analyzing real patients and their characteristics that are of clinical interest. As this may not always be practical or even possible, such as cases where it is desired to understand the isolated behavior of a certain anatomical structure, cadaveric studies are considered the gold standard for biomechanical analysis (YING et al., 2023).

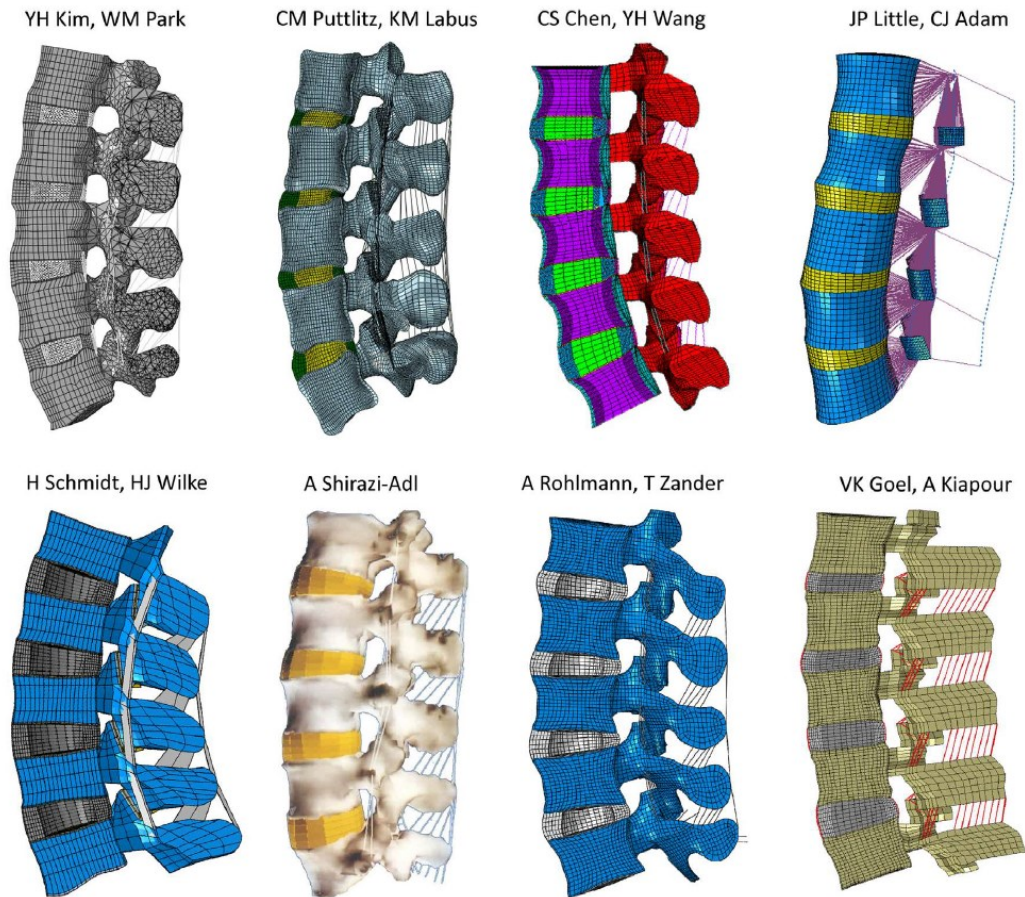
However, cadaveric studies have several limitations. The main one is the difficulty in obtaining samples that can be used in experiments. The paucity of

cadaveric samples restricts access for many research groups and limits the scope of experiments that can be conducted. For example, when a group obtains samples of cadaveric spines, they need to carefully consider which experiments they want to perform and in which order to maximize the number of tests that can be performed, since there are experiments of clinical interest that could damage the samples bringing to a halt all possible subsequent tests. There are also several requirements regarding pre-treatment and storage of cadaveric samples which must be followed to ensure reliability in scientific studies, thus increasing the cost. Ethical permissions are also required to perform this kind of study, which demands time and effort for the research team.

In this context, finite element analysis (FEA) has become an important technique to investigate the biomechanics of the human body. The finite element method is a numerical calculation technology that can approximately reproduce the biomechanical behavior of anatomical structures, including the spine. Once a finite element model is calibrated and validated based on experimental results, it can be used to perform a wide range of complex experiments *in silico* and provide guides mainly for comparative purposes. Geometries can be modeled by hand, but current software makes it possible to use CT-scan images to generate geometries for the FE model.

Several models of the spine have been created over the years. Dreischarf et al. (2014) have compared eight different published static FE models of the healthy and native lumbar spine. The constitutive models chosen for each structure differ significantly across studies. The vertebrae were modeled as either an isotropic elastic material, an anisotropic elastic material, or a rigid structure. The ground substance of the annulus fibrosus has been mostly considered a hyperelastic material, although the hyperelastic models used varied across studies as well. The nucleus pulposus was mostly modeled as an incompressible fluid, and the fibers of the annulus only resisted tension. Ligaments were largely assigned non-linear stress-strain curves, and the cartilage of the facet joints were modeled in different ways. In Dreischarf's study, all analyzed models were obtained from CT-scans, though some from living subjects and other from cadaver specimens, and with varying ages and genders (Figure 11).

Figure 11 – Different finite element models published in literature.



Source: Dreischarf et al. (2014).

Most FE models of the spine published in literature presents a similar technique to the ones shown in Figure 11. They are used for a wide variety of purposes.

Kulduk et al. (2015) used a validated model of the L3-L4 and L4-L5 segments to investigate how dynamic stabilization systems affected the biomechanics of the lumbar spine. Zhong et al. (2008; 2013) have studied whether load-controlled and displacement-controlled analyses would yield divergent results on the lumbar spine (L1-L5) when fused or with a disc replacement, as well as the way in which the method of applying preload to these constructions affect the results of the FE biomechanical analysis. Similarly, Natarajan et al. (2018) performed a FE biomechanical analysis of a long-segment fusion in the lumbar spine (L1-S1). Rohlmann et al. (2006), Little et al. (2008), Schmidt et al. (2008), and Kamal et al. (2019) have all used FEA to study specific phenomena observing either the whole lumbar spine or just segments of it. Their studies were able to, respectively, accurately estimate the trunk muscle forces for different upper body positions, better

characterize the role that osseo-ligamentous structures play in the coupled motion of the spine, explore how facet joint forces are influenced by motion, and reliably estimate intradiscal pressure and growth modulation. Ottardi et al. (2016) have also found a use to FEA by analyzing how pedicle subtraction reduction surgery affects the ROM and vertebral body forces in the lumbar spine.

Cobetto et al. (2018a, 2018b, 2018c) and Martin et al. (2023) have generated patient-specific FE models for application in surgical planning and outcome prediction for patients with AIS that underwent VBT surgery. This work is highly relevant in this field since it can be used by clinicians as a tool to better plan and execute VBT surgery, leading to better recovery for the patient.

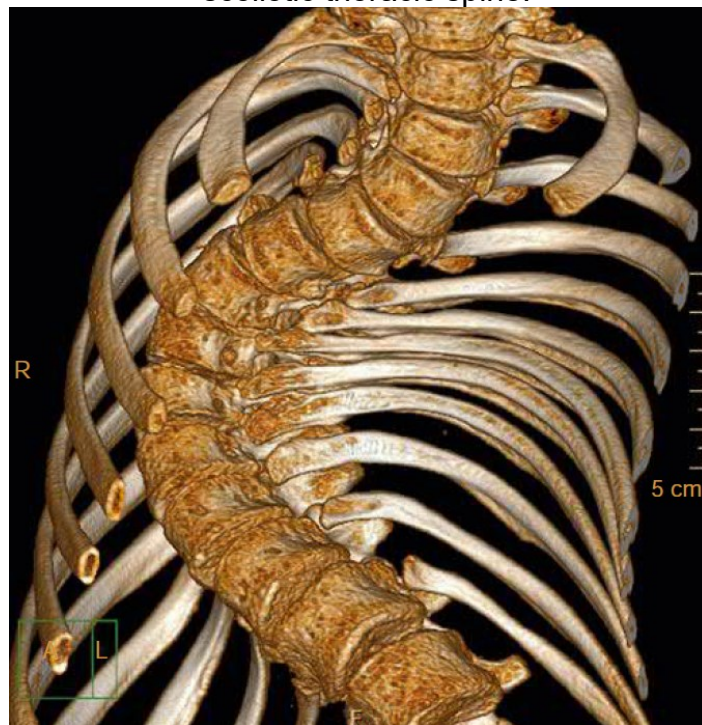
While FEA has been shown to be highly versatile in conducting biomechanical investigations in the spine, some degree of caution is required to ensure the reliability of the results. Dreischarf et al. (2014) found that the large inter-subject variability makes generalization of the results of a single model unreliable, and that a median of individual model results yields better results to estimate the response of the spine. Schmidt et al. (2006; 2007) has pointed out that oversimplification of the mechanical behavior of spinal structures and the application of mechanical properties found in literature to the model without calibration and validation, which are both common in literature, may lead to erroneous results. Schlager et al. (2018) have contributed to this discussion by performing an uncertainty analysis of the material properties of soft tissues and morphology in lumbar spine numerical models. They point out that the wide variability of this data as published in literature can lead to significant propagated errors when applied to FE models. Finally, considering how difficult calibration of a FE spine model can be due to the large number of spinal structures, Damm et al. (2019) have shown that the use of stepwise resection studies for obtaining the mechanical properties of ligaments yields more accurate results than the application of data from literature.

Concisely, a reliable FE model of the spine must be calibrated and validated using a significant amount of data, reflecting the median of different datasets as much as possible, and avoid oversimplifying the mechanical behavior of the spinal structures.

### 2.3 SCOLIOSIS AND CONVENTIONAL TREATMENTS

Scoliosis is the most common abnormal curve of the spine and is often described as a lateral curvature of the spine. However, it is actually a three-dimensional deformity that not only is characterized by the existence of one or two curves in the coronal plane, forming a “C” or “S” shape, but also by anomalies in the transverse and sagittal planes. Figure 12 shows a CT-scan of a severe case of thoracic scoliosis. Scoliosis can be found in any region of the spine, but it is most frequent in the thoracic region (HERRING, 2022; MORAMARCO et al., 2020; WEINSTEIN et al., 2021).

Figure 12 – 3D computed tomography (CT) scan reconstruction of a severe case of scoliotic thoracic spine.



Source: Herring (2022).

The curve in the coronal plane needs to have a Cobb angle of at least  $10^\circ$  to be diagnosed as scoliotic.

There are two types of scoliosis: functional and structural. Functional scoliosis is a curve without any anatomical anomaly in vertebra or disc geometry and may have many causes, such as poor posture, hysteria, nerve root irritation, inflammation, leg length discrepancy, or hip contracture. Structural scoliosis can be

genetic, idiopathic, or congenital and happens when there is an anomaly in bone shape, causing the spine's normal flexibility to be lost (HERRING, 2022; MAGEE; MANSKE, 2021; MORAMARCO et al., 2020; SHAKIL et al., 2014; WEINSTEIN et al., 2021).

Idiopathic scoliosis comprises nearly 80% of all cases of structural scoliosis. It has a prevalence between 2 and 3%, more often affecting females, but it lowers considerably if only more severe curves are considered. The probability of curve progression becomes higher when there is only a single thoracic curve than a double curve and when the Cobb angle is larger - curves higher than 30° tend to extend into adulthood. The cause of idiopathic scoliosis is still unknown, and when it occurs in patients between 10 and 18 years of age it is called adolescent idiopathic scoliosis (CRAMER; DARBY, 2014; HERRING, 2022; KIM et al., 2008; MAGEE; MANSKE, 2021; MORAMARCO et al., 2020; SHAKIL et al., 2014; WEINSTEIN et al., 2001, 2021).

There are many approaches to treating AIS. The decision on which technique to use will be taken depending on clinical parameters such as the patient's skeletal maturity, severity of the scoliotic curve, number of curves, number of scoliotic segments, patient-specific anatomic features, and the spine's flexibility. Patients with small curves, with a Cobb angle smaller than 25° will often just require periodic screening and clinical examinations to follow-up on the progression of the curve. When the scoliotic curve is between 25° and 40°, nonsurgical treatment should be considered. The most common nonsurgical treatment method for AIS is orthotic (brace) treatment, being considered the standard care in many centers (Figure 13). This method requires that patients follow a wearing schedule, and the early discontinuation of the brace will often lead the curve to return to the pretreatment level of severity. Several studies have shown that bracing is effective in skeletally immature patients whose scoliotic curves are smaller than 40°; however it is not considered to be a conservative treatment since has also been associated with some adverse events, such as pain, skin irritation, renal and pulmonary disorders, pressure sores, nerve irritation, and psychosocial issues. It is especially advised that patients are comfortable with the cosmetic appearance of the deformity and willing to follow the wear schedule rigorously, so that the effects of treatment and the mental health of the patient can be maximized (HERRING, 2022; KARAVIDAS, 2019; KIM et al.,



2008; MORAMARCO et al., 2020; NEGRINI et al., 2015; SHAKIL et al., 2014; WEINSTEIN et al., 2001, 2021).

Figure 13 – Patient wearing a Charleston nighttime bending brace.

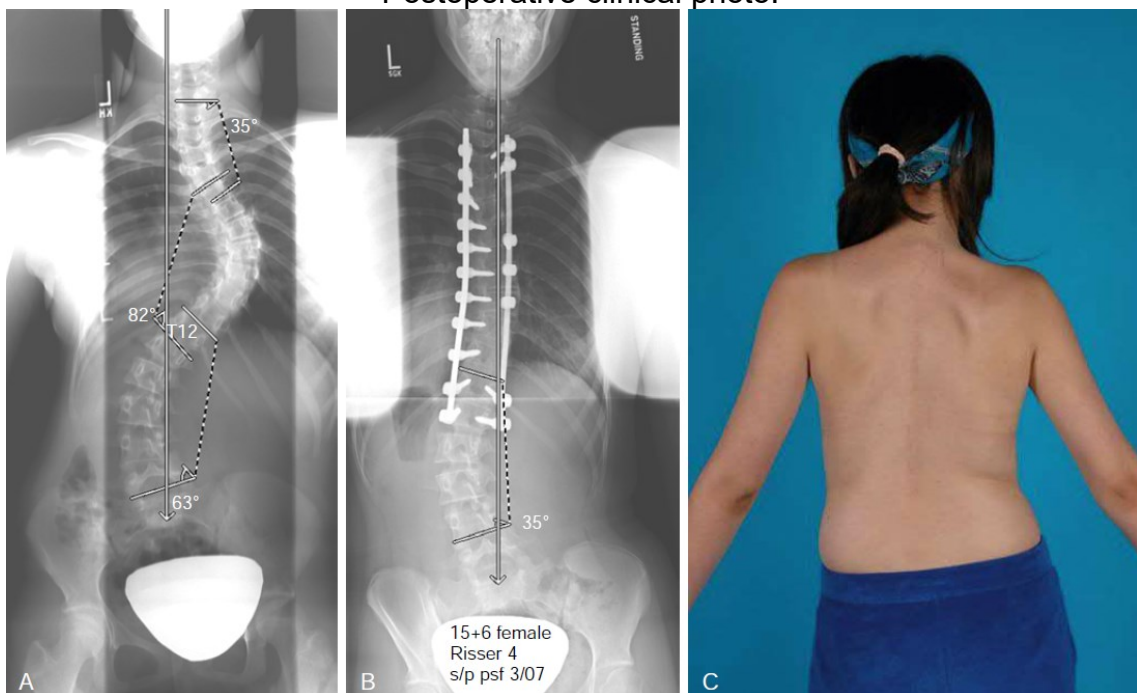


Source: Weinstein et al. (2021).

Surgical treatment is recommended when dealing with scoliotic curvatures greater than 40°. Weinstein et al. (2008) have explained that the primary objectives of AIS correction surgery are to arrest curve progression, achieve maximum permanent correction of the deformity, improve cosmetic appearance, and keep short-term and long-term complications to a minimum. The gold standard of AIS surgical treatment is posterior spinal fusion, although the anterior approach and other surgical techniques may also be utilized. Spinal fusion, or arthrodesis, is performed by anchoring screws to the scoliotic vertebrae, and then attaching one or two metallic rods to the screw heads (Figure 14). This setup constrains relative displacement between instrumented vertebrae, leading to curve correction. Despite the proven success in curve correction across the years, a range of adverse events associated with spinal fusion are reported in literature, especially in the treatment of AIS. Some

of them are growth and mobility limitation, loss of lumbar lordosis, higher risk of long-term degenerative disc disease, and higher rates of degenerative events in other structures of the unfused distal levels. These adverse events are counterproductive to the primary goals of AIS correction surgery, and thus new surgical approaches are being explored to provide better solutions (ASHER; BURTON, 2006; BAKER et al., 2020b; HERRING, 2022; KIM et al., 2008; MORAMARCO et al., 2020; O'DONNELL et al., 2023; ROACH, 1999; WEINSTEIN et al., 2001, 2021).

Figure 14 – AIS patient with posterior spinal fusion instrumentation. a) Preoperative radiographs showing the scoliotic curves; b) 2-year follow-up radiograph; c) Postoperative clinical photo.



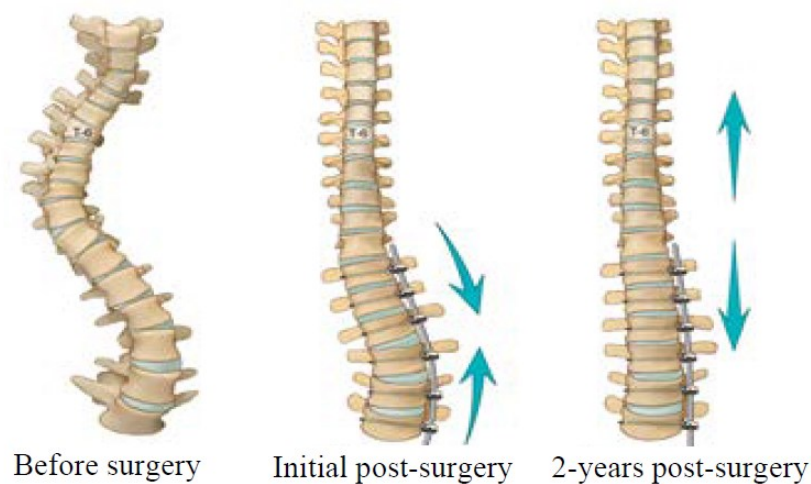
Source: Herring (2022).

The limitations of the spinal fusion surgical techniques have led researchers to explore fusionless surgical techniques to correct AIS. These techniques include growing rods, whose goal is to achieve and maintain correction during the subsequent growing period while avoiding definitive fusion of the spine, and growth modulating techniques using staples or flexible tethering elements (KIM et al., 2008; MACKEY et al., 2021; PHILLIPS et al., 2019; WEINSTEIN et al., 2021).

## 2.4 VERTEBRAL BODY TETHERING

Vertebral Body Tethering is a fusionless surgical technique that aims to treat AIS while avoid the intrinsic adverse events of spinal fusion. It consists of placing anchors and screws in convex side of the scoliotic curve and attaching a polyethylene terephthalate (PET) fiber tether to the screw heads while tensioning it (Figure 15). The correction of the scoliotic curve is directly proportional to the tension applied to the tether during surgery (BAKER et al., 2020b; NICOLINI et al., 2022a, 2024). Crawford and Lenke (2010) were the first to describe and perform this surgical technique, and still today much is being studied to optimize the surgical procedure and the device design. The FDA approved its first VBT device in 2019, while ANVISA approved the same device in 2024. Despite the novelty of this technology, Baroncini et al. (2020) found that VBT has a rapid learning curve, which means that the surgical procedure will soon be optimized for patient well-being.

Figure 15 – Representation of a scoliotic spine prior to surgery, immediately after VBT surgery, and at the 2-year postoperative follow-up. The scoliotic curve is corrected over time due to growth modulation.

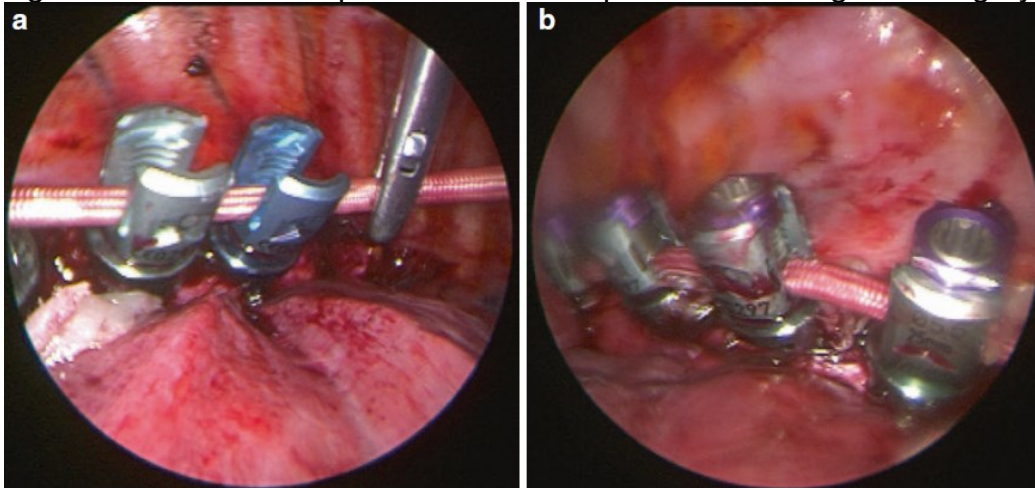


Source: Baker et al. (2020b).

The Hueter-Volkman principle states that skeletal growth is inhibited by increased mechanical compression and accelerated by decreased compressive loading. VBT relies on this principle to provide increasing curve correction across time, since the tensioning of the tether will create a stress gradient in the bony endplates of the vertebrae in a way that the convex side will be under higher compression than the concave side, causing the concave side to grow faster which

corrects vertebral wedging and, consequently, the scoliotic curve. Since VBT relies so heavily on spinal growth, this technique is indicated for surgery on skeletally immature patients with scoliotic curves between 35° and 65°. VBT is implanted using minimally invasive surgical procedures, such as the thoracoscopic technique (Figure 16) for example, and therefore does not incapacitate the patient for a long time. In fact, patients are usually able to return to all daily living activities within 6 weeks (BAKER et al., 2020b; BARONCINI et al., 2021a; PARENT; SHEN, 2020; PHILLIPS et al., 2019; VILLEMURE; STOKES, 2009).

Figure 16 – Thoracoscopic views of tether placement during VBT surgery.



Source: Phillips et al. (2019).

Several meta-analyses have been conducted to evaluate the performance of VBT as a safe and effective surgical technique to correct AIS. These meta-analyses compiled clinical data on the outcomes of VBT surgeries in several studies, and the results regarding curve correction are presented in Table 5.

Table 5 – Curve correction data of VBT surgery as reported in several studies [degrees]. The final curve is measured at least 2 years after surgery.

Study	Mean Preoperative Curve	Mean Final Curve
Abdullah et al., 2021	51.2	27.5
Alanay et al., 2020	47	17
Baker et al., 2020a	45	20
Baroncini et al., 2021b	52.4	26.6
Bernard et al., 2022	56.5	19.4
Cebeci et al., 2017	46	18
Costanzo et al., 2022	56.5	37
Hedge et al., 2021	52	15.3
Hoernschemeyer et al., 2020	50	9
Mackey et al., 2021	50	28
Miyanji et al., 2020	51	23
Mladenov and Stucker, 2021	46.5	23
Newton et al., 2018	52.7	27.4
Newton et al., 2020	53	33
Pehlivanoglu et al., 2020	48.2	10.1
Rushton et al., 2021	50.8	25.7
Samdani et al., 2014b	44	13.5
Wong et al., 2019	40.1	25
Yucekul et al., 2021	46	12

Source: Adapted from Bizzoca et al. (2022), Mariscal et al. (2022), Raitio et al. (2022), Roser et al. (2023), Shin et al. (2021), Vatkar et al. (2023), and Zhu et al. (2022).

The literature data makes it evident that VBT is effective in correcting the scoliotic curve, though not as much than spinal fusion. VBT has also been shown to outperform spinal fusion in some respects. For example, Yucekul et al. (2021) have examined VBT patients and found that, at a mean of 29 months, there was no disc and facet joint degeneration, which is one of the possible complications with spinal fusion. O'Donnell et al. (2023) evaluated patients that underwent VBT surgery or posterior spinal fusion for 6 weeks and concluded that in that period VBT patients experienced less pain, better mobility, and faster recovery than fusion patients. All this evidence indicates that VBT is indeed a very promising surgical approach to treating AIS.

However, current VBT surgical technique and design presents a few disadvantages due to its novelty. All the meta-analyses on the efficacy of VBT found by the author indicate that the complication rate is high (values between 18% and 52.17%). The most common adverse events associated with the complications are tether breakage (4.9% - 21.9%), overcorrection (6.75% - 14.34%), and pulmonary complications such as atelectasis, pleural effusion, pneumothorax, and pneumonia

(4.8% - 9.72%). The reoperation rate is also high (between 10.1% and 15.8%), and there were patients that needed to convert to spinal fusion (between 5% and 11%). Posterior spinal fusion has a reoperation rate of about 1.8%, thus there is still much to be improved in current VBT surgery and design (BIZZOCA et al., 2022; MARISCAL et al, 2022; RAITIO et al., 2022; ROSER et al., 2023; SHIN et al., 2021; VATKAR et al., 2023; ZHU et al., 2022).

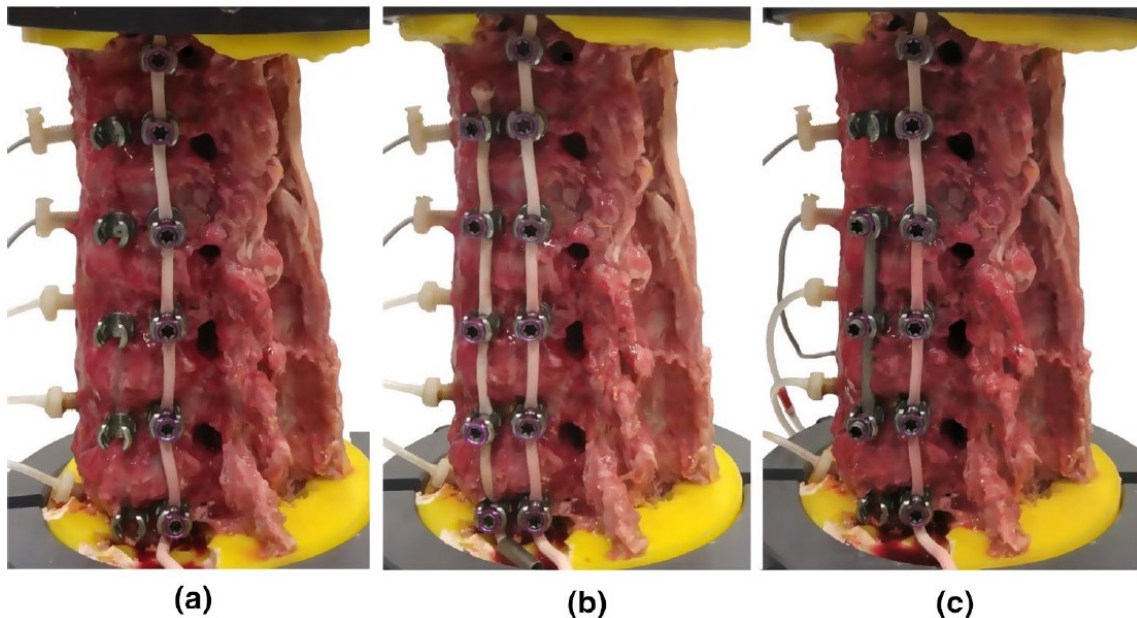
As discussed previously, literature data indicates that the most common complications associated with VBT surgery are tether breakage and overcorrection. Baroncini et al. (2022) investigated the risk factors that increase the rate of tether breakage within one year after surgery, and found that high curve magnitude, limited spine flexibility, and limited curve correction are the main risk factors. It is important to note that stiffer, more severely curved, or slowly correcting spines require maintaining higher tether tension for prolonged periods. Guldeniz et al. (2023) has performed tensile tests on single unit VBT samples and found that failure occurred by slippage at the screw-tether junction. This suggests that tether breakage may be related to stress concentration and damage at the screw-tether junction. However, more scientific data is required before achieving a proper characterization of the failure mechanism of tether breakage.

Overcorrection also is related to tether tension since it directly influences stresses in the vertebrae and, by the Hueter-Volkmann's principle, growth modulation is directly affected by these stresses. There have been attempts to develop methods to predict spinal correction based on surgical parameters. Cobetto et al. (2018b) have developed a planning tool based on patient-specific FE models incorporating spinal growth. The results were encouraging, as the predicted corrections were close to the one observed clinically.

The high rate of complications and limited indications of use have led health professionals to seek alternative surgical approaches using VBT principles and hardware. Trobisch et al. (2023) have used cadaveric tests to investigate the differences in spine mobility using larger diameter single-cord constructs or double-cord constructs. Both configurations aim to reduce tension in the tether, which in theory would minimize the risk of tether breakage while maintaining correction. They found that spinal mobility was not significantly influenced by change in single-cord construct tether diameter, but it was decreased with double-cord construct. Nicolini et al. (2021) has also conducted cadaveric studies on the human spine instrumented

with three different configurations: single-cord construct, double-cord construct, and a hybrid construct (instrumented with one tether and a titanium rod attached to part of the segment). Such study showed that motion was best preserved with a single-cord construct, and the hybrid construct showed the least mobility preservation in the segment attached to the rod.

Figure 17 – Left lateral view of cadaveric samples (T10-L3) instrumented with different VBT configurations. a) single-cord construct; b) double-cord construct; c) hybrid construct.

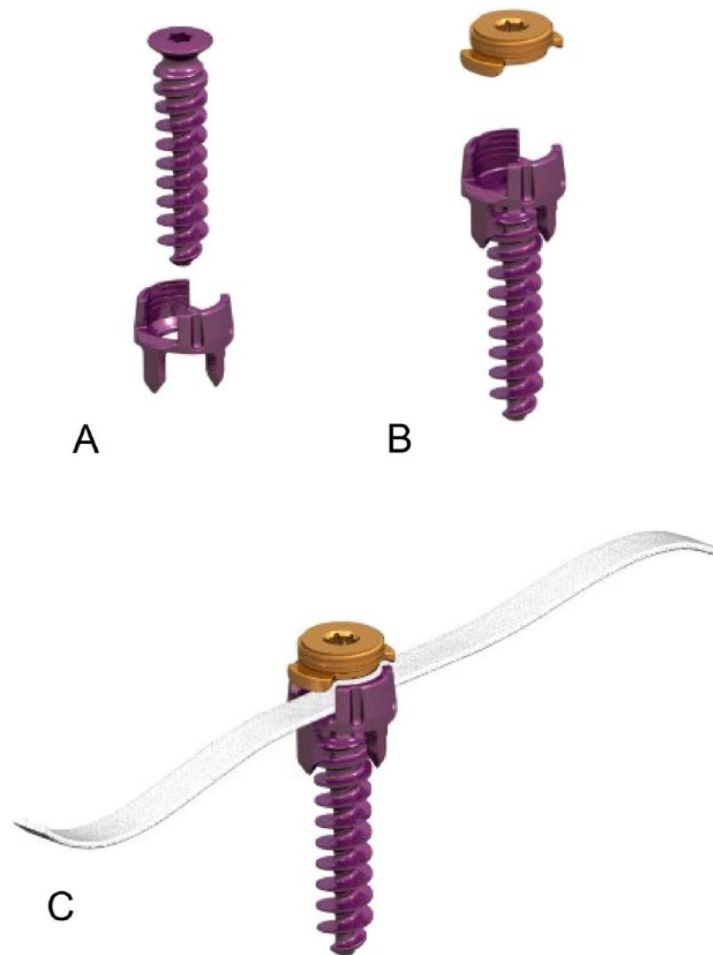


Source: Nicolini et al. (2021).

Other alternatives to traditional single-cord VBT are also being explored. Wong et al. (2019) have evaluated a new device that replaces the PET tether with braided ultra-high molecular weight polyethylene (UHMWPE) tether, but the results of this first study were not encouraging regarding curve correction and growth modulation. Boudissa et al. (2017) have proposed a new approach that combines the use of a PET synthetic ligament (tether) with staples instead of anchors and screws to introduce growth modulation to the scoliotic spine. This first study demonstrated that the device was able to halt progression of the curve during growth spurt. Antonacci et al. (2021, 2022) has developed a technique that uses the hardware of VBT coupled with releasing techniques of the ALL and annulus fibrosus in the instrumented segment as needed. They claim their technique can correct curves with Cobb angle greater than  $65^\circ$ , with greater stiffness, and can even be used to correct skeletally mature spines. More clinical evidence is required before such claims can

be effectively proven, but it shows the versatility and potential that VBT has for evolution.

Figure 18 – MIScoli tethering device, belonging to DePuy Spine. It shows a) the association between the anchor and screw; b) the locking screw; c) the UHMWPE tether.



Source: Wong et al. (2019).

In response to the growing need for standardized testing methods to validate the design of VBT device assemblies prior to commercialization, the American Society for Testing and Materials (ASTM) is developing a Work Item (WK) – which is a proposed new standard. The WK, designated as ASTM WK90586, introduces new test methods specifically for VBT implant applications. These tests aim to rigorously assess the structural integrity and mechanical properties of the devices and include:

- Static tensile test.
- Dynamic tensile (fatigue) test.
- Tensile creep and stress relaxation test.



The static and dynamic tensile tests are crucial for evaluating the structural integrity of VBT devices, enabling manufacturers to benchmark their products against competitors and confirm their safety. The tensile creep and stress relaxation test addresses the behavior of polymeric tethers under continuous stress, which can lead to creep deformation and subsequent loss of tension. This phenomenon is critical as it could compromise the long-term effectiveness of curve correction in patients, potentially resulting in undercorrection.

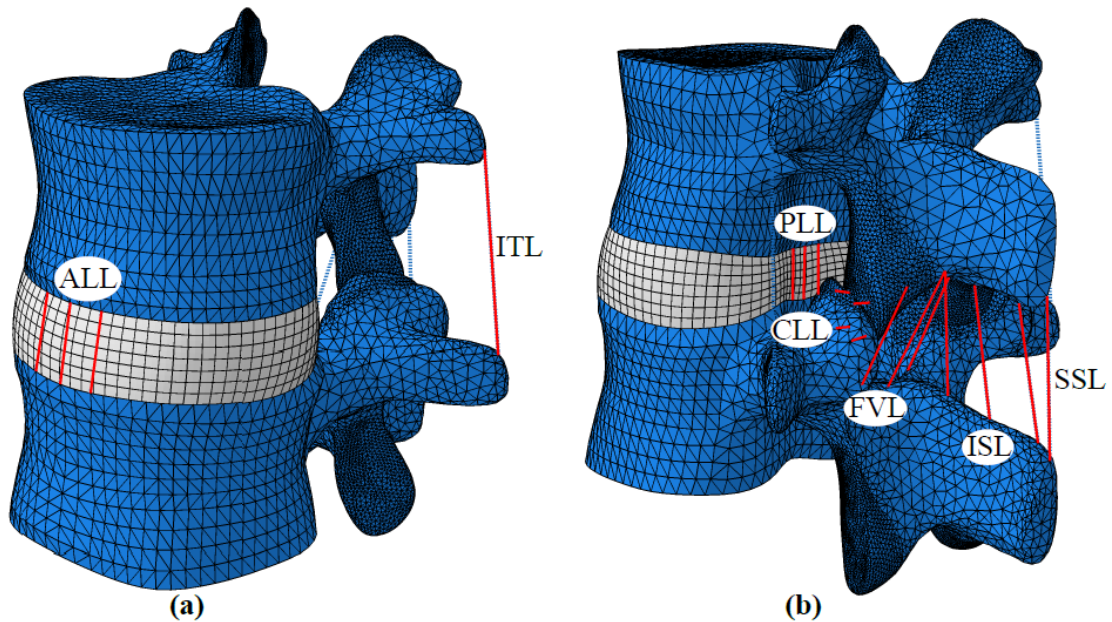
Despite the critical nature of these effects, studies examining creep and stress relaxation in VBT devices remain scarce. The development of ASTM WK90586 not only underscores the increasing adoption of VBT surgery by spine surgeons but also represents the first concerted effort to standardize pre-clinical testing methods for these devices. By standardizing these tests, ASTM WK90586 provides methods to more comprehensively evaluate the safety and efficacy of VBT device assemblies, directly contributing to improved clinical outcomes.

## 2.5 DESCRIPTION OF THE FINITE ELEMENT MODEL

The FE model used in this work is an extension of that presented by Nicolini et al. (2022a, 2024), Oliveira (2022) and Nicolini (2022), shown in Figure 19.

The geometry of the thoracolumbar spine model (T10-S1) of a healthy man, obtained from a CT-scan, was commercially acquired and went through an anthropometric adaptation to better represent the spine of a young man. The process was extensive, considering literature data to ensure compliance of the model with the anatomy of the human body.

Figure 19 – a) Front lateral view and b) back lateral view of the L1-L2 segment model, with all ligaments highlighted.



Source: Nicolini (2022).

The model was developed using ABAQUS software. All bony structures were meshed with linear tetrahedral elements for the trabecular bone and vertebral volumes covered by linear shell elements with 0.29 mm thickness to represent the cortical bone. Mesh refinement was performed at the most complex geometries and regions of interest, such as the facet joints.

The IVDs were meshed with quadratic hexahedral elements in order to better capture its complex behavior and provide more reliable results. Ligaments were modeled as 2-node spring elements without pre-tension in the neutral position. Table 6 shows details about the mesh of individual structures of the model, while Table 7 presents the general information for the whole model.

Table 6 – Details of the mesh for each individual structure of the thoracolumbar spine model.

Spinal Structure	Element Type	Element count	Node count
Trabecular bone of the vertebral bodies	C3D4: 4-node linear tetrahedron	9342	2416
Cortical bone of the vertebral bodies	S3: 3-node linear shell	1267	731
Posterior elements of vertebrae	C3D4: 4-node linear tetrahedron	29,612	8051
Sacrum	C3D4: 4-node linear tetrahedron	33924	8921
Intervertebral discs	C3D20H: 20-node quadratic brick and hybrid	5,747	26559
Ligaments	CONN3D2: connector element of two nodes and unidimensional resistance	1 to 3 elements for each ligament	2 nodes for each element

Source: Nicolini (2022).

Table 7 – General characteristics of the mesh for the thoracolumbar spine model.

Parameter	Quantity
Element S3: 3-node linear shell	10,140
Element C3D4: 4-node linear tetrahedron	486,345
Element C3D20H: 20-node quadratic brick and hybrid	45,979
Total Elements	542,464
Total Nodes	335,614

Source: Author.

The IVD mesh was chosen through a mesh convergence analysis considering not only ROM, but also pressure and *von Mises* stress at the center of the IVD. The mesh size at the bony structures was set with the main objective of good reproduction of the shape of the components, and its quality has little effect on the motion of the spine if compared to the soft tissues due to its comparatively high stiffness. All bony structures were modeled as linear elastic materials with data from literature. Since they influence motion very little in this analysis, there was no need for a more complex model and calibration. Ligaments were modeled as non-linear spring elements that resist only tension. The facet joints were modeled as soft frictionless contact that only transmits compressive forces.

The IVDs' nucleus pulposus was modeled as a Mooney-Rivlin incompressible hyperelastic material, whose strain-energy density function is presented in Equation 1.  $C_{10n}$  and  $C_{01n}$  are material properties intrinsic to the model,  $D_n$  is a variable related

to volume change,  $I_1$  and  $I_2$  are invariants of the right Cauchy-Green deformation tensor, and  $J$  is the Jacobian of the deformation.

$$W_n = C_{10n} (I_1 - 3) + C_{01n} (I_2 - 3) + \frac{1}{D_n} (J - 1)^2 \quad (1)$$

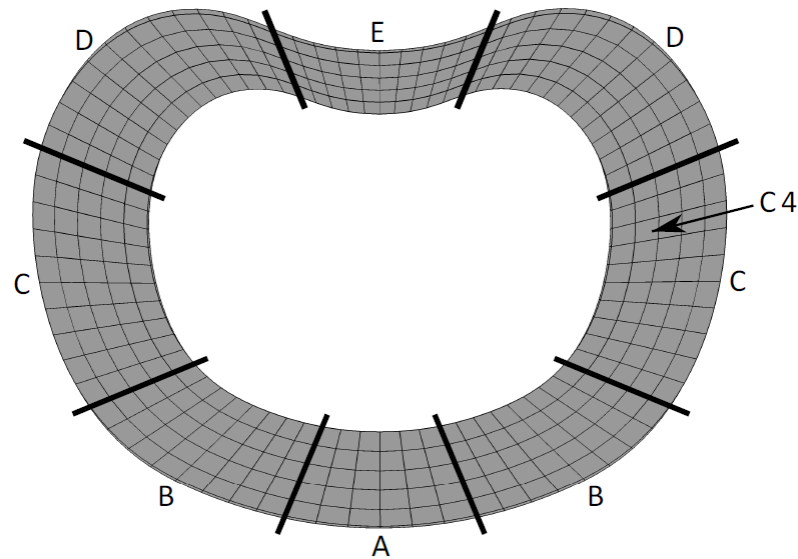
The annulus fibrosus was modeled as a Holzapfel-Gasser-Ogden incompressible hyperelastic material, as described by Holzapfel et al. (2000, 2010) and Gasser et al. (2005). This is an anisotropic hyperelastic model that considers the existence of fibers into a ground hyperelastic substance. The strain-energy density function is shown in Equation 2, with further details shown in Equation 3. The terms containing  $C_{10}$  and  $D$  control the stiffness and compressibility of the ground substance, representing the Neo-Hookean hyperelastic model.  $k_1$  and  $k_2$  define the stress-strain relation of the fibers, which only contribute to the strain energy in tension.  $N_f$  is the number of fiber families, with  $E_\alpha$  identifying the deformation of the fiber group,  $\kappa$  represents the level of dispersion of the fibers, and  $I_{4\alpha\alpha}$  is an invariant equal to the square of the stretch in each fiber.

$$W_\alpha = C_{10} (I_1 - 3) + \frac{1}{D} \left( \frac{J^2 - 1}{2} - \ln J \right) + \frac{k_1}{2k_2} \sum_{\alpha=1}^{N_f} \{ \exp[k_2 (E_\alpha)^2] - 1 \} \quad (2)$$

$$E_\alpha := \kappa (I_1 - 3) + (1 - 3\kappa) (I_{4\alpha\alpha} - 1) \quad (3)$$

The development of the whole thoracolumbar model was performed before this study, but only the L1-L2 segment was calibrated and validated. The soft tissue structures and contact of the facet joints were calibrated using resection studies for L1-L2. The calibration process for the annulus fibrosus was more complex than for the other structures because its mechanical properties are not constant throughout the material. Instead, they vary circumferentially and radially. Therefore, it was necessary to separate the annulus fibrosus into five circumferential regions and five radial regions, with specific mechanical properties, as shown in Figure 20.

Figure 20 – Division of the annulus fibrosus in 25 regions to accommodate variation in the mechanical properties. Circumferentially, regions were named from A to E starting from the anterior side. Radially, they were named from 1 to 5 starting from the external surface.



Source: Nicolini (2022).

Once the model was validated, the implantation of a VBT device at the L1-L2 level was simulated to analyze its effects on the biomechanics of the spine.

In this study, the calibration and validation of the other segments of the spine was performed.

### 3 METODOLOGY

#### 3.1 GENERAL ASPECTS

The development of this study was conducted in multiple stages that led to the calibration and validation of a reliable and robust model of the thoracolumbar spine and then to the application of that model to investigate the effects of VBT instrumentation on the biomechanics of the spine. The steps are listed in order below, and further explained later in this section.

1. Calibration of the mechanical properties of the IVDs and the ligaments of the thoracolumbar spine (T10-S1) using the data from the calibration of the L1-L2 IVD as described by Nicolini et al. (2022a), Oliveira (2022), Oliveira et al. (2023), and Nicolini (2022).
2. Final validation of the native thoracolumbar spine model.
3. Insertion of the VBT implants in T10-L3 and calibration of the mechanical behavior of the pre-tensioned tether in each simulated configuration.
4. Simulation of the behavior of the system spine-VBT for different configurations.

#### 3.2 CALIBRATION AND VALIDATION OF THE THORACOLUMBAR SPINE MODEL

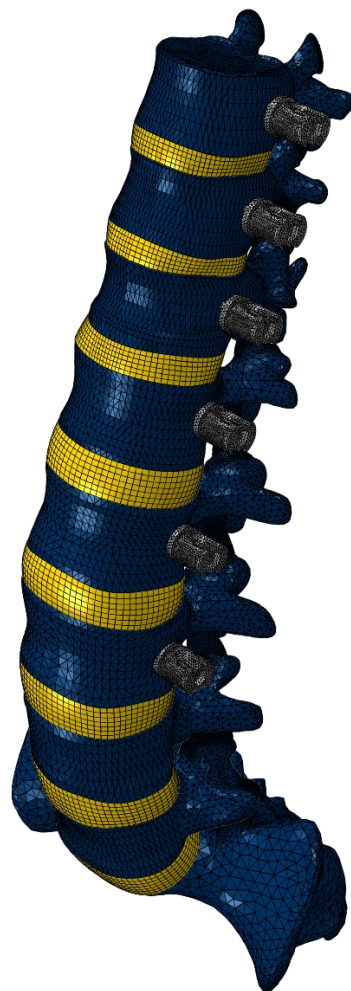
The primary objective of this phase was to develop a reliable and robust thoracolumbar spine model to be used for the VBT case study and for future implant analyses. As explained in the literature review, the mechanical properties of the IVD and ligaments of the L1-L2 segment were calibrated using optimization algorithms (NICOLINI et al., 2022b) coupled with experimental results from *in vitro* tests (BECKMANN et al., 2017; BECKMANN et al., 2019b; NICOLINI et al., 2021, 2022a). The calibration process aimed to better fit the numerical Moment-ROM curve of that segment in flexion, extension, axial rotation, and lateral bending to the experimental data.

The calibration process of the thoracolumbar spine model was conducted by extrapolating the mechanical properties of L1-L2 to the other segments via a scaling

procedure. The mechanical properties for the material models of L1-L2 were conveniently multiplied by a scaling coefficient in order to obtain ROMs with good correlation with experimental values obtained from native cadaveric spine tests.

The final calibration and validation of the model were conducted using data from multiple studies to approximate the average behavior reflected in the general literature, thereby minimizing bias from data specific to our research group.

Figure 21 – Thoracolumbar spine model (T10-S1) without tether.



Source: Author.

Once the native spine model was validated, the screws and tether were inserted into the model. The screws were positioned as shown in Figure 22.

Figure 22 – Screw positioning in the thoracolumbar spine model (T10-S1) instrumented with VBT.



Source: Author.

### 3.3 CALIBRATION OF THE PRE-TENSIONED TETHERS IN EACH TEST CONFIGURATION

This section presents the method used to obtain the mechanical behavior of the pre-tensioned PET fiber tether. These properties are entered into the model through the stiffness curves of the tether, which are calculated based on its Young's modulus, cross-sectional area, and length. The tether has a diameter of 4 mm, a Young's Modulus of 1,500 MPa in tension, and negligible resistance to compression (NICOLINI et al., 2022a; KULDUK et al., 2015).

The calibration process was performed in two steps. First, the desired tether pre-tensions were applied simultaneously to all the segments of the instrumented spine and the relative shortening of the cords was recorded. Then these shortening values were used to shift the tether stiffness curves to represent its mechanical behavior at the specified pre-tension, and the shifted curve was then included in ABAQUS. This procedure allowed the introduction of VBT instrumentation and tether pre-tensioning into the thoracolumbar spine model, making it ready for numerical simulation in different load cases.

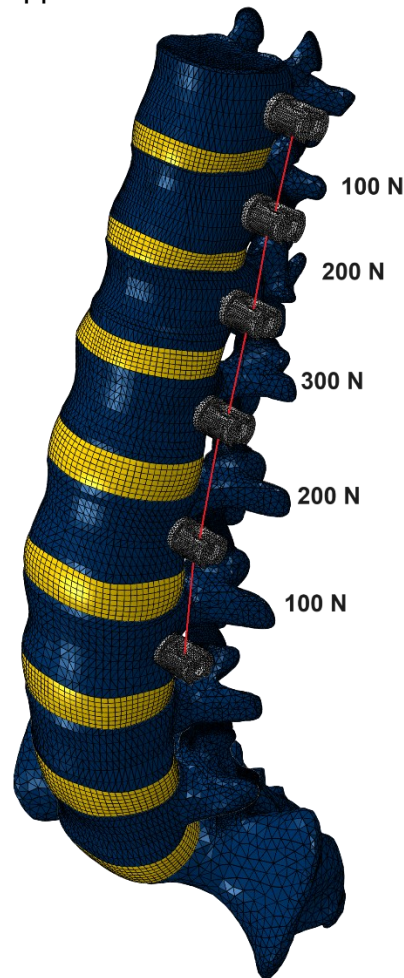


Once the results were satisfactory, a case study was conducted to evaluate how the biomechanics of the spine and the characteristics of the VBT implant are affected by pure moment loading in different pre-tension configurations.

### 3.4 SIMULATIONS OF DIFFERENT VBT CONFIGURATIONS IN THE SPINE UNDER PURE MOMENT LOADING

To investigate the biomechanical effects of VBT, the thoracolumbar spine model was instrumented with four different VBT configurations, spanning segments from T10 to L3 resulting in a total of five tethered segments. Three configurations were chosen to reflect a uniform pre-tensioning across all segments, either 100 N (Conf100N), 200 N (Conf200N), or 300 N (Conf300N). The fourth configuration was based on a gradient pre-tensioning approach, where a higher pre-tension is assigned to the apex of the scoliotic curve, and it is reduced in adjacent tethers until it reaches its minimum value at the extremities (ConfGrad). The use of this configuration is a common clinical practice because the curvature is more acute at the apex than at the extremities, thus requiring a higher tension at the tether to correct the scoliotic curve than in the adjacent segments. In this case, pre-tension of 100 N is assigned to the tethers at the T10-T11 and L2-L3 segments, while 200 N is assigned to T11-T12 and L1-L2, and 300 N is assigned to T12-L1 (COBETTO et al., 2018b, 2018c; RAITIO et al., 2022).

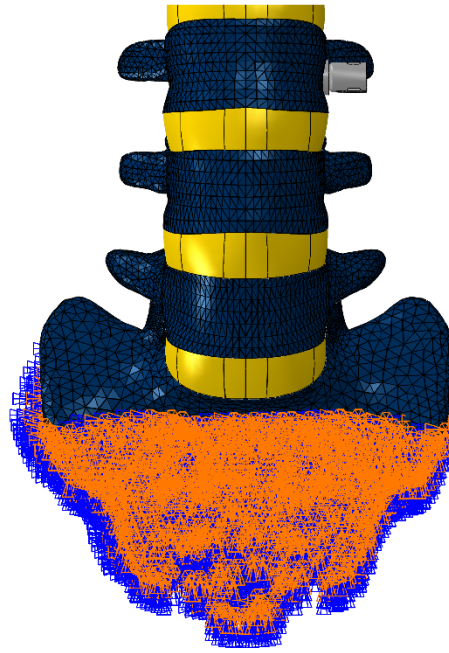
Figure 23 – Thoracolumbar spine model (T10-S1) instrumented with VBT in a tension gradient configuration. The tension at the apex is higher, while it decreases as it approaches the extremities.



Source: Author.

All these configurations were tested under a pure moment loading of 5 Nm in flexion, extension, left and right axial rotation, and left and right lateral bending applied at T10. As a boundary condition, the sacrum was constrained with fixed degrees of freedom (Figure 24). Pure moment loading has been shown to effectively replicate the effects of physiological loading on spinal implants, and the magnitude of 5 Nm has been used in other studies to evaluate the behavior of the thoracolumbar spine (COUVERTIER et al., 2017; GERMANEAU et al., 2016; NICOLINI et al., 2022b; WILKE et al., 2001). Results for ROM, force on the tethers, and coupled motion were obtained and recorded. The ROM of the spine and the other clinically relevant data presented in this work are measured from the post-surgery spinal position as the neutral position.

Figure 24 – Boundary condition of the thoracolumbar spine model (T10-S1) instrumented with VBT. The sacrum was constrained with fixed degrees of freedom.



Source: Author.

## 4 RESULTS

The results presented in this section include those related to the calibration and validation process of the spine model described in Sections 3.2 and 3.3, as well as ROM, forces acting on the tether during spine motion, and coupled motion for each of the four tethering cases described in Section 3.4.

### 4.1 CALIBRATION AND VALIDATION OF THE THORACOLUMBAR SPINE MODEL

This subsection presents the mechanical properties obtained from the calibration of the IVDs in the T10-S1 segments, as well as the behavior of the thoracolumbar native spine model under pure moment loading in comparison with experimental data from the literature in flexion, extension, lateral bending, and axial rotation. Some of the results have already been presented by the author (OLIVEIRA et al., 2023). The mechanical properties are shown in Table 8.

Table 8 – Material properties of each IVD in the thoracolumbar spine model (T10-S5) considering the Holzapfel-Gasser-Ogden Hyperelastic constitutive model for the annulus fibrosus and the Hyperelastic Mooney-Rivlin model for the nucleus pulposus.

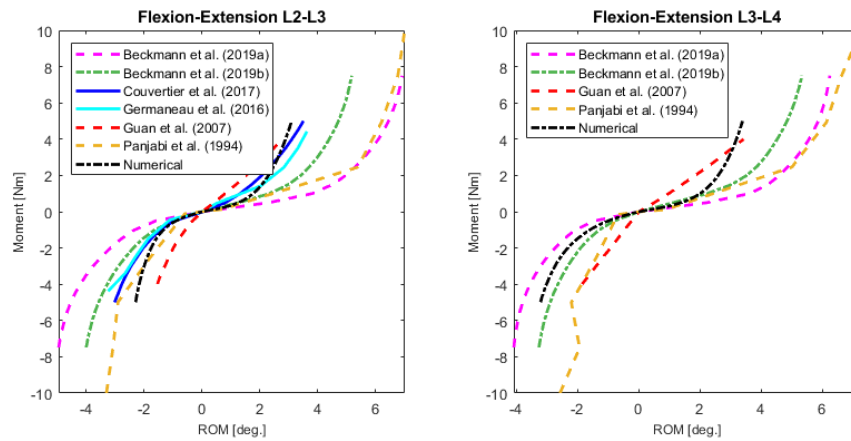
<b>Material Properties</b>	<b>T10-T11</b>	<b>T11-T12</b>	<b>T12-L1</b>	<b>L1-L2</b>	<b>L2-L3</b>	<b>L3-L4</b>	<b>L4-L5</b>	<b>L5-S1</b>
$C_{10n}$	0.030	0.030	0.030	0.030	0.015	0.015	0.015	0.015
$C_{01n}$	0.19	0.19	0.19	0.19	0.095	0.095	0.095	0.095
$C_{10}$	0.22	0.22	0.22	0.22	0.11	0.11	0.11	0.11
$k_1$	4.5	4.5	4.5	4.5	5.0	5.0	5.0	5.0
$k_2$	300	300	300	300	300	300	300	300
$\kappa$	0.1	0.1	0.1	0.1	0.1	0.1	0.1	0.1
$\beta$	30°	30°	30°	30°	30°	30°	30°	30°
$k_{1c}$	-0.05	-0.15	-0.05	-0.05	-0.24	-0.24	-0.24	-0.24
$k_{2c}$	-0.05	-0.15	-0.05	-0.05	-0.24	-0.24	-0.24	-0.24
$k_{1r}$	-0.15	-0.15	-0.15	-0.15	-0.15	-0.15	-0.15	-0.15
$k_{2r}$	-0.15	-0.15	-0.15	-0.15	-0.15	-0.15	-0.15	-0.15
$\beta_c$	0.1	0.1	0.1	0.1	0.1	0.1	0.1	0.1

Source: Adapted from Oliveira et al. (2023).

Figure 25 to Figure 27 show the fitting of the moment-ROM curves of the thoracolumbar model in the L2-L3 and L3-L4 segments in flexion-extension, axial rotation, and lateral bending, respectively. The ROM results exhibit significant variation among different studies and samples. Taking the L2-L3 segment as an

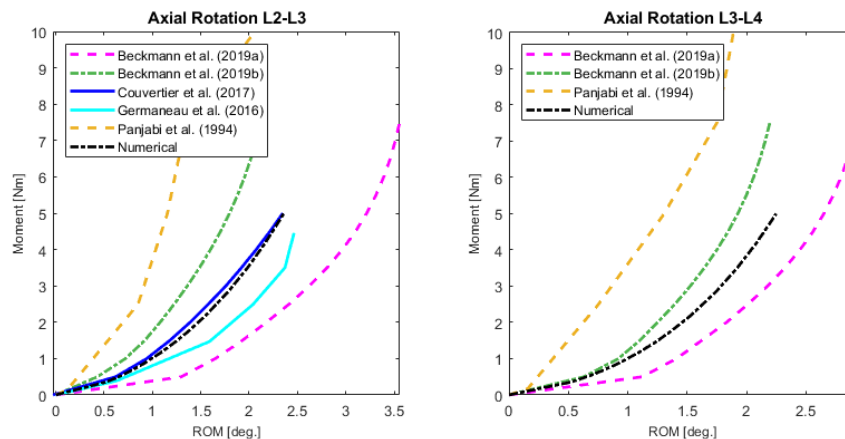
example, at 5 Nm in lateral bending, the ROM varies between 3.5° and 6° across studies, representing a variation of 42% of the highest value. The numerical ROM value for this segment and loading condition is 5.25°, which falls within the expected range of experimental in vitro data. The numerical ROM across all segments and loading conditions encompassed in this work either falls between the maximum and minimum ROM data found in the literature or is sufficiently close to be considered acceptable, given the variability between different studies. This analysis shows that the behavior of the numerical model falls within the data spectrum of experimental curves published in the literature, and this consistency with empirical data validates the model as a reliable tool for studying the biomechanics of the spine. The complete set of graphs showing moment-ROM for each segment, related to the validation of the thoracolumbar spine model, is presented in Appendix A.

Figure 25 – Comparison of the Moment-ROM curve of the L2-L3 and L3-L4 segments of the model with literature data in flexion-extension.



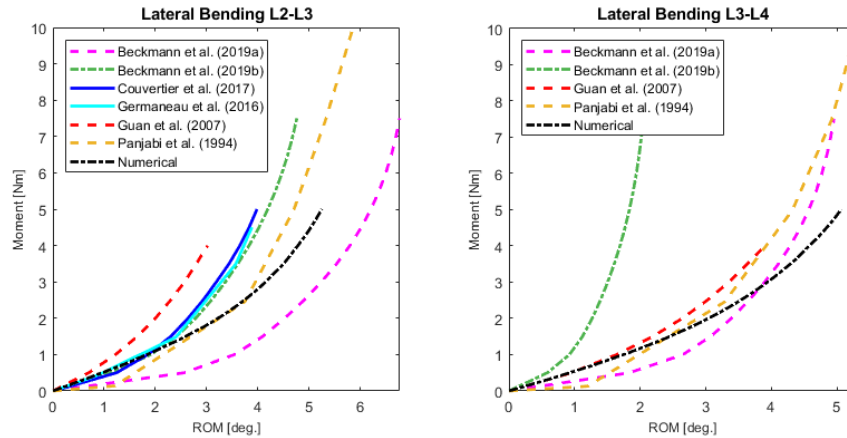
Source: Adapted from Oliveira et al. (2023).

Figure 26 – Comparison of the Moment-ROM curve of the L2-L3 and L3-L4 segments of the model with literature data in axial rotation.



Source: Adapted from Oliveira et al. (2023).

Figure 27 – Comparison of the Moment-ROM curve of the L2-L3 and L3-L4 segments of the model with literature data in lateral bending.



Source: Adapted from Oliveira et al. (2023).

## 4.2 IMMEDIATE POST-SURGICAL CURVE CORRECTION

As previously discussed, VBT surgery consists of tensioning a tether anchored to the convex side of the scoliotic spine so that part of the curvature will decrease immediately after surgery, while the remaining curvature will be gradually corrected due to the Hueter-Volkmann law. Thus, post-surgical correction is a key measurable result of VBT surgery to assess its effectiveness.

Table 9 shows the immediate post-surgical correction for each of the four different pre-tensioning configurations given in terms of angular variation at each segment of the instrumented spine (T10-L3), and the whole thoracolumbar spine (T10-S1). Since the angular variation of the non-instrumented segments was negligible, they are not presented in Table 9.

As a rule, it has been observed that the greater the pre-tension, the greater the correction, which is a very intuitive result. Similarly, the results of the ConfGrad configuration show that, in all directions of rotation, the main factor in determining the surgical correction in a specific segment is the pre-tension assigned to it, despite the pre-tension in adjacent segments. That is due to the segmental correction in the ConfGrad configuration almost matching the correction at that same segment in other configurations with the same pre-tension. Also, considering the whole instrumented spine or the whole thoracolumbar spine model, the overall correction increases with the pre-tension for the even tensioned configurations - Conf100N, Conf200N, and

Conf300N. ConfGrad presented intermediary correction compared to the other configurations, being closer to but slightly lower than Conf200N.

Table 9 – Immediate post-surgical correction (in degrees) of the scoliotic curve with different VBT pre-tensioning configurations for each segment of the instrumented spine and the whole thoracolumbar spine model.

<b>Motion</b>	<b>Condition</b>	<b>T10-T11</b>	<b>T11-T12</b>	<b>T12-L1</b>	<b>L1-L2</b>	<b>L2-L3</b>	<b>T10-L3</b>	<b>T10-S1</b>
<b>Flexion-extension</b>	Conf100N	-0.70	-0.54	-0.92	-0.92	-0.13	-3.21	-3.22
	Conf200N	-1.11	-0.87	-1.17	-1.21	0.10	-4.26	-4.29
	Conf300N	-1.39	-1.11	-1.24	-1.25	0.18	-4.80	-4.84
	ConfGrad	-0.70	-0.89	-1.23	-1.20	-0.10	-4.13	-4.14
<b>Axial rotation</b>	Conf100N	-0.49	-0.57	-0.68	-0.78	-0.92	-3.45	-3.45
	Conf200N	-0.66	-0.83	-1.03	-1.18	-1.11	-4.82	-4.81
	Conf300N	-0.75	-0.99	-1.23	-1.44	-1.22	-5.63	-5.60
	ConfGrad	-0.46	-0.86	-1.27	-1.17	-0.93	-4.69	-4.68
<b>Lateral bending</b>	Conf100N	-1.34	-1.15	-2.08	-2.78	-3.90	-11.25	-11.26
	Conf200N	-2.15	-1.95	-3.17	-4.47	-5.49	-17.22	-17.24
	Conf300N	-2.70	-2.53	-3.82	-5.48	-6.36	-20.89	-20.94
	ConfGrad	-1.29	-1.98	-3.87	-4.44	-3.89	-15.47	-15.47

Source: Author.

#### 4.3 RANGE OF MOTION

Since one of the greatest advantages of VBT surgery is the capacity of preserving spinal ROM, in contrast with spinal fusion, it is important to identify the degree to which mobility can be preserved and how different pre-tensioning configurations affect this feature.

Table 10 shows the ROM results for each segment and the whole of the instrumented spine. They show a decrease in ROM with increased pre-tension.

Table 10 – Range of motion (in degrees) of the spine at pure moment loading of 5 Nm in flexion-extension, lateral bending, and axial rotation measured from the immediate post-surgery position. The data of the native spine has been published by Oliveira et al. (2023).

		<b>T10-T11</b>	<b>T11-T12</b>	<b>T12-L1</b>	<b>L1-L2</b>	<b>L2-L3</b>	<b>T10-L3</b>
<b>Extension</b>	Native	-3.07	-2.75	-2.94	-3.25	-2.30	-14.32
	Conf100N	-2.52	-2.34	-1.99	-2.20	-1.42	-10.46
	Conf200N	-2.16	-2.02	-1.56	-1.55	-0.95	-8.24
	Conf300N	-1.87	-1.72	-1.33	-1.19	-0.71	-6.81
	ConfGrad	-2.53	-2.02	-1.35	-1.54	-1.39	-8.83
<b>Flexion</b>	Native	2.62	2.42	3.12	3.25	3.09	14.49
	Conf100N	2.57	2.21	3.38	3.49	2.21	13.86
	Conf200N	2.29	1.93	2.93	2.92	1.23	11.30
	Conf300N	2.02	1.68	2.40	2.29	0.86	9.25
	ConfGrad	2.56	1.95	2.41	2.92	2.21	12.05
<b>Right AR</b>	Native	-2.11	-2.00	-2.22	-2.05	-2.36	-10.74
	Conf100N	-1.65	-1.52	-1.68	-1.46	-1.49	-7.80
	Conf200N	-1.37	-1.25	-1.25	-1.06	-1.09	-6.03
	Conf300N	-1.17	-1.05	-0.97	-0.80	-0.84	-4.83
	ConfGrad	-1.64	-1.24	-0.98	-1.05	-1.48	-6.39
<b>Left AR</b>	Native	2.11	2.00	2.22	2.05	2.36	10.74
	Conf100N	2.14	1.98	1.66	1.63	1.91	9.33
	Conf200N	1.84	1.76	1.30	1.24	1.38	7.52
	Conf300N	1.54	1.49	1.02	0.97	1.05	6.09
	ConfGrad	2.16	1.76	1.03	1.21	1.89	8.05
<b>Left LB</b>	Native	-2.21	-2.02	-3.26	-4.27	-5.25	-17.00
	Conf100N	-0.91	-0.88	-1.18	-1.48	-1.35	-5.79
	Conf200N	-0.70	-0.70	-0.80	-0.86	-0.75	-3.80
	Conf300N	-0.57	-0.57	-0.62	-0.64	-0.58	-2.99
	ConfGrad	-0.91	-0.71	-0.64	-0.86	-1.35	-4.46
<b>Right LB</b>	Native	2.21	2.02	3.26	4.27	5.25	17.00
	Conf100N	1.12	0.98	1.15	1.28	1.54	6.07
	Conf200N	0.95	0.85	0.99	1.11	1.15	5.05
	Conf300N	0.78	0.71	0.82	0.92	0.85	4.08
	ConfGrad	1.11	0.86	0.84	1.11	1.54	5.45

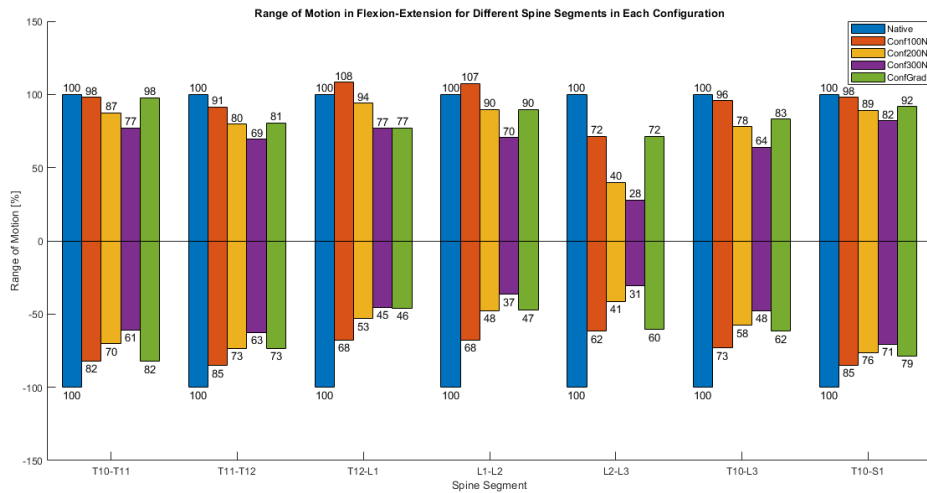
Source: Author.

Figure 28 to Figure 30 show the percentage of mobility that is preserved for the thoracolumbar spine in the native and instrumented conditions in flexion-extension, axial rotation, and lateral bending. Considering individual segments, it can be observed that the segments in the ConfGrad configuration show the same mobility preservation as the corresponding segments in the configuration with equivalent pre-tension. The lowest preservation of mobility happened in right lateral bending of the L2-L3 with the Conf300N configuration. It is also worth noting that the L2-L3 segment presented much lower mobility preservation in flexion than the other segments. This



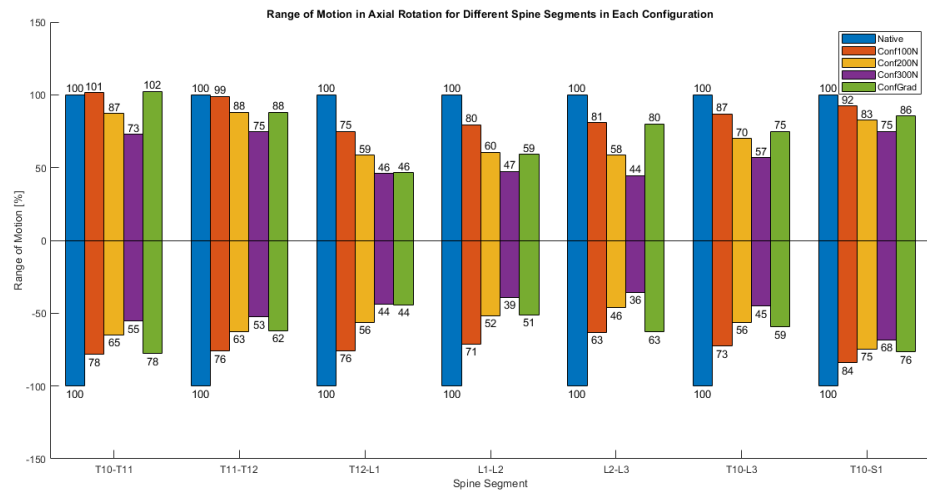
difference may be explained by the natural lordosis of the lumbar spine, that has an influence on the angle of the VBT's tether leading to greater resistance to flexion.

Figure 28 – Preservation of range of motion compared to the native spine when segments T10-L3 are instrumented with VBT in flexion-extension. Four different configurations of instrumentation are compared to the native spine. Negative values indicate extension and positive values indicate flexion.



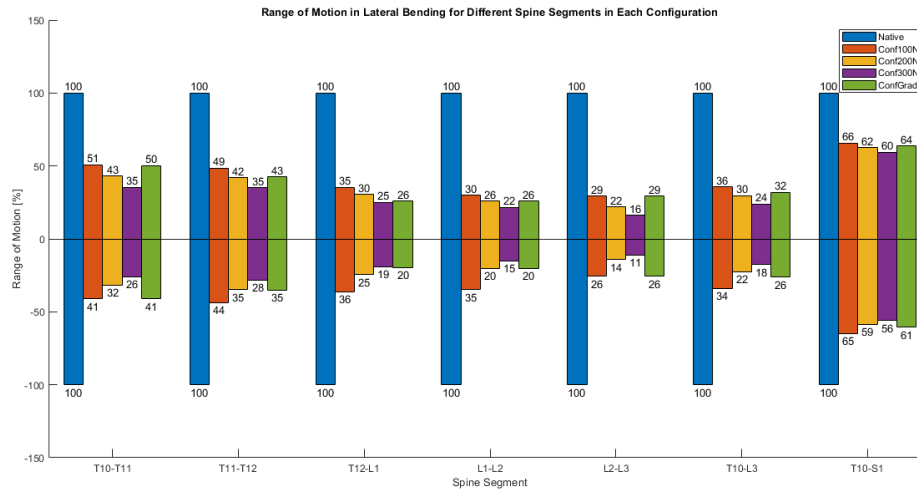
Source: Author.

Figure 29 – Preservation of range of motion compared to the native spine when segments T10-L3 are instrumented with VBT in axial rotation. Four different configurations of instrumentation are compared to the native spine. Negative values indicate right axial rotation and positive values indicate left axial rotation.



Source: Author.

Figure 30 – Preservation of range of motion compared to the native spine when segments T10-L3 are instrumented with VBT in lateral bending. Four different configurations of instrumentation are compared to the native spine. Negative values indicate left lateral bending and positive values indicate right lateral bending.

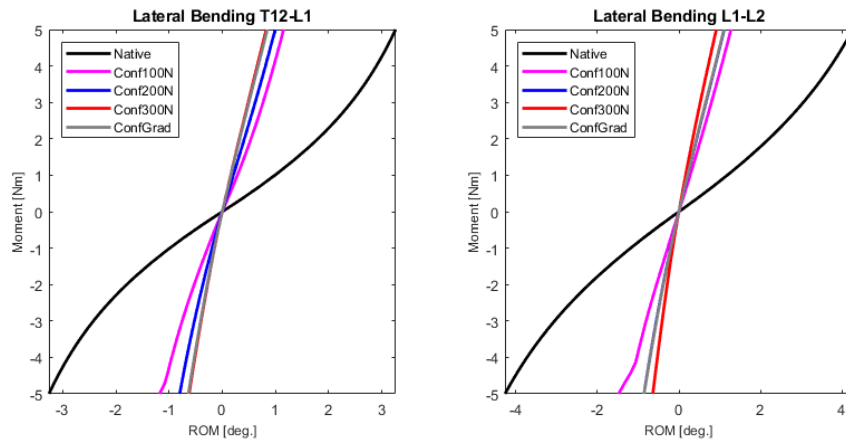


Source: Author.

Considering the global ROM, the mobility preservation with the Conf300N configuration was the lowest. The instrumented spine (T10-L3) preserved between 18% and 64% of native spine ROM, depending on the direction of motion, while the whole thoracolumbar spine (T10-S1) preserved between 56% and 82%. The ConfGrad configuration showed slightly better motion preservation than the Conf200N configuration when considering the whole model or the whole instrumented spine.

Appendix B presents moment-ROM graphs for each segment of the native and the instrumented spine. It takes into consideration each pre-tension configuration and all the directions of motion. Among details of the motion that can be observed in those graphs is the point of the ROM curve at which the tether in the Conf100N under left lateral bending at some segments, such as L1-L2, loses all tensioning and the moment-ROM curve starts to follow a path different from expected, as shown in Figure 31 below.

Figure 31 – Moment-ROM curves of the T12-L1 and L1-L2 segments of the spine in different pre-tension configurations under pure lateral bending moment loading.

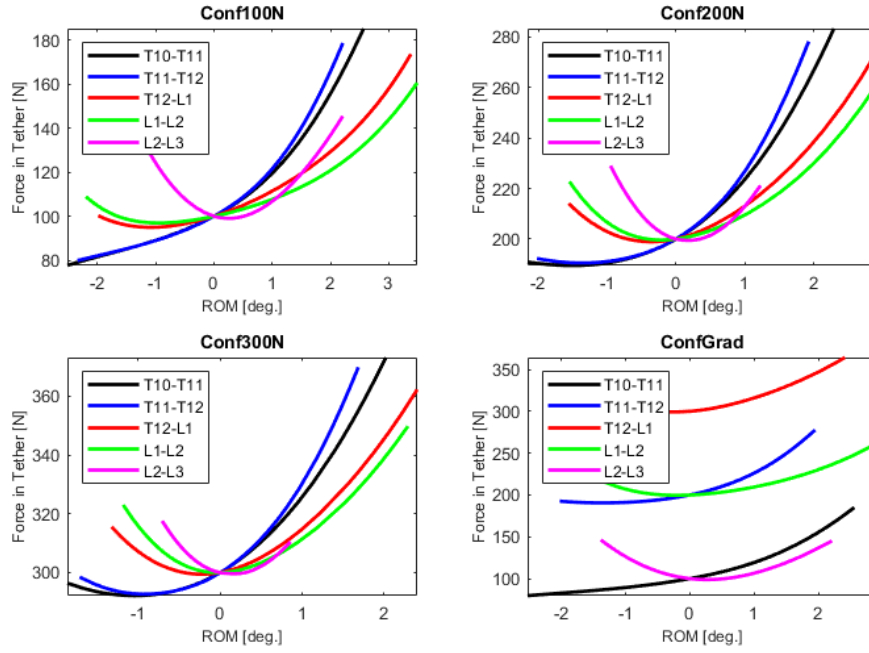


Source: Author.

#### 4.4 FORCES ACTING ON THE TETHER

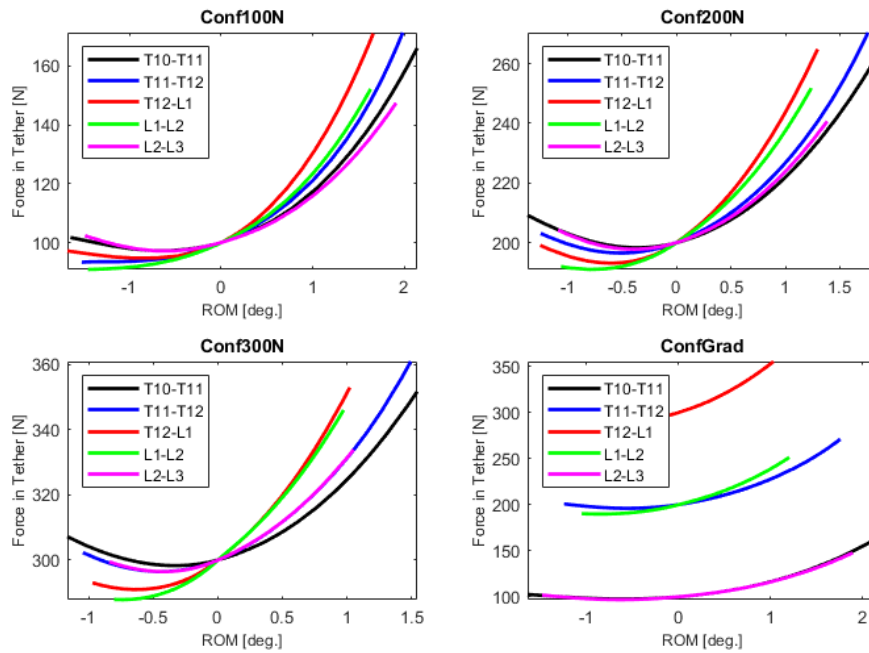
Figure 32 to Figure 34 show the Tether Force-ROM graphs for each configuration in all moment directions – flexion-extension, axial rotation, and lateral bending. It can be observed that the instrumented spine tends to produce higher tension in the tether during left axial rotation than right axial rotation. In lateral bending, there is not much difference in the forces acting on the tether in different segments as long as the pre-tension is the same. However, the data regarding the flexion-extension motion suggests that instrumented lumbar segments tend to generate higher tensions in the tether than thoracic segments. This is most likely due to the lumbar lordosis that affects the angle of the tether between lumbar segments leading to more resistance to both flexion and extension by the implant. The role of this lordosis is supported by the behavior of the L2-L3 segment, where this physiological curve is more accentuated, that shows similar tensions in both flexion and extension, with a higher tension in flexion, which is contrary to all other segments analyzed.

Figure 32 – Tether Force-ROM graphs in flexion-extension. Each graph presents all instrumented segments in a specific configuration.



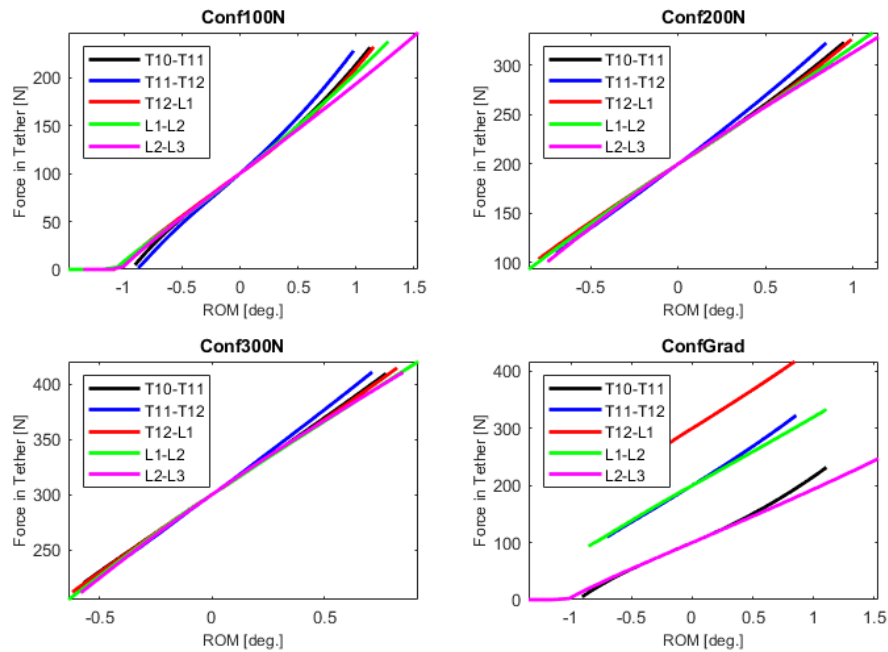
Source: Author.

Figure 33 – Tether Force-ROM graphs in axial rotation. Each graph presents all instrumented segments in a specific configuration.



Source: Author.

Figure 34 – Tether Force-ROM graphs in lateral bending. Each graph presents all instrumented segments in a specific configuration.



Source: Author.

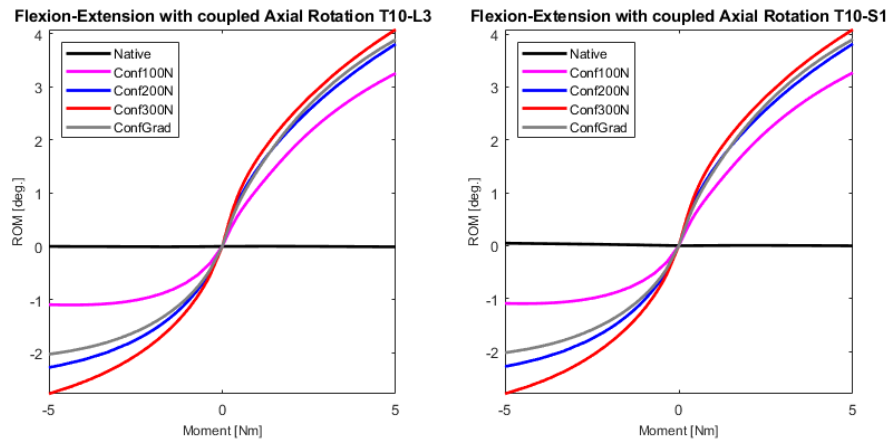
Appendix C shows graphs regarding the forces acting on the tether for each segment across all pre-tension configurations. This type of graph is significant to verify if the general behavior of the tether at a specific segment is consistent across different pre-tensions or if there are any significant changes. The general shape of the curves for each direction of motion is consistent across segments, and the lumbar segments under left lateral bending show consistency with the ROM results as the tether reaches 0 N in the Conf100N configuration. All segments in the ConfGrad configuration showed equivalent behavior in other configurations with the same pre-tension, which reinforces the assessment that the main factor influencing the biomechanics of an individual segment instrumented with VBT is the tether's pre-tension at that segment.

#### 4.5 COUPLED MOTION

Figure 35 to Figure 40 illustrate the coupled motions observed under each moment loading direction for all pre-tension configurations. Flexion-Extension loading has been shown not to produce coupled motion in the native spine due to its symmetry on the sagittal plane. However, VBT instrumentation on the left lateral side

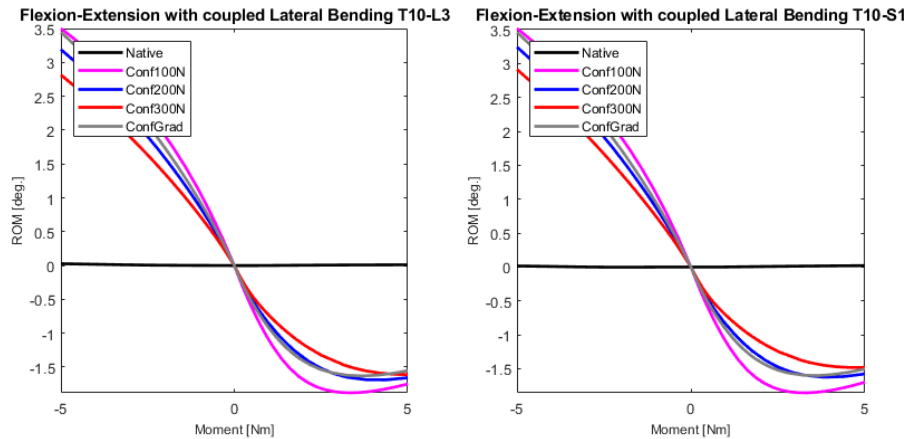
of the vertebral bodies leads the spine to experience coupled left axial rotation and left lateral bending motions during flexion loading, and to experience coupled right axial rotation and right lateral bending during extension loading. While increasing pre-tension seems to increase coupled axial rotation, it seems to decrease coupled lateral bending. The ConfGrad configuration shows behavior very similar to Conf200N in coupled axial rotation and coupled left lateral bending, but in coupled right lateral bending it is shown to behave similarly to the Conf100N configuration.

Figure 35 – Coupled Axial Rotation Motion versus Flexion-Extension Moment curves of the T10-L3 and T10-S1 segments of the spine in different pre-tension configurations.



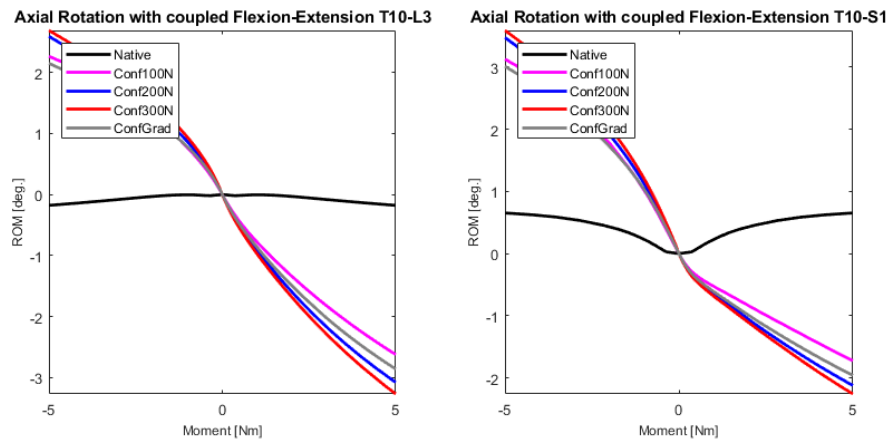
Source: Author.

Figure 36 – Coupled Lateral Bending Motion versus Flexion-Extension Moment curves of the T10-L3 and T10-S1 segments of the spine in different pre-tension configurations.



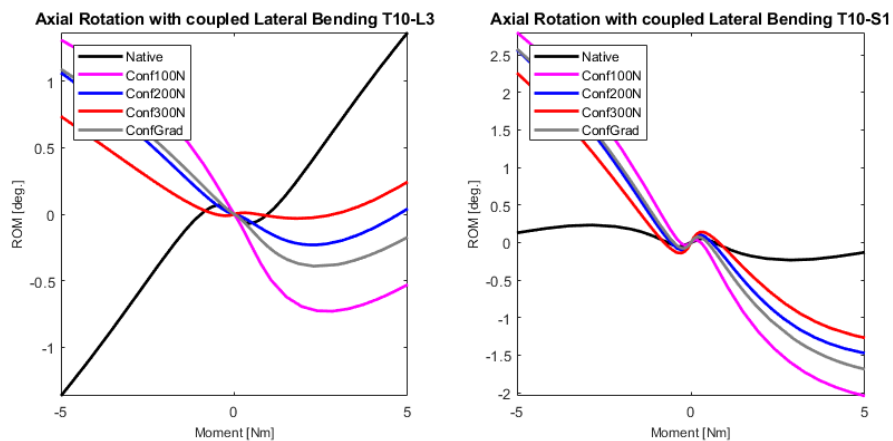
Source: Author.

Figure 37 – Coupled Flexion-Extension Motion versus Axial Rotation Moment curves of the T10-L3 and T10-S1 segments of the spine in different pre-tension configurations.



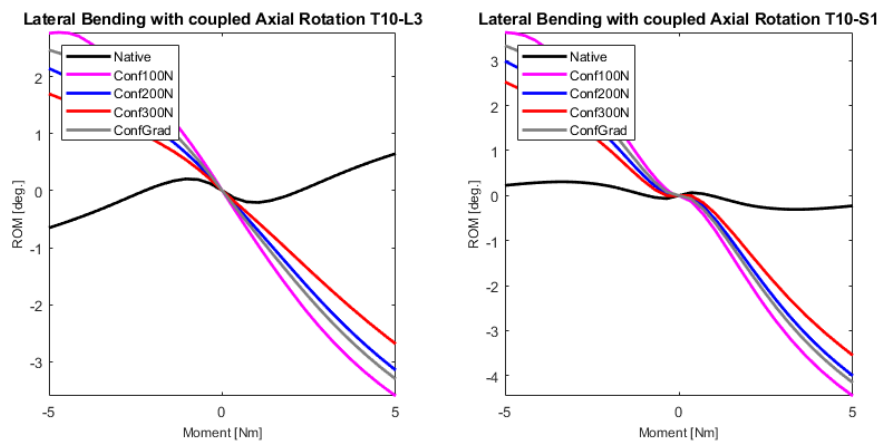
Source: Author.

Figure 38 – Coupled Lateral Bending Motion versus Axial Rotation Moment curves of the T10-L3 and T10-S1 segments of the spine in different pre-tension configurations.



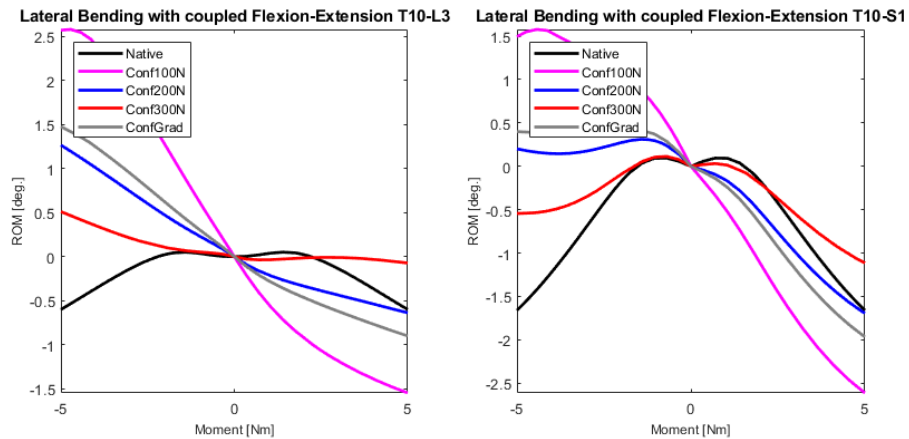
Source: Author.

Figure 39 – Coupled Axial Rotation Motion versus Lateral Bending Moment curves of the T10-L3 and T10-S1 segments of the spine in different pre-tension configurations.



Source: Author.

Figure 40 – Coupled Flexion-Extension Motion versus Lateral Bending Moment curves of the T10-L3 and T10-S1 segments of the spine in different pre-tension configurations.



Source: Author.

During pure axial rotation moment loading, the native T10-L3 spine presents practically no coupled flexion-extension motion, while the T10-S1 spine presents a slight flexion (Figure 37). The VBT's setup induces coupled flexion during right axial rotation and coupled extension during left axial rotation. This effect increases as pre-tension increases. Regarding coupled lateral bending during main axial rotation motion, native T10-L3 presents significant coupled left lateral bending during right axial rotation loading and coupled right lateral bending during left axial rotation loading. For the native T10-S1 this effect is less pronounced, and little coupled lateral bending is observed during axial rotation. The VBT instrumentation induces coupled right lateral bending during right axial rotation and coupled left lateral bending during left axial rotation. This effect is decreased with the increase of pre-tension. The ConfGrad configuration presents behavior similar to the Conf200N in coupled lateral bending and extension, and similar to Conf100N in flexion.

The native spine presents little coupled axial rotation during pure moment lateral bending loading, and it decreases when considering T10-S1 instead of T10-L3. However, while instrumented with VBT, left lateral bending loading induced coupled left axial rotation motion and right lateral bending loading induced coupled right axial rotation motion. There was also coupled extension motion during lateral bending of the native T10-L3 and T10-S1 spine, with this behavior being more pronounced in the latter. VBT instrumentation induces coupled flexion during left



lateral bending, probably due to the decrease in the tether's tension caused by this motion and induces coupled extension during right lateral bending. VBT instrumentation tended to decrease all couple motion during lateral bending motion, with Conf300N yielding less coupled extension than the native spine during lateral bending in both directions.

Table 11 presents the numerical results of highest coupled motion locally and globally. L3-L4 is included in the table because, even though it is not instrumented, it presented significant coupled motion in some cases probably due to the anchor placed on the L3 vertebra. The L4-L5 and L5-S1 segments didn't present any variation in coupled motion with the instrumentation of the adjacent segments. The highest coupled motions in the native L4-L5 and L5-S1 are displayed in Table 12. The Coupled Motion-Moment graphs for each individual segment are presented in Appendix D, where it is possible to verify at which point of loading the coupled motion reached its peak and directly compare the behavior between different configurations.

Table 11 – Maximum coupled motion (in degrees) of the spine at pure moment loading of 5 Nm in flexion-extension, lateral bending, and axial rotation measured in degrees from the immediate post-surgery position.

		T10-T11	T11-T12	T12-L1	L1-L2	L2-L3	L3-L4	T10-L3	T10-S1
<b>Loading:</b> <b>Extension</b>	Native	0.00	0.00	0.00	0.00	-0.01	0.01	0.00	0.05
	Conf100N	-0.12	-0.08	-0.31	-0.30	-0.29	-0.03	-1.09	-1.09
<b>Coupled Motion:</b> <b>Axial Rotation</b>	Conf200N	-0.30	-0.26	-0.54	-0.56	-0.61	-0.05	-2.27	-2.28
	Conf300N	-0.38	-0.37	-0.63	-0.65	-0.74	-0.07	-2.77	-2.80
	ConfGrad	-0.21	-0.28	-0.64	-0.58	-0.32	-0.04	-2.03	-2.02
<b>Loading:</b> <b>Flexion</b>	Native	0.00	0.00	-0.01	0.00	-0.01	0.00	-0.01	0.00
	Conf100N	0.69	0.47	0.62	0.59	0.88	0.02	3.25	3.27
<b>Coupled Motion:</b> <b>Axial Rotation</b>	Conf200N	0.79	0.63	0.82	0.68	0.88	0.02	3.80	3.82
	Conf300N	0.80	0.68	0.90	0.78	0.91	0.01	4.07	4.09
	ConfGrad	0.70	0.66	0.98	0.68	0.87	0.02	3.88	3.90
<b>Loading:</b> <b>Extension</b>	Native	0.00	0.00	0.00	0.03	0.00	0.00	0.03	0.02
	Conf100N	0.77	0.57	0.80	0.67	0.70	0.03	3.50	3.52
<b>Coupled Motion:</b> <b>Lateral Bending</b>	Conf200N	0.76	0.57	0.81	0.63	0.43	0.06	3.19	3.25
	Conf300N	0.70	0.53	0.75	0.55	0.30	0.11	2.82	2.91
	ConfGrad	0.81	0.57	0.79	0.62	0.66	0.03	3.45	3.46

Source: Author.

Table 11 – Continued.

		T10-T11	T11-T12	T12-L1	L1-L2	L2-L3	L3-L4	T10-L3	T10-S1
<b>Loading: Flexion</b>	Native	0.00	0.01	-0.01	0.02	0.00	0.00	0.01	0.02
	Conf100N	-0.35	-0.36	-0.73	-0.45	-0.17	0.04	-1.88	-1.86
<b>Coupled Motion: Lateral Bending</b>	Conf200N	-0.33	-0.33	-0.69	-0.33	-0.10	0.07	-1.69	-1.62
	Conf300N	-0.33	-0.30	-0.65	-0.28	-0.10	0.12	-1.61	-1.48
	ConfGrad	-0.36	-0.32	-0.66	-0.34	-0.16	0.04	-1.63	-1.60
<b>Loading: Right AR</b>	Native	-0.37	-0.19	0.17	0.18	0.03	0.16	-0.18	0.65
	Conf100N	0.24	0.30	0.67	0.87	0.19	0.18	2.26	3.12
<b>Coupled Motion: Flexion- Extension</b>	Conf200N	0.50	0.48	0.52	0.83	0.26	0.21	2.59	3.47
	Conf300N	0.64	0.56	0.42	0.73	0.34	0.23	2.69	3.59
	ConfGrad	0.37	0.44	0.36	0.80	0.18	0.18	2.15	3.01
<b>Loading: Left AR</b>	Native	-0.37	-0.19	0.17	0.18	0.09	0.16	-0.18	0.65
	Conf100N	-0.94	-0.77	-0.24	-0.60	-0.08	0.23	-2.62	-1.72
<b>Coupled Motion: Flexion- Extension</b>	Conf200N	-1.00	-0.85	-0.32	-0.66	-0.25	0.29	-3.08	-2.12
	Conf300N	-1.00	-0.85	-0.40	-0.69	-0.34	0.35	-3.27	-2.25
	ConfGrad	-1.00	-0.80	-0.35	-0.65	-0.06	0.23	-2.86	-1.96
<b>Loading: Right AR</b>	Native	0.16	0.11	-0.35	-0.46	-0.75	0.07	-1.36	0.23
	Conf100N	0.43	0.37	0.22	0.11	0.18	0.07	1.31	2.80
<b>Coupled Motion: Lateral Bending</b>	Conf200N	0.33	0.27	0.15	0.07	0.23	0.09	1.06	2.57
	Conf300N	0.23	0.20	0.08	0.04	0.19	0.11	0.73	2.26
	ConfGrad	0.42	0.28	0.10	0.09	0.19	0.07	1.09	2.58
<b>Loading: Left AR</b>	Native	-0.16	-0.11	0.35	0.46	0.75	-0.07	1.36	0.23
	Conf100N	-0.17	-0.29	-0.07	-0.09	-0.16	-0.08	-0.73	-2.04
<b>Coupled Motion: Lateral Bending</b>	Conf200N	0.12	-0.16	0.11	0.07	-0.12	-0.09	-0.23	-1.47
	Conf300N	0.19	-0.08	0.11	0.11	-0.10	-0.08	0.24	-1.27
	ConfGrad	-0.15	-0.15	0.07	0.06	-0.17	-0.08	-0.39	-1.69
<b>Loading: Left LB</b>	Native	0.36	0.21	-0.20	-0.41	-0.60	-0.27	-0.65	0.31
	Conf100N	0.83	0.77	0.50	0.43	0.34	-0.28	2.77	3.63
<b>Coupled Motion: Axial Rotation</b>	Conf200N	0.69	0.64	0.40	0.27	0.15	-0.30	2.14	2.99
	Conf300N	0.60	0.52	0.32	0.20	0.05	-0.32	1.70	2.53
	ConfGrad	0.86	0.65	0.36	0.29	0.34	-0.28	2.47	3.33
<b>Loading: Right LB</b>	Native	-0.36	-0.21	0.20	0.41	0.60	0.27	0.65	-0.31
	Conf100N	-1.13	-0.93	-0.78	-0.53	-0.23	0.29	-3.60	-4.45
<b>Coupled Motion: Axial Rotation</b>	Conf200N	-0.99	-0.79	-0.66	-0.47	-0.22	0.29	-3.14	-4.00
	Conf300N	-0.86	-0.67	-0.57	-0.40	-0.18	0.28	-2.68	-3.55
	ConfGrad	-1.11	-0.81	-0.64	-0.52	-0.22	0.29	-3.30	-4.16

Source: Author.

Table 11 – Continued.

		T10-T11	T11-T12	T12-L1	L1-L2	L2-L3	L3-L4	T10-L3	T10-S1
<b>Loading: Left LB</b>	Native	-0.12	-0.12	-0.01	-0.33	0.10	-0.37	-0.60	-1.66
	Conf100N	0.55	0.38	0.93	0.65	0.14	-0.35	2.58	1.58
<b>Coupled Motion: Flexion- Extension</b>	Conf200N	0.35	0.20	0.57	0.29	-0.14	-0.34	1.27	0.31
	Conf300N	0.22	0.09	0.34	0.06	-0.20	-0.33	0.51	-0.54
	ConfGrad	0.52	0.21	0.35	0.29	0.14	-0.35	1.48	0.43
<b>Loading: Right LB</b>	Native	-0.12	-0.12	-0.01	-0.33	0.10	-0.37	-0.60	-1.66
	Conf100N	-0.19	-0.10	-0.45	-0.57	-0.24	-0.37	-1.55	-2.61
<b>Coupled Motion: Flexion- Extension</b>	Conf200N	-0.10	-0.03	-0.34	-0.28	0.11	-0.36	-0.64	-1.69
	Conf300N	-0.04	0.05	-0.22	-0.09	0.22	-0.35	-0.07	-1.12
	ConfGrad	-0.19	-0.02	-0.21	-0.28	-0.23	-0.37	-0.90	-1.97

Source: Author.

Table 12 – Coupled motion (in degrees) of the L4-S1 segments of the native spine at pure moment loading of 5 Nm in flexion-extension, lateral bending, and axial rotation measured in degrees.

		L4-L5	L5-S1
<b>Loading: Extension</b>			
<b>Coupled Motion: Axial Rotation</b>	Native	-0.01	0.04
<b>Loading: Flexion</b>			
<b>Coupled Motion: Axial Rotation</b>	Native	0.01	0.00
<b>Loading: Extension</b>			
<b>Coupled Motion: Lateral Bending</b>	Native	-0.01	0.00
<b>Loading: Flexion</b>			
<b>Coupled Motion: Lateral Bending</b>	Native	0.00	0.01
<b>Loading: Right AR</b>			
<b>Coupled Motion: Flexion-Extension</b>	Native	0.36	0.30
<b>Loading: Left AR</b>			
<b>Coupled Motion: Flexion-Extension</b>	Native	0.36	0.30
<b>Loading: Right AR</b>			
<b>Coupled Motion: Lateral Bending</b>	Native	0.56	0.87
<b>Loading: Left AR</b>			
<b>Coupled Motion: Lateral Bending</b>	Native	-0.56	-0.87

Source: Author.

Table 12 – Continued.

		<b>L4-L5</b>	<b>L5-S1</b>
<b>Loading: Left LB</b>			
<b>Coupled Motion: Axial Rotation</b>	Native	0.28	0.87
<b>Loading: Right LB</b>			
<b>Coupled Motion: Axial Rotation</b>	Native	-0.28	-0.87
<b>Loading: Left LB</b>			
<b>Coupled Motion: Flexion-Extension</b>	Native	-0.15	-0.54
<b>Loading: Right LB</b>			
<b>Coupled Motion: Flexion-Extension</b>	Native	-0.15	-0.54

Source: Author.

## 5 DISCUSSION

The first part of this work, concerning the calibration and validation of the mechanical properties of the spine, was crucial to ensure reliable results in further case studies. Modelling and validation of spine models are not new in literature, and there is a wide variety of them worldwide. Some of them use linear constitutive models as simplifications to represent the mechanical properties of soft tissue, such as structures of the IVDs (COBETTO et al., 2018a; KULDUK et al., 2015; NATARAJAN et al., 2018; OTTARDI et al., 2016; ROHLMANN et al., 2006). Others used reaction forces and moments to incorporate IVD behavior into the model, which, while capable of achieving specific goals, do not provide insight into the stresses and displacements occurring within the IVD that would enable the study of a range of pathologies, such as disc degeneration (KAMAL et al., 2019). Other studies use more complex constitutive models with mechanical properties found in the literature (DREISCHARF et al., 2014; ZHONG et al., 2008, 2013). While that is a valid resource to prepare a numerical model, it is widely recognized that there is significant variation of material properties of spinal structures reported in literature, which can influence the biomechanical results observed in the simulations (DREISCHARF et al., 2014; SCHLAGER et al., 2018). Moreover, it has been concluded that calibration methods for the mechanical properties greatly improve the clinical reliability of FE models when compared to simple application of data from literature, especially when studying some kind of defect (DAMM et al., 2019; SCHMIDT et al., 2007).

Nicolini et al. (2022a, 2022b, 2024) have previously calibrated and validated a L1-L2 spinal segment model using stepwise resection experimental data. While this result provided a highly reliable tool for analyzing that specific segment, it was not possible to analyze a whole spinal treatment system, such as VBT, if it encompasses more segments, which is usually the case. This work reports the successful calibration and validation of a thoracolumbar spine (T10-S1), which will become an asset to research groups in the study of VBT instrumentation and other types of spinal implants.

The calibrated and validated thoracolumbar spine model was proven to be robust and reliable, and allowed the inclusion of a VBT system to analyze its effects on the biomechanics of the spine. The first clinically relevant result analyzed was the immediate post-surgical correction. The studied pre-tension configurations were able

to generate a global correction between 11° and 21°, which appears to be slightly inferior to data registered in literature (ABDULLAH et al., 2021; ALANAY et al., 2020; BAKER et al., 2020a; BARONCINI et al., 2021b, 2022; BUYUK et al., 2021; COSTANZO et al., 2022; COURVOISIER et al., 2023; HEDGE et al., 2021; HOERNSCHEMEYER et al., 2020; MARISCAL et al., 2022; MIYANJI et al., 2020; NEWTON et al., 2018, 2020; PEHLIVANOGLU et al., 2020; RAITIO et al., 2022; ROSER et al., 2023; RUSHTON et al., 2021; SAMDANI et al., 2014, 2015; YUCEKUL et al., 2021). However, this difference is still within standard deviation of most studies, which usually included patients with more instrumented segments than considered in this study, and thus the results satisfactorily approximate the expected immediate post-surgical correction in VBT surgery.

The results of immediate post-surgery correction showed that an increase in pre-tension leads to an increase in correction in all segments. This result is consistent with what was found by Nicolini et al. (2022a) and Martin et al. (2023), which both concluded that tether pre-tension is the most important biomechanical parameter to determine scoliotic curve correction.

Another clinically relevant result is the ROM of the instrumented spine, since one of the main advantages of VBT treatment is the preservation of mobility to a larger degree than other traditional treatment methods such as spinal fusion (O'DONNELL et al., 2023). This study's ROM results show that the mobility of the spine is inversely proportional to the tether's pre-tension, which is consistent with the findings of Nicolini et al. (2022a, 2024). Lavelle et al. (2016) have performed cadaveric studies and evaluated the ROM preservation in the T4-T12 spine when tethered with 100 N in each segment. They found mobility preservation of 94±25%, 96±30%, and 61±21% for flexion-extension, axial rotation, and lateral bending, respectively, while in this study, the Conf100N instrumented spine yielded mobility preservation between 73 and 96%, 73 and 87%, and 34 and 36%, respectively. Even though different segments are considered in this study and the one conducted by Lavelle, these studies show similar values of mobility preservation for a VBT instrumented spine, which gives validation to the computational results. This study found that VBT instrumentation was able to preserve at least 45% mobility of the instrumented spine (T10-L3) in flexion-extension and axial rotation for the Conf300N, which is the configuration with the highest pre-tension in the tether at all instrumented segments. In lateral bending, only 18% of the mobility was preserved in the

Conf300N instrumented spine. The ConfGrad configuration resulted in much better mobility, with mobility preservation between 60 and 80% for flexion-extension and axial rotation, and between 26 and 32% for lateral bending. Since ConfGrad is a more clinically accurate pre-tension configuration, and high pre-tensions such as 300 N are usually applied only to the apical segments instead of the whole curve, high mobility preservation is expected from clinical practice (RAITIO et al., 2022).

It is important to notice that screw positioning at each vertebra play a role in determining the biomechanical behavior of the instrumented spine, even if not many studies have been performed to assess this parameter in more depth (COBETTO et al., 2018a). It is not yet clear how screw positioning in different vertebrae may affect the ROM of the spine in different directions, and thus this remains as a possibility for a future study using the thoracolumbar spine model developed in this work, or the scoliotic model that the group aims to develop soon.

While Nicolini et al. (2022a, 2024) have previously reported ROM data for the instrumented spine using a FEM model, it only considered the L1-L2 segment, which despite providing key insights into the interaction of VBT with an individual spinal segment, does not give a broader clinical view of the effects of a whole VBT system in the spine. On the other hand, the present work provides a wider range of data regarding the effects of VBT surgery in the spine, thus providing deeper insight into the clinical scenario where a physician needs to manage surgical parameters of the VBT system to achieve optimal results.

Due to the novelty of the technique, there is still no consensus on the indications of VBT surgery, and the surgical parameters are currently being studied by the scientific community (PARENT; SHEN, 2020). It has been found by several studies that VBT surgery, as is practiced now, has a high rate of complications and reoperations (MARISCAL et al., 2022; RAITIO et al., 2022; ROSER et al., 2023; SHIN et al., 2021; VATKAR et al., 2023; ZHU et al., 2022). Tether breakage is one of the most common, if not the most common, complication in VBT treatment (BARONCINI et al., 2022; GULDENIZ et al., 2023; MARISCAL et al., 2022; RAITIO et al., 2022; ROSER et al., 2023; SHIN et al., 2021; TROBISCH; BARONCINI, 2021; TROBISCH et al., 2022; ZHU et al., 2022). Baroncini et al. (2022), while unsure of the exact biomechanics leading to failure, verified that the main preoperative risk factor for early tether breakage after VBT surgery are a high curve magnitude and limited curve flexibility. Due to these limitations, pediatric surgeons often consider

that patients with scoliotic curvatures greater than  $65^\circ$  and/or stiff curves are not adequate for VBT treatment (ANTONACCI et al., 2021; PHILLIPS et al., 2019). From the mechanical point of view, it is of note that both factors require higher tether tension to effectively correct the scoliotic curve, increasing the risk of cord failure. Guldeniz et al. (2023) studied more deeply the failure mode of tether breakage by submitting single-unit VBT implants to tensile tests and found that the probability that tether breakage occurs due to the damage caused by the locking mechanism in the screw-tether joint is very high. During their quasi-static tensile testing of a VBT single-unit, failure occurred by slippage due to the damage to the cord at the screw-cord connection.

In this study the highest force acting in the PET fiber tether has a magnitude of 420.43 N. The model's tether has a diameter of 4 mm, and thus the highest stress observed in the cord is 33.46 MPa. Data from literature shows that the PET fiber bundle has tensile strength of at least 708 MPa (LECHAT et al., 2006; LECHAT et al., 2010; BAI et al., 2020; GULDENIZ et al., 2023), and therefore it is not likely that tether breakage occurs due to static loading of the cord during motion, even with high pre-tension applications. Fatigue of the tether outside of the screw-tether joint – or at intact parts of the tether – also seems an unlikely cause for failure since the developed stresses are low. However, those force and stress values are close to the ones reported by Guldeniz et al. (2023) when slippage occurred, namely, 582.2 N and 50.4 MPa. The evidence suggests that stress concentration and cord damage at the screw-tether joint play a major role in tether breakage, but there is still not enough data to fully understand this mechanism. Our model simplified the tether as a connector element and did not consider the stress concentration in the screw-cord connection. Moreover, Guldeniz et al. (2023) performed quasi-static tests, not assessing the effects of cyclic loading on the structural integrity of the implant. In order to fully characterize the failure mechanism in tether breakage it is necessary to fully consider the mechanical properties of the implant and the working conditions of the device *in situ*, both experimentally and computationally.

Finally, coupled motion of the VBT instrumented spine has been measured and registered in this work. Although coupled motion of the spine has been studied for decades, there is no consensus on its expected behavior due to conflicting results in literature which likely stem from the complex interactions between osseoligamentous anatomy and muscle, and the different methods for measuring motion



employed by different studies (LEGASPI; EDMOND, 2007; LITTLE et al., 2008). Despite the lack of proper characterization, it is evident that coupled motion is segment-dependent, which is supported by the data published in this work (SHIN et al., 2013; WIDMER et al., 2019).

To the best of the author's knowledge, the only work that has assessed coupled motion due to VBT instrumentation was conducted by Nicolini et al. (2024), where they studied the L1-L2 segment of the spine and concluded that VBT instrumentation generated coupled motion. This study has reached the same conclusion, and studied how coupled motion is altered in each instrumented segment, in the instrumented spine (T10-L3), and in the whole thoracolumbar spine (T10-S1).

Native flexion-extension did not generate coupled motion due to the bilateral symmetry of the spine. However, when instrumented with VBT, the spine presented coupled axial rotation and lateral bending to the side of the implant during flexion and to the concave side during extension. Axial rotation appeared to increase with pre-tension, while lateral bending showed the opposite behavior.

Native axial rotation generated a slight extension and lateral bending to the opposite side of torsion in the T10-L3 segment, but generated flexion and almost no lateral bending when considering the whole thoracolumbar spine model (T10-S1). VBT instrumentation caused lateral bending to the same side of rotation, flexion during right axial rotation, and extension during left axial rotation. Increased with pre-tension seems to increase coupled flexion-extension but decrease coupled lateral bending.

Native lateral bending generated coupled extension and little coupled axial rotation, phenomena which, respectively, increased and decreased when considering T10-S1 rather than only T10-L3. VBT instrumentation caused coupled axial rotation to the same side of bending, flexion during left lateral bending and extension during right lateral bending. However, an increase in pre-tension decreased couple motion, especially in flexion-extension where the Conf300N configuration presented less coupled motion than the native spine.

ConfGrad configuration didn't yield particularly similar behavior to other configurations in none of the cases, but always exhibited intermediate behavior to the configurations with highest and lowest pre-tensions. Native and instrumented

coupled motion was shown to vary across segments, which is consistent with data from literature (SHIN et al., 2013; WIDMER et al., 2019).

It is worth noting that the coupled motion observed in the VBT instrumented spine is often greater, or even opposite to the coupled motion of the native spine. As indicated by Legaspi and Edmond (2007), coupling biomechanics is an important parameter in treatment decision making for physiotherapists, however the inconsistency in reported coupled motion data currently hinders its use. Thus, information on coupled motion is largely relevant to VBT's postoperative recovery.

The postoperative protocol of VBT surgery, as explained by Phillips et al. (2019) and Baker et al. (2020a), allows patients to return to usual daily living activities as soon as they are comfortable, and may return to all activities at six weeks in most cases. Meyers et al. (2021) has reported that the incidence of early (prior to 90 days) postoperative complications is small (3.3%), although data was gathered with patients of a single surgeon. Ergene (2019) has also studied early-term postoperative complications for thoracic VBT surgery, and reached a similar conclusion, with a complication rate of 9.2% and 30-day readmission rate of 1.8%. During the postoperative recovery period, the patient undergoes both respiratory and orthopedic physiotherapy, which play a significant role in ensuring complete and faster rehabilitation (ERGENE, 2019; BARONCINI et al., 2021a). Despite not offering a definitive solution to the uncertainty regarding the coupling biomechanics of the spine due to the model's limitations, such as lack of musculoskeletal interactions, and the intrinsic limitations of computational models, this study provides valuable insight into the effects of VBT instrumentation on the biomechanics of the spine. The appearance of unnatural coupled motion can lead to overloading of anatomical structures and muscles due to compensation, and thus this information can better prepare physiotherapists to make appropriate treatment decisions regarding VBT's postoperative recovery, since the analysis in this work indicates how a VBT instrumented spine is expected to behave when compared to the native spine.

## 5.1 LIMITATIONS AND FUTURE WORK

Despite the success of the validation and calibration of the model, the model still has many opportunities for improvement. The mechanical properties of the IVDs and ligaments of the model were obtained based on the experimental resection

studies of the L1-L2 segment of the spine, varying these properties in other segments to better reflect ROM data from literature. While the results were satisfactory, resection studies on each segment of the thoracolumbar spine would be ideal to provide a more precise calibration tool for the model. However, due to the difficulty in obtaining cadaveric spines to perform this kind of study, this remains as a possibility for the future without an appropriate estimation of viability.

Another point for improvement of the model relates to the geometry of the spine model. This spine model depicts a healthy spine from a young man, and thus do not adequately represent pathologies that should be considered in more specific clinical studies. There are currently models that not only include the scoliotic geometry into the spine, but even includes growth modulation models to study the spine's geometry change across time while instrumented with VBT (COBETTO et al., 2018a, 2018b, 2018c). Some models also include other structures, such as the rib cage and other bone structures for thoracic models, or muscles that are connected to the spine in various segments (COBETTO et al., 2018a, 2018b, 2018c; KAMAL et al., 2019; ROHLMANN et al., 2006). The possibility of including more pertinent structures, features related to modulated growth models and incorporating specific spine pathologies to the model are a current objective of the study group. Particularly for the VBT biomechanical analysis, the group aims to generate a new scoliotic geometry that will allow other clinically relevant studies to be performed as a natural next step, include verifying whether the conclusions reached in this work related to post-surgical correction, ROM, tether forces, and coupled motion are sustained in a study with a scoliotic spine model.

Long-term correction in VBT treatment happens due to the growth modulation governed by the Hueter-Volkman's law (MARISCAL et al., 2022; STOKES et al., 1996). This model makes it possible to calculate the stresses acting on the endplates of the vertebrae, which is crucial information to estimate and model the growth rate and modulation (COBETTO et al., 2018a, 2018b, 2018c; KAMAL et al., 2019; MARTIN et al., 2023; NICOLINI et al., 2024; STOKES et al., 2006; STOKES, 2007; VILLEMURE; STOKES, 2009). This is an important first step in the construction of a more advanced model that would allow a deeper understanding of the biomechanics of the spine and the causes for adverse events such as overcorrection, undercorrection, and tether breakage. Such understanding may lead to the design of better products for VBT surgery and better instructed surgeons who

will know how to deal with each variable during the surgical procedure to lead to an optimal result. Cobetto et al. (2018a, 2018b, 2018c) and Martin et al. (2023) have used patient-specific spine models instrumented with VBT to predict correction and study relevant parameters in providing adequate correction to the spine, which shows the clinical potential of computational models. The incorporation of growth into the spine model is among the next planned steps to advance the thoracolumbar spine model.

Another aspect that was not included within the scope of this study is the musculoskeletal consequences of the unnatural coupling biomechanics of the VBT instrumented spine. That is because it is uncertain whether certain motions happen due to extra tensioning in the tether, relaxation of the tether or just an anatomical adjustment to enable the instrumented spine to reach equilibrium. The inclusion of muscles into the computational model would be highly beneficial to properly characterize this phenomenon. While this model provides health professionals with a general idea of the structures which may be affected by unnatural coupled motion, the inclusion of muscles would allow for a more in-depth analysis of what is happening in each structure. Despite the low incidence of postoperative early-term complications in VBT surgery, it would still be beneficial to study whether there are aspects to improve during rehabilitation to make it better and safer, as well as the potential to utilize such knowledge to improve physiotherapy practice in general.

Finite Element Analysis has been increasingly popular to evaluate the mechanical behavior of implants and segments of the body due to its capacity to reliably simulate real anatomic structures (KULDUK et al., 2015; COBETTO et al., 2018b; YING et al., 2023). Despite the potential of these models to better understand the biomechanics of specific systems and phenomena, there are many more applications of technology to improve clinical and surgical practice. One example is the work of Cobetto et al. (2018b) where they developed a FEM based tool to plan VBT surgery based on patient-specific geometry. While this type of tool is desirable and useful for surgical planning, complex FEM models usually require a long time to run which limits clinical applicability for situations that require real-time response, such as computer assisted surgery (PHELLAN et al., 2020). In order to bypass this problem, many real-time models have been created by training machine learning models with data from FEM-based simulations in order to obtain faster response while maintaining reliable characterization of anatomical structures, such as breast

tissue and the liver (MARTÍNEZ-MARTÍNEZ et al., 2017; PELLICER-VALERO et al., 2020; PHELLAN et al., 2020). This technique is applicable to various clinical fields and could be used to assist VBT surgery planning in the future.

Machine learning and artificial intelligence (AI) have been playing a major role in scientific advancement in the most diverse areas, including the medical field and VBT treatment. Mulford et al. (2023), for example, have developed a deep learning algorithm for measuring interscrew angle after VBT surgery so that tether breakage can be more accurately diagnosed and in reduced time. Nevertheless, the potential of AI extends beyond the field of diagnostics and surgical planning. It has also been increasingly used in implant design optimization (REVILLA-LEÓN et al., 2023). Roy et al. (2018), for example, has combined the application of FE analysis to an artificial neural networks model to achieve optimum design of patient specific dental implant. Chatterjee et al. (2019) has done the same for femoral implants. Having these works as basis, it would likely be viable to use FE models and AI to optimize VBT implants and surgery simultaneously. It could even be used to make a new calibration of the mechanical properties of the spine model using a trained artificial neural network model that replicated the results of FE models as an objective function so the process could be performed more efficiently.

There is still much room for development in the understanding and planning of VBT surgery, and exciting technologies can be used for that. Future works will explore these possibilities while aiming to optimize patient care and recovery.

## 6 CONCLUSION

The aim of this work was to develop a reliable thoracolumbar spine model (T10-S1) for use in biomechanical studies and to perform a case study of how VBT instrumentation affects the biomechanics of the spine.

As reported in Section 4.1, a reliable and robust model of the thoracolumbar spine was obtained. The mechanical properties of the intervertebral discs were calibrated, and the resulting biomechanical behavior of the spine validated. Thus, the first objective of this work was properly achieved, and the model will be available for use to evaluate the effects of a variety of spine implants.

The other main results shown in Section 4 relate to the effects of VBT instrumentation on the biomechanics of the spine. It has been shown that increased tether tension increases immediate postoperative curve correction and reduces ROM, both in individual segments and in the whole instrumented spine. Moreover, each segment is affected in a specific way, which should be considered by surgeons and physiotherapists.

The forces acting on the tether during flexion-extension, axial rotation, and lateral bending have been analyzed, and the stresses observed do not surpass the tensile strength of PET – the tether’s material. Thus, tether breakage, which is one of the most common adverse events in VBT surgery, likely doesn’t stem from static mechanical failure. Though, it is important to remark that the biomechanical loads acting on the spine vary depending on the spinal region of interest and may be superior to the 5 Nm used in this work. Studies suggest that failure occurs most likely due to damage and stress concentration in the tether at the screw-tether joint (GULDENIZ et al., 2023), but not enough data has been gathered yet to fully support this claim.

Coupled motion in the native spine have also been studied, along with the effect VBT instrumentation has on it. While there is no consensus in literature on how the coupling biomechanics of the spine is manifested, this work was able to provide both extra data to help in this characterization and a direct comparison of how VBT instrumentation will influence this aspect of spine biomechanics. This data is highly relevant to physiotherapists, which will be responsible for ensuring proper recovery and return to all activities.

Finally, various possibilities for further studies have been presented in Section 5. The research group is currently working on generating a scoliotic spine model and scaling it to better represent the spine of a child. There are also projects related to the application of AI models to study the biomechanics of the spine. Single-cord VBT is only one of the possible configurations that exist. There is also double-cord and hybrid – which is a combination of VBT with spinal fusion – techniques. Future studies from the group will also study how these different configurations affect the biomechanics of the spine.

Despite the large volume of data generated and analyzed in this work, there are more aspects of VBT instrumentation which will also be further analyzed in the future. These aspects include intradiscal pressure and stress at the facet joints, which are important parameters in preventing diseases and injury.

The objectives of this work have been achieved, and further research from the group will be focused on pursuing full understanding of the effects all different configurations of VBT instrumentation have on the biomechanics of the spine, how to ensure patient recovery and well-being, and how to prevent the most common adverse events associated with VBT surgery.

## REFERENCES

ABDULLAH, A. *et al.* Risk of early complication following anterior vertebral body tethering for idiopathic scoliosis. **Spine Deformity**, v. 9, n. 5, p. 1419–1431, 9 abr. 2021. Available in: <https://doi.org/10.1007/s43390-021-00326-2>. Access in: 24 jan. 2024.

ALANAY, A. *et al.* Thoracoscopic vertebral body tethering for adolescent idiopathic scoliosis. **Spine**, v. Publish Ahead of Print, 1 ago. 2020. Available in: <https://doi.org/10.1097/BRS.0000000000003643>. Access in: 02 fev. 2024.

ALMEER, G. *et al.* Anatomy and pathology of facet joint. **Journal of Orthopaedics**, v. 22, p. 109–117, nov. 2020. Available in: <https://doi.org/10.1016/j.jor.2020.03.058>. Access in: 05 mar. 2024.

ANTONACCI, Christopher L. *et al.* Treatment of patients with scoliosos using a unique anterior scoliosis correction technique. **Medical Research Archives**, v. 9, n. 7, p. 2-12, 2021. Available in: <https://doi.org/10.18103/mra.v9i7.2463>. Access in: 10 abr. 2024.

ANTONACCI, M. *et al.* Treatment for an adult patient with slowly progressive idiopathic scoliosis using a unique anterior scoliosis correction technique: a case report. **Medical Research Archives**, v. 10, n. 12, p. 327-345, 2022. Available in: <https://doi.org/10.18103/mra.v10i12.3345>. Access in: 10 jan. 2024.

ASHER, M. A.; BURTON, D. C. Adolescent idiopathic scoliosis: natural history and long term treatment effects. **Scoliosis**, v. 1, n. 1, 31 mar. 2006. Available in: <https://doi.org/10.1186/1748-7161-1-2>. Access in: 02 abr. 2024.

ATLAS of anatomy. Thieme Medical Publishers. 2020.

BAI, Yu-Lei *et al.* Quasi-static and dynamic tensile properties of large-rupture-strain (LRS) polyethylene terephthalate fiber bundle. **Construction and Building Materials**, v. 232, p. 117241–117241, 1 jan. 2020. Available in: <https://doi.org/10.1016/j.conbuildmat.2019.117241>. Access in: 07 fev. 2024.

BAKER, C. E.; KIEBZAK, G. M.; NEAL, K. M. Anterior vertebral body tethering shows mixed results at 2-year follow-up. **Spine Deformity**, v. 9, n. 2, p. 481–489, 28 out. 2020a. Available in: <https://doi.org/10.1007/s43390-020-00226-x>. Access in: 05 mar. 2024.

BAKER, C. *et al.* Anterior Lumbar Vertebral Body Tethering in Adolescent Idiopathic Scoliosis. **Journal of the Pediatric Orthopaedic Society of North America**, v. 2, n. 3, 1 nov. 2020. Available in: <https://doi.org/10.55275/JPOSNA-2020-145>. Access in: jan. 2024.

BAKER, C. E.; MILBRANDT, T. A.; LARSON, A. N. Anterior vertebral body tethering for adolescent idiopathic scoliosis. **Orthopedic Clinics of North America**,



v. 52, n. 2, p. 137–147, abr. 2021. Available in: <http://dx.doi.org/10.1016/j.ocl.2021.01.003>. Access in: 28 abr. 2024.

BARONCINI, Alice; TROBISCH, Per David; MIGLIORINI, Filippo. Learning curve for vertebral body tethering: analysis on 90 consecutive patients. **Spine Deformity**, v. 9, n. 1, p. 141-147, 2020. Available in: <http://dx.doi.org/10.1007/s43390-020-00191-5>. Access in: 15 fev. 2024.

BARONCINI, Alice. *et al.* Return to sport and daily life activities after vertebral body tethering for AIS: analysis of the sport activity questionnaire. **European Spine Journal**, v. 30, n. 7, p. 1998-2006, 2021a. Available in: <http://dx.doi.org/10.1007/s00586-021-06768-6>. Access in: 24 dez. 2023.

BARONCINI, Alice *et al.* The effects of vertebral body tethering on sagittal parameters: evaluations from a 2-years follow-up. **European Spine Journal**, v. 31, n. 4, p. 1060–1066, 15 dez. 2021b. Available in: <https://doi.org/10.1007/s00586-021-07076-9>. Access in: 09 mar. 2024.

BARONCINI, A. *et al.* Analysis of the risk factors for early tether breakage following vertebral body tethering in adolescent idiopathic scoliosis. **European Spine Journal**, 4 maio 2022. Available in: <https://doi.org/10.1007/s00586-022-07231-w>. Access in: 04 mar. 2024.

BECKMANN, A. *et al.* A new in vitro spine test rig to track multiple vertebral motions under physiological conditions. **Biomedizinische Technik**, v. 63, n. 4, p. 341–347, 27 abr. 2017. Available in: <https://doi.org/10.1515/bmt-2016-0173>. Access in: 28 abr. 2024.

BECKMANN, A. *et al.* Biomechanical testing of a polycarbonate-urethane-based dynamic instrumentation system under physiological conditions. **Clinical Biomechanics**, v. 61, p. 112–119, 1 jan. 2019a. Available in: <https://doi.org/10.1016/j.clinbiomech.2018.12.003>. Access in: 10 mar. 2024.

BECKMANN, A. *et al.* Biomechanical in vitro test of a novel dynamic spinal stabilization system incorporating polycarbonate urethane material under physiological conditions. **Journal of Biomechanical Engineering**, v. 142, n. 1, 1 out. 2019b. Available in: <https://doi.org/10.1115/1.4044242>. Access in: 08 mar. 2024.

BERMEL, E. A.; BAROCAS, V. H.; ELLINGSON, A. M. The role of the facet capsular ligament in providing spinal stability. **Computer Methods in Biomechanics and Biomedical Engineering**, v. 21, n. 13, p. 712–721, 2018. Available in: [10.1080/10255842.2018.1514392](https://doi.org/10.1080/10255842.2018.1514392). Access in: 18 jan. 2024.

BERNARD, J. *et al.* Dual modality of vertebral body tethering: anterior scoliosis correction versus growth modulation with mean follow-up of five years. **Bone & Joint Open**, v. 3, n. 2, p. 123–129, 1 fev. 2022. Available in: <https://doi.org/10.1302/2633-1462.32.BJO-2021-0120.R1>. Access in: 01 fev. 2024.

BIZZOCA, D. *et al.* Anterior vertebral body tethering for idiopathic scoliosis in growing children: a systematic review. **World Journal of Orthopedics**, v. 13, n. 5, p. 481–493, 18 maio 2022. Available in: [10.5312/wjo.v13.i5.481](https://doi.org/10.5312/wjo.v13.i5.481). Access in: may 2024.

BOUDISSA, M. *et al.* Early outcomes of spinal growth tethering for idiopathic scoliosis with a novel device: a prospective study with 2 years of follow-up. **Child's Nervous System**, v. 33, n. 5, p. 813–818, 21 mar. 2017. Available in: <https://doi.org/10.1007/s00381-017-3367-4>. Access in: 01 abr. 2024.

BURWELL, R. G. *et al.* Adolescent idiopathic scoliosis (AIS): a multifactorial cascade concept for pathogenesis and embryonic origin. **Scoliosis and Spinal Disorders**, v. 11, n. 1, 30 jan. 2016. Available in: <https://doi.org/10.1186/s13013-016-0063-1>. Access in: 05 abr. 2024.

BUYUK, Abdul Fettah *et al.* Does preoperative and intraoperative imaging for anterior vertebral body tethering predict postoperative correction? **Spine Deformity**, v. 9, n. 3, p. 743–750, 22 jan. 2021. Available in: <https://doi.org/10.1007/s43390-020-00267-2>. Access in: 19 abr. 2024.

CARREGARO, R. L.; DA SILVA, E. N.; VAN TULDER, M. Direct healthcare costs of spinal disorders in Brazil. **International Journal of Public Health**, v. 64, n. 6, p. 965–974, 15 maio 2019. Available in: <https://doi.org/10.1007/s00038-019-01211-6>. Access in: 02 mar. 2024.

CARREGARO, R. L. *et al.* Low back pain should be considered a health and research priority in Brazil: Lost productivity and healthcare costs between 2012 to 2016. **PLOS ONE**, v. 15, n. 4, p. e0230902, 1 abr. 2020. Available in: [10.1371/journal.pone.0230902](https://doi.org/10.1371/journal.pone.0230902). Access in: may 2024.

CATANZANO, A. A. *et al.* Spontaneous lumbar curve correction following vertebral body tethering of main thoracic curves. **Journal of bone and joint surgery. American volume/The Journal of bone and joint surgery**, v. 104, n. 18, p. 1629–1638, 18 jul. 2022. Available in: <http://dx.doi.org/10.2106/JBJS.21.01500>. Access in: 08 abr. 2024.

CEBECI, Barbaros Omer *et al.* Non-fusion growth modulation with anterior vertebral body tethering for adolescent idiopathic scoliosis: a promising minimal invasive alternative to traditional treatment. **European Spine Journal**, v. 26, n. S2, p. 251–291, set. 2017. Available in: [10.1016/j.spinee.2017.07.089](https://doi.org/10.1016/j.spinee.2017.07.089). Access in: may 2024.

CHATTERJEE, Subhomoy *et al.* Computational intelligence based design of implant for varying bone conditions. **International Journal for Numerical Methods in Biomedical Engineering**, v. 35, n. 6, p. 327-345, 2019. Available in: <http://dx.doi.org/10.1002/cnm.3191>. Access in: 15 dez. 2023.

CHEN, H.C. *et al.* Biomechanical evaluation of a novel pedicle screw-based interspinous spacer: a finite element analysis. **Medical Engineering & Physics**, v. 46, p. 27–32, 1 ago. 2017. Available in: <http://dx.doi.org/10.1016/j.medengphy.2017.05.004>. Access in: 11 abr. 2024.

CHENG, Alexander H.-D. **Poroelasticity**. Mississippi: Springer, 2016.

COBETTO, N.; PARENT, S.; AUBIN, C.-E. 3D correction over 2 years with anterior vertebral body growth modulation: A finite element analysis of screw positioning, cable tensioning and postoperative functional activities. **Clinical Biomechanics**, v. 51, p. 26–33, jan. 2018a. Available in: <https://doi.org/10.1016/j.clinbiomech.2017.11.007>. Access in: 19 mar. 2024.

COBETTO, N.; AUBIN, C.-E.; PARENT, S. Surgical planning and follow-up of anterior vertebral body growth modulation in pediatric idiopathic scoliosis using a patient-specific finite element model integrating growth modulation. *Spine Deformity*, v. 6, n. 4, p. 344–350, jul. 2018b. Available in: <https://doi.org/10.1016/j.jspd.2017.11.006>. Access in: 18 abr. 2024.

COBETTO, N.; AUBIN, C.-E.; PARENT, S. Contribution of Lateral Decubitus Positioning and Cable Tensioning on Immediate Correction in Anterior Vertebral Body Growth Modulation. **Spine Deformity**, v. 6, n. 5, p. 507–513, set. 2018c. Available in: <https://doi.org/10.1016/j.jspd.2018.01.013>. Access in: 15 mar. 2024.

COSTANZO, S. *et al.* Video-Assisted Thoracoscopy for Vertebral Body Tethering of Juvenile and Adolescent Idiopathic Scoliosis: Tips and Tricks of Surgical Multidisciplinary Management. **Children**, v. 9, n. 1, p. 74–74, 5 jan. 2022. Available in: <https://doi.org/10.3390/children9010074>. Access in: 07 jan. 2024.

COURVOISIER, Aurélien *et al.* Vertebral body tethering in AIS Management—a preliminary report. **Children**, v. 10, n. 2, p. 192–192, 20 jan. 2023. Available in: <https://doi.org/10.3390/children10020192>. Access in: 09 jan. 2024.

COUVERTIER, M. *et al.* Biomechanical analysis of the thoracolumbar spine under physiological loadings: Experimental motion data corridors for validation of finite element models. Proceedings of the Institution of Mechanical Engineers. Part H, **Journal of Engineering in Medicine**, v. 231, n. 10, p. 975–981, 14 jul. 2017. Available in: <https://doi.org/10.1177/0954411917719740>. Access in: 05 fev. 2024.

CRAMER, Gregory D. DARBY, Susan A. **Clinical anatomy of the spine, spinal cord, and ANS**. Missouri: Elsevier, 2014.

CRAWFORD, C. H.; LENKE, L. G. Growth modulation by means of anterior tethering resulting in progressive correction of juvenile idiopathic scoliosis: a case report. **The Journal of Bone and Joint Surgery**. American Volume, v. 92, n. 1, p. 202–209, 1 jan. 2010. Available in: <https://doi.org/10.2106/JBJS.H.01728>. Access in: 01 abr. 2024.

DAMM, N.; ROCKENFELLER, R.; GRUBER, K. Lumbar spinal ligament characteristics extracted from stepwise reduction experiments allow for preciser modeling than literature data. **Biomechanics and Modeling in Mechanobiology**, v. 19, n. 3, p. 893–910, 2 dez. 2019. Available in: <https://doi.org/10.1007/s10237-019-01259-6>. Access in: 25 abr. 2024.

DREISCHARF, M. *et al.* Comparison of eight published static finite element models of the intact lumbar spine: predictive power of models improves when combined together. **Journal of Biomechanics**, v. 47, n. 8, p. 1757–1766, 3 jun. 2014. Available in: <https://doi.org/10.1016/j.jbiomech.2014.04.002>. Access in: 06 mar. 2024.

ERGENE, G. Early-term postoperative thoracic outcomes of videothoracoscopic vertebral body tethering surgery. **The Turkish Journal of Thoracic and Cardiovascular Surgery**, v. 27, n. 4, p. 526–531, 2019. Available in: [10.5606/tgkdc.dergisi.2019.17889](https://doi.org/10.5606/tgkdc.dergisi.2019.17889). Access in: 30 nov. 2023.

FISH, Jacob; BELYTSCHKO, Ted. **A first course in finite elements**. Chichester: John Wiley & Sons, 2007.

FON, Gerald T. PITT, Michael J. THIES JR. A. Cole. **Thoracic kyphosis: range in normal subjects**. AJR. 1980.

FORSBERG, D. *et al.* Fully automatic measurements of axial vertebral rotation for assessment of spinal deformity in idiopathic scoliosis. **Physics in Medicine & Biology/Physics in Medicine and Biology**, v. 58, n. 6, p. 1775–1787, 26 fev. 2013. Available in: [doi:10.1088/0031-9155/58/6/1775](https://doi.org/10.1088/0031-9155/58/6/1775). Access in: 30 abr. 2024.

GASSER, T. C.; OGDEN, R. W.; HOLZAPFEL, G. A. Hyperelastic modelling of arterial layers with distributed collagen fibre orientations. **Journal of The Royal Society Interface**, v. 3, n. 6, p. 15–35, 28 set. 2005. Available in: <https://doi.org/10.1098/rsif.2005.0073>. Access in: 10 abr. 2024.

GERMANEAU A. *et al.* A novel approach for biomechanical spine analysis: mechanical response of vertebral bone augmentation by kyphoplasty to stabilise thoracolumbar burst fractures. **Journal of the mechanical behavior of biomedical materials/Journal of mechanical behavior of biomedical materials**, v. 59, p. 291–303, 1 jun. 2016. Available in: <http://dx.doi.org/10.1016/j.jmbbm.2016.02.002>. Access in: 01 abr. 2024.

GILROY, Anne M. (ed.) **Atlas of anatomy**. 4 ed. Thieme Medical Publishers. 2020.

GUAN, Y. *et al.* Moment–rotation responses of the human lumbosacral spinal column. **Journal of Biomechanics**, v. 40, n. 9, p. 1975–1980, jan. 2007. Available in: <http://dx.doi.org/10.1016/j.jbiomech.2006.09.027>. Access in: 20 mar. 2024.

GULDENIZ, Ogulcan *et al.* Biomechanics of the tether breakage: tensile behaviour of a single-unit vertebral body tethering construct. **Spine Deformity**, v. 11, n. 4, p. 825–831, 10 fev. 2023. Available in: <https://doi.org/10.1007/s43390-023-00657-2>. Access in: 28 fev. 2024.

GURTIN, Morton E. **An introduction to continuum mechanics**. New York: Academic Press, 1981.

GURTIN, Morton E. *et al.* **The mechanics and thermodynamics of continua**. New York: Cambridge University Press, 2010.

HALDEMAN, Scott *et al.* **An atlas of back pain**. London: The Parthenon Publishing Group, 2002.

HAMILL, Joseph *et al.* **Bases biomecânicas do movimento humano**. Barueri, SP: Manole, 2016.

HEGDE, S. K. *et al.* Efficacy of anterior vertebral body tethering in skeletally mature children with adolescent idiopathic scoliosis: a preliminary report. **International Journal of Spine Surgery**, v. 15, n. 5, p. 995–1003, 22 set. 2021. Available in: <https://doi.org/10.14444/8122>. Access in: 25 abr. 2024.

HERRING, John A. **Tachdjian's pediatric orthopaedics: from the Texas scottish rite hospital for children**, vol. 2. Philadelphia: Elsevier Saunders, 2022.

HEUER, F. *et al.* Stepwise reduction of functional spinal structures increase range of motion and change lordosis angle. **Journal of Biomechanics**, v. 40, n. 2, p. 271–280, 2007. Available in: <http://dx.doi.org/10.1016/j.jbiomech.2006.01.007>. Access in: 24 jan. 2024.

HOERNSCHEMEYER, D. G. *et al.* Anterior vertebral body tethering for adolescent scoliosis with growth remaining. **Journal of Bone and Joint Surgery**, v. Publish Ahead of Print, 21 abr. 2020. Available in: <http://dx.doi.org/10.2106/JBJS.19.00980>. Access in: 13 jan. 2024.

HOERNSCHEMEYER, D. G. *et al.* Bilateral vertebral body tethering: identifying key factors associated with successful outcomes. **European spine journal**, v. 33, n. 2, p. 723–731, 5 jan. 2024. Available in: <https://doi.org/10.1007/s00586-023-08074-9>. Access in: 05 abr. 2024.

HOLZAPFEL, G. A. *et al.* Single lamellar mechanics of the human lumbar anulus fibrosus. **Biomechanics and Modeling in Mechanobiology**, v. 3, n. 3, p. 125–140, 8 out. 2004. Available in: <https://doi.org/10.1007/s10237-004-0053-8>. Access in: 05 abr. 2024.

HOLZAPFEL, G. A.; GASSER, T. C.; OGDEN, R. W. A new constitutive framework for arterial wall mechanics and a comparative study of material models. **Journal of Elasticity**, v. 61, n. 1/3, p. 1–48, 2000. Available in: <https://doi.org/10.1023/A:1010835316564>. Access in: 28 abr. 2024.

HOLZAPFEL, G. A.; OGDEN, R. W. Constitutive modelling of arteries. **Proceedings of the Royal Society A: Mathematical, Physical and Engineering Sciences**, v. 466, n. 2118, p. 1551–1597, 31 mar. 2010. Available in: <https://doi.org/10.1098/rspa.2010.0058>. Access in: 25 mar. 2024.

HOLZAPFEL, Gerhard E. **Nonlinear solid mechanics: a continuum approach for engineering**. Chichester: John Wiley & Sons, 2000.

JARAMILLO, Héctor Henrique *et al.* Characterization of the L4–L5–S1 motion segment using the stepwise reduction method. **Journal of Biomechanics**, v. 49, n. 7, p. 1248–1254, 3 maio 2016. Available in: <http://dx.doi.org/10.1016/j.jbiomech.2016.02.050>. Access in: 08 abr. 2024.

KADO, D. M. Narrative review: hyperkyphosis in older persons. **Annals of Internal Medicine**, v. 147, n. 5, p. 330, 4 set. 2007. Available in: <https://doi.org/10.7326/0003-4819-147-5-200709040-00008>. Access in: 02 abr. 2024.

KAMAL, Z. *et al.* A stability-based model of a growing spine with adolescent idiopathic scoliosis: A combination of musculoskeletal and finite element approaches. **Medical engineering & physics**, v. 64, p. 46–55, 1 fev. 2019. Available in: <https://doi.org/10.1016/j.medengphy.2018.12.015>. Access in: 05 abr. 2024.

KARAVIDAS, N. Bracing in the treatment of adolescent idiopathic scoliosis: evidence to date. **Adolescent Health, Medicine and Therapeutics**, v. 10, p. 153–172, out. 2019. Available in: <http://doi.org/10.2147/AHMT.S190565>. Access in: 02 abr. 2024.

KATZ, J. N. Lumbar disc disorders and low-back pain: socioeconomic factors and consequences. **The Journal of Bone and Joint Surgery (American)**, v. 88, n. suppl\_2, p. 21, 1 abr. 2006. Available in: <https://doi.org/10.2106/JBJS.E.01273>. Access in: 02 abr. 2024.

KIM, Daniel H. *et al.* **Surgery of the pediatric spine**. New York: Thieme Medical Publishers, 2008.

KLYCE, W. *et al.* Pedicle screw plowing in adolescent idiopathic scoliosis. **Spine (Philadelphia, Pa. 1976)/Spine**, v. 47, n. 12, p. 873–878, 21 set. 2021. Available in: <http://dx.doi.org/10.1097/BRS.0000000000004252>. Access in: 28 jan. 2024.

KONIECZNY, M. R.; SENYURT, H.; KRAUSPE, R. Epidemiology of adolescent idiopathic scoliosis. **Journal of Children's Orthopaedics**, v. 7, n. 1, p. 3–9, fev. 2013. Available in: <https://doi.org/10.2106/JBJS.E.01273>. Access in: 03 abr. 2024.

KOWALSKI, R. J.; FERRARA, L. A.; BENZEL, E. C. Biomechanics of the Spine. **Neurosurgery Quarterly**, v. 15, n. 1, p. 42–59, mar. 2005. Available in: <https://doi.org/10.1097/01.wnq.0000152406.39871.8e>. Access in: 03 abr. 2024.

KULDUK, Ahmet *et al.* Biomechanical comparison of effects of the dynesys and coflex dynamic stabilization systems on range of motion and loading characteristics in the lumbar spine: a finite element study. **International Journal of Medical Robotics and Computer Assisted Surgery**, v. 11, n. 4, p. 400–405, 23 jan. 2015. Available in: <https://doi.org/10.1002/rcs.1636>. Access in: 02 mar. 2024.

LAVELLE, W. F. *et al.* An initial biomechanical investigation of fusionless anterior tether constructs for controlled scoliosis correction. **The Spine Journal**, v.

16, n. 3, p. 408–413, mar. 2016. Available in: <http://dx.doi.org/10.1016/j.spinee.2015.11.004>. Access in: 28 abr. 2024.

LECHAT, C. *et al.* Mechanical behaviour of polyethylene terephthalate & polyethylene naphthalate fibres under cyclic loading. **Journal of Materials Science**, v. 41, n. 6, p. 1745–1756, mar. 2006. Available in: <https://doi.org/10.1007/s10853-006-2372-x>. Access in: 21 fev. 2024.

LECHAT, C.; BUNSELL, A. R.; DAVIES, P. Tensile and creep behaviour of polyethylene terephthalate and polyethylene naphthalate fibres. **Journal of Materials Science**, v. 46, n. 2, p. 528–533, 30 out. 2010. Available in: <https://doi.org/10.1007/s10853-010-4999-x>. Access in: 16 fev. 2024.

LEGASPI, Owen; EDMOND, Susan L. **Does the evidence support the existence of lumbar spine coupled motion?** a critical review of the literature. *Journal of Orthopaedic & Sports Physical Therapy*, v. 37, n. 4, p. 169–178, 2007. Available in: <https://doi.org/10.2519/jospt.2007.2300>. Access in: 16 jan. 2024.

LITTLE, J. P. *et al.* Are coupled rotations in the lumbar spine largely due to the osseo-ligamentous anatomy? A modeling study. **Computer Methods in Biomechanics and Biomedical Engineering**, v. 11, n. 1, p. 95–103, 2008. Available in: <https://doi.org/10.1080/10255840701552143>. Access in: 09 dez. 2023.

MACKEY, C. *et al.* Magnetically Controlled Growing Rods (MCGR) Versus Single Posterior Spinal Fusion (PSF) Versus Vertebral Body Tether (VBT) in Older Early Onset Scoliosis (EOS) Patients. **Spine (Philadelphia, Pa. 1976)/Spine**, v. 47, n. 4, p. 295–302, 1 out. 2021. Available in: <https://doi.org/10.1097/BRS.0000000000004245>. Access in: 25 jan. 2024.

MAGEE, David J. MANSKE, Robert C. **Orthopedic physical assessment**. Missouri: Elsevier, 2021.

MALVERN, Lawrence E. **Introduction to the mechanics of a continuous medium**. New Jersey: Prentice Hall, 1969.

MARISCAL, G. *et al.* Meta-analysis on the efficacy and safety of anterior vertebral body tethering in adolescent idiopathic scoliosis. **European spine journal**, v. 32, n. 1, p. 140–148, 29 nov. 2022. Available in: <https://doi.org/10.1007/s00586-022-07448-9>. Access in: 02 fev. 2024.

MARTIN, S. *et al.* Biomechanical modeling and assessment of lumbar vertebral body tethering configurations. **Spine Deformity**, v. 11, n. 5, p. 1041–1048, 2023. Available in: <https://doi.org/10.1007/s43390-023-00697-8>. Access in: 18 nov. 2023.

MARTÍNEZ-MARTÍNEZ, F. *et al.* A finite element-based machine learning approach for modeling the mechanical behavior of the breast tissues under compression in real-time. **Computers in Biology and Medicine**, v. 90, p. 116–124, nov. 2017. Available in: <https://doi.org/10.1016/j.combiomed.2017.09.019>. Access in: 17 nov. 2023.

MARUYAMA, T. *et al.* Conservative treatment for adolescent idiopathic scoliosis: can it reduce the incidence of surgical treatment? **Pediatric Rehabilitation**, v. 6, n. 3-4, p. 215–219, jul. 2003. Available in: <https://doi.org/10.1080/13638490310001642748>. Access in: 03 abr. 2024.

MAYO, Nancy E. *et al.* The ste-justine adolescent idiopathic scoliosis cohort study: part III back pain. **Spine**, v. 19, n. 14. 1994.

MENDONÇA, A. G. *et al.* Custos diretos da dor lombar em hospitais financiados pelo Sistema Único de Saúde. **Revista Pesquisa em Fisioterapia**, v. 11, n. 1, p. 181–189, 21 jan. 2021. Available in: <https://doi.org/10.17267/2238-2704rpf.v11i1.3438>. Access in: 28 abr. 2024.

MEYERS, J. *et al.* Early operative morbidity in 184 cases of anterior vertebral body tethering. **Scientific Reports**, v. 11, n. 1, 29 nov. 2021. Available in: <https://doi.org/10.1038/s41598-021-02358-0>. Access in: 18 jan. 2024.

MIYANJI, F. *et al.* Safety and efficacy of anterior vertebral body tethering in the treatment of idiopathic scoliosis. **The Bone & Joint Journal**, v. 102-B, n. 12, p. 1703–1708, 1 dez. 2020. Available in: <https://doi.org/10.1302/0301-620X.102B12.BJJ-2020-0426.R1>. Access in: 19 abr. 2024.

MIYANJI, Firoz; PARENT, S. Anterior vertebral body tethering (AVBT) for early-onset scoliosis. **Springer eBooks**, p. 117–134, 27 nov. 2017. Available in: [https://doi.org/10.1007/978-3-319-71580-3\\_10](https://doi.org/10.1007/978-3-319-71580-3_10). Access in: 30 abr. 2024.

MLADENOV, K.; STUCKER, R. Anterior vertebral body tethering (VBT) for idiopathic scoliosis. 2021. In: 16th German Spine Congress Annual Meeting of the German Spine Society 9th to 11th December 2021 Muenster, Germany. **European Spine Journal**, v. 30, n. 11, p. 3328–3414, 16 out. 2021. Available in: <https://doi.org/10.1007/s00586-021-07017-6>. Access in: 16 dez. 2023.

MOON, S. M. *et al.* Evaluation of intervertebral disc cartilaginous endplate structure using magnetic resonance imaging. **European Spine Journal**, v. 22, n. 8, p. 1820–1828, 1 ago. 2013. Available in: <https://doi.org/10.1007/s00586-013-2798-1>. Access in: 04 abr. 2024.

MORAMARCO, Marc (org). **Schroth's textbook of scoliosis and other spinal deformities**. England: Cambridge Scholars Publishing, 2020.

MULFORD, K. L. *et al.* Automated measurements of interscrew angles in vertebral body tethering patients with deep learning. **The Spine journal/The spine journal**, 1 set. 2023. Available in: <https://doi.org/10.1016/j.spinee.2023.09.011>. Access in: 02 dez. 2023.

NATARAJAN, R. N.; WATANABE, K.; HASEGAWA, K. Biomechanical analysis of a long-segment fusion in a lumbar spine—a finite element model study. **Journal of Biomechanical Engineering**, v. 140, n. 9, 24 maio 2018. Available in: <https://doi.org/10.1115/1.4039989>. Access in: 05 dez. 2023.



NATOUR, Jamil (org.) **Coluna vertebral: conhecimentos básicos**. São Paulo: Etecetera Editora, 2004.

NEGRINI, S. *et al.* Recommendations for research studies on treatment of idiopathic scoliosis: Consensus 2014 between SOSORT and SRS non-operative management committee. **Scoliosis**, v. 10, n. 1, 7 mar. 2015. Available in: <https://doi.org/10.1186/s13013-014-0025-4>. Access in: 03 abr. 2024.

NEWTON, P. O. *et al.* Anterior Spinal Growth Modulation in Skeletally Immature Patients with Idiopathic Scoliosis. **Journal of Bone and Joint Surgery**, v. 102, n. 9, p. 769–777, 19 fev. 2020. Available in: <http://dx.doi.org/10.2106/JBJS.19.01176>. Access in: 15 dez. 2023.

NEWTON, P. O. *et al.* Anterior spinal growth tethering for skeletally immature patients with scoliosis. **Journal of Bone and Joint Surgery**, v. 100, n. 19, p. 1691–1697, 3 out. 2018. Available in: <https://doi.org/10.2106/JBJS.18.00287>. Access in: 02 dez. 2023.

NEWTON, P. O. Spinal growth tethering: indications and limits. **Annals of Translational Medicine**, v. 8, n. 2, p. 27–27, 1 jan. 2020. Available in: <https://doi.org/10.21037/atm.2019.12.159>. Access in: 03 abr. 2024.

NICOLINI, Luis Fernando. **Effect of sagittal alignment fusion of the lumbosacral spine: an analysis with finite elements**. 2016. Dissertation. (Master's Degree in Mechanical Engineering). Federal University of Santa Catarina, Technological Center. Postgraduate Program in Mechanical Engineering, 2016.

NICOLINI, Luis Fernando *et al.* Motion preservation surgery for scoliosis with a vertebral body tethering system: a biomechanical study. **European Spine Journal**, v. 31, n. 4, p. 1013–1021, 30 out. 2021. Available in: <https://doi.org/10.1007/s00586-021-07035-4>. Access in: 15 jan. 2024.

NICOLINI, Luis Fernando *et al.* The effects of tether pretension within vertebral body tethering on the biomechanics of the spine: a Finite Element analysis. **Latin American Journal of Solids and Structures**, v. 19, n. 3, 1 jan. 2022a. Available in: <https://doi.org/10.1590/1679-78256932>. Access in: 09 abr. 2024.

NICOLINI, Luis Fernando *et al.* An experimental-numerical method for the calibration of finite element models of the lumbar spine. **Medical engineering & physics**, v. 107, p. 103854–103854, 1 set. 2022b. Available in: <https://doi.org/10.1016/j.medengphy.2022.103854>. Epub 2022 Jul 19. Access in: 04 abr. 2024.

NICOLINI, Luis Fernando. The effects of the vertebral body tethering system on the biomechanics of the thoracolumbar spine. 2022. Thesis. (Doctorate in Mechanical Engineering). Aachen University, Germany, 2022.

NICOLINI, Luis Fernando *et al.* Tether pre-tension within vertebral body tethering reduces motion of the spine and influences coupled motion: a finite element

analysis. **Computers in biology and medicine**, v. 169, p. 107851–107851, 1 fev. 2024. Available in: <https://doi.org/10.1016/j.compbimed.2023.107851>. Access in: 15 jan. 2024.

O'DONNELL, J. M. *et al.* Anterior vertebral body tethering for adolescent idiopathic scoliosis associated with less early post-operative pain and shorter recovery compared with fusion. **Spine Deformity**, v. 11, p. 919-925, 21 fev. 2023. Available in: <https://doi.org/10.1007/s43390-023-00661-6>. Access in: 24 jan. 2024.

OLIVEIRA, Rafael Carreira. **A numerical analysis of the effects of vertebral body tethering on spine motion**. 2022. Undergraduate Thesis. (Graduation in Mechanical Engineering). Federal University of Santa Catarina, Florianópolis, 2022.

OLIVEIRA, Rafael Carreira *et al.* Development of a finite element model of the thoracolumbar spine for the investigation of vertebral body tethering instrumentation. In: INTERNATIONAL CONGRESS OF MECHANICAL ENGINEERING, 27., 2023, Florianópolis. Proceedings [...] . Florianópolis: Abcm, 2023. p. 1-10.

OTTARDI, C. *et al.* Finite element analysis of the lumbar destabilization following pedicle subtraction osteotomy. **Medical engineering & physics**, v. 38, n. 5, p. 506–509, 1 maio 2016. Available in: <http://dx.doi.org/10.1016/j.medengphy.2016.02.002>. Access in: 28 jan. 2024.

PARENT, S.; SHEN, J. Anterior vertebral body growth-modulation tethering in idiopathic scoliosis: surgical technique. **Journal of the American Academy of Orthopaedic Surgeons**, v. 28, n. 17, p. 693–699, 1 jul. 2020. Available in: <https://doi.org/10.5435/JAAOS-D-19-00849>. Access in: 08 mar. 2024.

PEHLIVANOGLU, T. *et al.* Thoracoscopic vertebral body tethering for adolescent idiopathic scoliosis. **Journal of Pediatric Orthopaedics**, v. Publish Ahead of Print, 15 maio 2020. Available in: <https://doi.org/10.1097/BPO.0000000000001590>. Access in: 29 abr. 2024.

PELLICER-VALERO, O. J. *et al.* Real-time biomechanical modeling of the liver using Machine Learning models trained on finite element method simulations. **Expert Systems With Applications**, v. 143, p. 113083–113083, 1 abr. 2020. Available in: <https://doi.org/10.1016/j.eswa.2019.113083>. Access in: 09 abr. 2024.

PHELLAN, R. *et al.* Real-time biomechanics using the finite element method and machine learning: review and perspective. **Medical Physics**, 22 nov. 2020. Available in: <https://doi.org/10.1002/mp.14602>. Access in: 10 fev. 2024.

PHILLIPS, F. M. *et al.* Minimally invasive spine surgery: surgical techniques and disease management. 2 ed. [s.l.] **Springer Nature**, 2019. Available in: <https://doi.org/10.1007/978-3-030-19007-1>. Access in: 02 fev. 2024.

RAITIO, A.; SYVÄNEN, J.; HELENIUS, I. Vertebral body tethering: indications, surgical technique, and a systematic review of published results. **Journal of Clinical Medicine**, v. 11, n. 9, p. 2576, 4 maio 2022. Available in: <https://doi.org/10.3390/jcm11092576>. Access in: 25 fev. 2024.

REDDY, J. N. **An introduction to continuum mechanics**. 2 ed. New York: Cambridge University Press, 2013.

REVILLA-LEÓN, Martha *et al.* Artificial intelligence applications in implant dentistry: a systematic review. **The Journal of Prosthetic Dentistry**, v. 129, n. 2, 2023. Available in: <https://doi.org/10.1016/j.prosdent.2021.05.008>. Access in: 10 fev. 2024.

RITZEL, Holger. The thickness of human vertebral cortical bone and its changes in aging and osteoporosis: a histomorphometric analysis of the complete spinal column from thirty-seven autopsy specimens. **Journal of Bone and Mineral Research**, v. 12, n. 1, p. 89–95, 1 jan. 1997. Available in: <https://doi.org/10.1359/jbmr.1997.12.1.89>. Access in: 02 abr. 2024.

RITZMAN, T. F. *et al.* Comparison of compensatory curve spontaneous derotation after selective thoracic or lumbar fusions in adolescent idiopathic scoliosis. **Spine (Philadelphia, Pa. 1976)**, v. 33, n. 24, p. 2643–2647, 1 nov. 2008. Available in: <https://doi.org/10.1097/BRS.0b013e3181891806>. Access in: 18 jan. 2024.

ROACH, James W. Adolescent idiopathic scoliosis. **Disorders of the Pediatric and Adolescent Spine**, v. 30, n. 3, 1999.

ROHLMANN, A. *et al.* Determination of trunk muscle forces for flexion and extension by using a validated finite element model of the lumbar spine and measured in vivo data. **Journal of Biomechanics**, v. 39, n. 6, p. 981–989, jan. 2006. Available in: <https://doi.org/10.1016/j.jbiomech.2005.02.019>. Access in: 05 fev. 2024.

ROSER, M. J. *et al.* Vertebral body tethering for idiopathic scoliosis: a systematic review and meta-analysis. **Spine Deformity**, v. 11, n. 6, p. 1297–1307, 11 jul. 2023. Available in: <https://doi.org/10.1007/s43390-023-00723-9>. Access in: 25 mar. 2024.

ROY, S. *et al.* Design of patient specific dental implant using FE analysis and computational intelligence techniques. **Applied Soft Computing**, v. 65, p. 272–279, abr. 2018. Available in: <https://doi.org/10.1016/j.asoc.2018.01.025>. Access in: 28 mar. 2024.

RUSHTON, P. R. P. *et al.* Anterior vertebral body tethering for treatment of idiopathic scoliosis in the skeletally immature. **Spine**, v. 46, n. 21, p. 1461–1467, 4 jun. 2021. Available in: <https://doi.org/10.1097/BRS.0000000000004061>. Access in: 28 mar. 2024.

SAMDANI, A. F. *et al.* anterior vertebral body tethering for idiopathic scoliosis. **Spine**, v. 39, n. 20, p. 1688–1693, set. 2014a. Available in: <https://doi.org/10.1097/BRS.0000000000000472>. Access in: 04 mar. 2024.

SAMDANI, A. F. *et al.* Anterior vertebral body tethering for immature adolescent idiopathic scoliosis: one-year results on the first 32 patients. **European Spine Journal**, v. 24, n. 7, p. 1533–1539, 16 dez. 2014b. Available in: <https://doi.org/10.1007/s00586-014-3706-z>. Access in: 16 dez. 2023.

SANDERS, A. E. *et al.* Clinically significant psychological and emotional distress in 32% of adolescent idiopathic scoliosis patients. **Spine Deformity**, v. 6, n. 4, p. 435–440, jul. 2018. Available in: <https://doi.org/10.1016/j.jspd.2017.12.014>. Access in: 05 mar. 2024.

SCHLAGER, B. *et al.* Uncertainty analysis of material properties and morphology parameters in numerical models regarding the motion of lumbar vertebral segments. **Computer methods in biomechanics and biomedical engineering**, v. 21, n. 12, p. 673–683, 10 set. 2018. Available in: <https://doi.org/10.1080/10255842.2018.1508571>. Access in: 10 fev. 2024.

SCHLÖSSER, T. P. C. *et al.* Anterior overgrowth in primary curves, compensatory curves and junctional segments in adolescent idiopathic scoliosis. **PLOS ONE**, v. 11, n. 7, p. e0160267, 28 jul. 2016. Available in: <https://doi.org/10.1371/journal.pone.0160267>. Access in: 10 jan. 2024.

SCHMIDT, H. *et al.* Application of a calibration method provides more realistic results for a finite element model of a lumbar spinal segment. **Clinical Biomechanics**, v. 22, n. 4, p. 377–384, maio 2007. Available in: <https://doi.org/10.1016/j.clinbiomech.2006.11.008>. Access in: 15 fev. 2024.

SCHMIDT, H. *et al.* Application of a new calibration method for a three-dimensional finite element model of a human lumbar annulus fibrosus. **Clinical Biomechanics**, v. 21, n. 4, p. 337–344, 1 maio 2006. Available in: <https://doi.org/10.1016/j.clinbiomech.2005.12.001>. Access in: 10 jan. 2024.

SCHMIDT, H.; HEUER, F.; WILKE, H.-J. Interaction between finite helical axes and facet joint forces under combined loading. **Spine**, v. 33, n. 25, p. 2741–2748, dez. 2008. Available in: <https://doi.org/10.1097/BRS.0b013e31817c4319>. Access in: 10 jan. 2024.

SHAKIL, H.; IQBAL, Z. A.; AL-GHADIR, A. H. Scoliosis: review of types of curves, etiological theories and conservative treatment. **Journal of Back and Musculoskeletal Rehabilitation**, v. 27, n. 2, p. 111–115, 1 abr. 2014. Available in: <https://doi.org/10.3233/BMR-130438>. Access in: 11 jan. 2024.

SHIN, J.-H. *et al.* Investigation of coupled bending of the lumbar spine during dynamic axial rotation of the body. **European Spine Journal**, v. 22, n. 12, p. 2671–2677, 28 abr. 2013. Available in: <https://doi.org/10.1007/s00586-013-2777-6>. Access in: 26 jan. 2024.

SHIN, M. *et al.* Complications, reoperations, and mid-term outcomes following anterior vertebral body tethering versus posterior spinal fusion. **JBJS Open Access**, v. 6, n. 2, p. e21.00002, 23 jun. 2021. Available in: <http://dx.doi.org/10.2106/JBJS.OA.21.00002>. Access in: 19 jan. 2024.

STOKES, I. A. *et al.* Mechanical modulation of vertebral body growth. Implications for scoliosis progression. **Spine**, v. 21, n. 10, p. 1162–7, 1996. Available in: <https://doi.org/10.1097/00007632-199605150-00007>. Access in: 27 abr. 2024.

STOKES, I. A. F. Analysis and simulation of progressive adolescent scoliosis by biomechanical growth modulation. **European Spine Journal**, v. 16, n. 10, p. 1621–1628, 26 jul. 2007. Available in: <http://dx.doi.org/10.1007/s00586-007-0442-7>. Access in: 13 jan. 2024.

STOKES, IAN A. F. *et al.* Endochondral growth in growth plates of three species at two anatomical locations modulated by mechanical compression and tension. **Journal of Orthopaedic Research**, v. 24, n. 6, p. 1327–1334, 1 jan. 2006. Available in: <http://dx.doi.org/10.1002/jor.20189>. Access in: 15 jan. 2024.

TABER, Larry A. **Nonlinear theory of elasticity**: applications in biomechanics. Singapore: World Scientific Publishing, 2004.

THÉROUX, Jean *et al.* Prevalence and management of back pain in adolescent idiopathic scoliosis patients: A retrospective study. **Pain Res Manag**, v. 20, n. 3 May/June 2015.

TORTORA, Gerard J.; DERRICKSON, Bryan. **Principles of anatomy and physiology**. 15 ed. England: Wiley, 2017.

TROBISCH, P. D.; BARONCINI, A. Preliminary outcomes after vertebral body tethering (VBT) for lumbar curves and subanalysis of a 1- versus 2-tether construct. **European Spine Journal**, v. 30, n. 12, p. 3570–3576, 30 set. 2021. Available in: <http://dx.doi.org/10.1007/s00586-021-07009-6>. Access in: 03 abr. 2024.

TROBISCH, P. D.; KOBBE, P.; BARONCINI, A. dynamic scoliosis correction as alternative treatment for patients with adolescent idiopathic scoliosis: a non-fusion surgical technique. **Zeitschrift für Orthopädie und Unfallchirurgie**, 18 set. 2019. Available in: <https://doi.org/10.1055/a-0983-1265>. Access in: 25 jan. 2024.

TROBISCH, Per *et al.* An investigation of range of motion preservation in fusionless anterior double screw and cord constructs for scoliosis correction. **European spine journal**, v. 32, n. 4, p. 1173–1186, 5 mar. 2023. Available in: <https://doi.org/10.1007/s00586-023-07608-5>. Access in: 25 jan. 2024.

TROBISCH, Per *et al.* Difference between radiographically suspected and intraoperatively confirmed tether breakages after vertebral body tethering for idiopathic scoliosis. **European spine journal**, v. 31, n. 4, p. 1045–1050, 8 jan. 2022. Available in: <https://doi.org/10.1007/s00586-021-07107-5>. Access in: 10 jan. 2024.

VATKAR, Arvind *et al.* Vertebral body tethering in adolescent idiopathic scoliosis with more than 2 years of follow-up- systematic review and meta-analysis. **European Spine Journal**, v. 32, n. 9, p. 3047–3057, 12 jun. 2023. Available in: <https://doi.org/10.1007/s00586-023-07724-2>. Access in: 08 fev. 2024.

VILLEMURE, I.; STOKES, I. A. F. Growth plate mechanics and mechanobiology. A survey of present understanding. **Journal of Biomechanics**, v. 42, n. 12, p. 1793–1803, ago. 2009. Available in: <https://doi.org/10.1016/j.jbiomech.2009.05.021>. Access in: 29 fev. 2024.

VRTOVEC, T.; PERNUŠ, F.; LIKAR, B. A review of methods for quantitative evaluation of spinal curvature. **European Spine Journal**, v. 18, n. 5, p. 593–607, 27 fev. 2009. Available in: <https://doi.org/10.1007/s00586-009-0913-0>. Access in: 10 fev. 2024.

WEINSTEIN, Stuart L. (ed.). **The pediatric spine: principles and practice**. 2 ed. Philadelphia: Lippincott Williams & Wilkins, 2001.

WEINSTEIN, S. L. *et al.* Adolescent idiopathic scoliosis. **The Lancet**, v. 371, n. 9623, p. 1527–1537, maio 2008. Available in: [https://doi.org/10.1016/S0140-6736\(08\)60658-3](https://doi.org/10.1016/S0140-6736(08)60658-3). Access in: 03 abr. 2024.

WEINSTEIN, Stuart L.; FLYNN, John M.; CRAWFORD, HAEMISH A (ed.). Lovell and winter's: pediatric orthopaedics. 8 ed. v. 2. Wolters Kluwer, 2021.

WEISS, H.-R. *et al.* Long-term effects of untreated adolescent idiopathic scoliosis: a review of the literature. **Asian Spine Journal**, v. 10, n. 6, p. 1163, 2016. Available in: <https://doi.org/10.4184/asj.2016.10.6.1163>. Access in: 04 abr. 2024.

WIDMER, J. *et al.* Kinematics of the spine under healthy and degenerative conditions: a systematic review. **Annals of Biomedical Engineering**, v. 47, n. 7, p. 1491–1522, 1 abr. 2019. Available in: <https://doi.org/10.1007/s10439-019-02252-x>. Access in: 15 mar. 2024.

WILKE, H.-J. *et al.* In vitro analysis of the segmental flexibility of the thoracic spine. **PLOS ONE**, v. 12, n. 5, p. e0177823, 16 maio 2017. Available in: <https://doi.org/10.1371/journal.pone.0177823>. eCollection 2017. Access in: 05 fev. 2024.

WILKE, H.-J. *et al.* In vitro analysis of thoracic spinal motion segment flexibility during stepwise reduction of all functional structures. **European Spine Journal**, v. 29, n. 1, p. 179–185, 29 out. 2019. Available in: <https://doi.org/10.1007/s00586-019-06196-7>. Epub 2019 Oct 29. Access in: 09 jan. 2024.

WILKE, H.-J. *et al.* Is it possible to simulate physiologic loading conditions by applying pure moments? **Spine**, v. 26, n. 6, p. 636–642, 1 mar. 2001. Available in: <https://doi.org/10.1097/00007632-200103150-00014>. Access in: 25 fev. 2024.

WONG, H.-K. *et al.* Non-fusion surgical correction of thoracic idiopathic scoliosis using a novel, braided vertebral body tethering device. **JBJS Open Access**, v. 4, n. 4, p. e0026, 2019. Available in: <http://dx.doi.org/10.2106/JBJS.OA.19.00026>. Access in: 10 fev. 2024.

YING, J. *et al.* Biomechanical insights into ankle instability: a finite element analysis of posterior malleolus fractures. **Journal of orthopaedic surgery and research**, v. 18, n. 1, 12 dez. 2023. Available in: <https://doi.org/10.1186/s13018-023-04432-x>. Access in: 24 mar. 2024.

YUCEKUL, A. *et al.* Does vertebral body tethering cause disc and facet joint degeneration? A preliminary MRI study with minimum two years follow-up. **The Spine Journal**, v. 21, n. 11, p. 1793–1801, nov. 2021. Available in: <https://doi.org/10.1016/j.spinee.2021.05.020>. Access in: 25 abr. 2024.

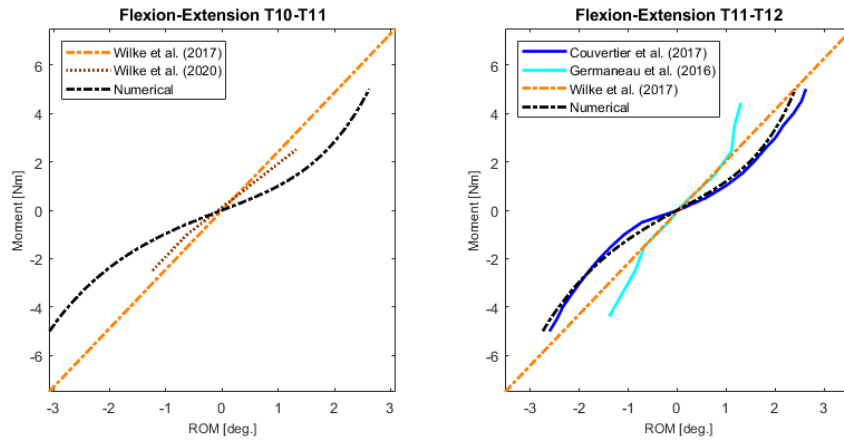
ZHONG, Z. C.; CHEN, S. H.; HUNG, C.-H. Load- and displacement-controlled finite element analyses on fusion and non-fusion spinal implants. **Proceedings of the Institution of Mechanical Engineers, Part H: Journal of Engineering in Medicine**, v. 223, n. 2, p. 143–157, 18 dez. 2008. Available in: <https://doi.org/10.1243/09544119JEIM476>. Access in: 25 abr. 2024.

ZHONG, Zheng-Cheng *et al.* The influence of different magnitudes and methods of applying preload on fusion and disc replacement constructs in the lumbar spine: a finite element analysis. **Computer methods in biomechanics and biomedical engineering**, v. 16, n. 9, p. 943–953, 1 set. 2013. Available in: <https://doi.org/10.1080/10255842.2011.645226>. Access in: 28 abr. 2024.

ZHU, F. *et al.* Minimum 3-year experience with vertebral body tethering for treating scoliosis: A systematic review and single-arm meta-analysis. **Journal of orthopaedic surgery**, v. 30, n. 3, p. 102255362211377-102255362211377, 1 set. 2022. Available in: <https://doi.org/10.1177/10225536221137753>. Access in: 28 abr. 2024.

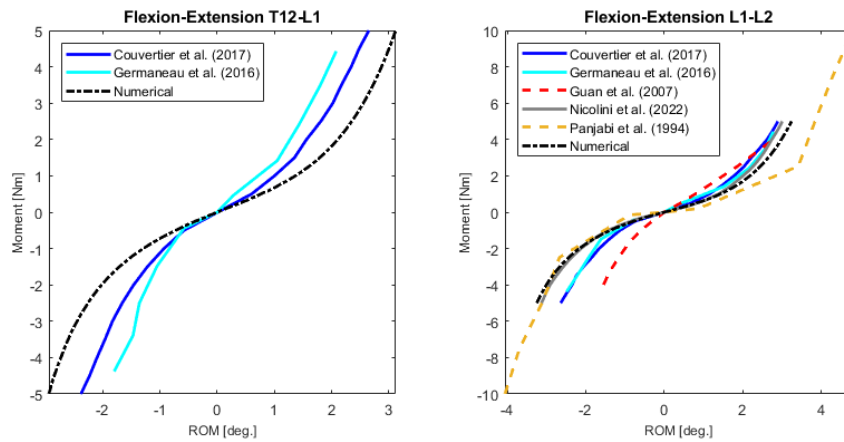
**APPENDIX A – Graphs pertaining to the validation of the thoracolumbar spine model**

Figure 41 – Comparison of the Moment-ROM curve of the T10-T11 and T11-T12 segments of the model with literature data in flexion-extension.



Source: Adapted from Oliveira et al. (2023).

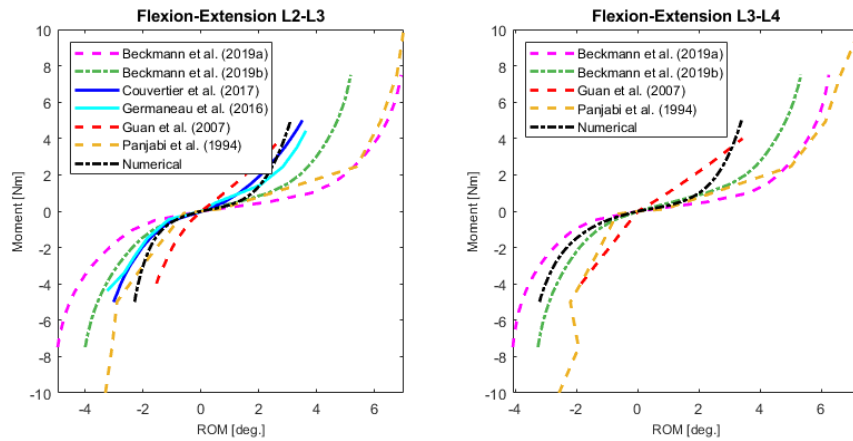
Figure 42 – Comparison of the Moment-ROM curve of the T12-L1 and L1-L2 segments of the model with literature data in flexion-extension.



Source: Adapted from Oliveira et al. (2023).

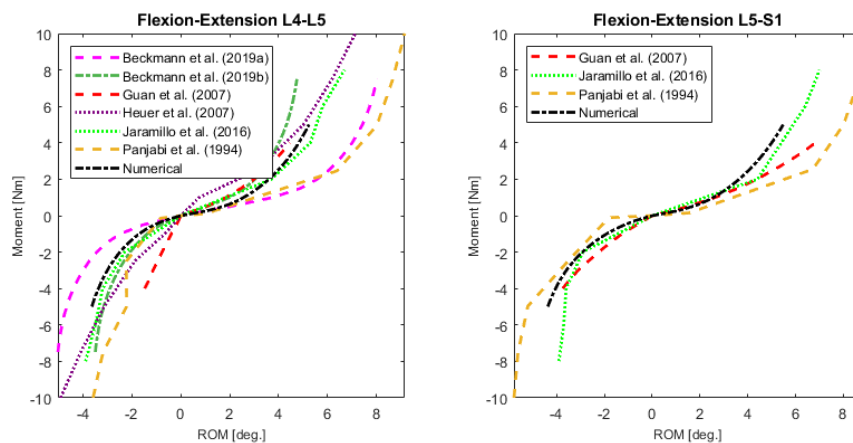


Figure 43 – Comparison of the Moment-ROM curve of the L2-L3 and L3-L4 segments of the model with literature data in flexion-extension.



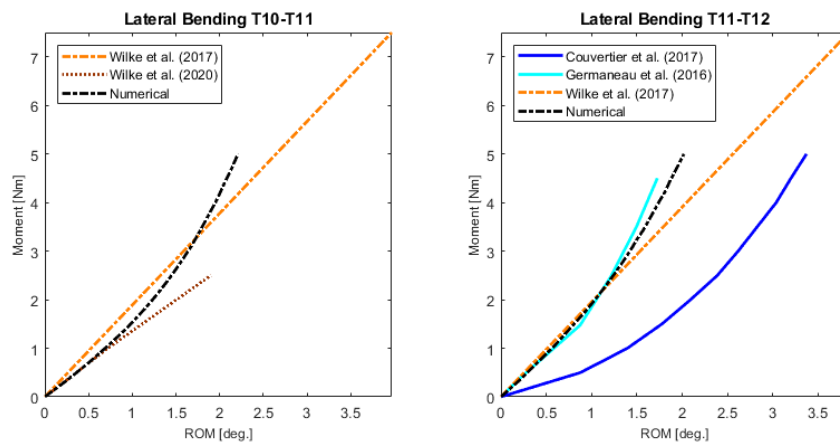
Source: Adapted from Oliveira et al. (2023).

Figure 44 – Comparison of the Moment-ROM curve of the L4-L5 and L5-S1 segments of the model with literature data in flexion-extension.



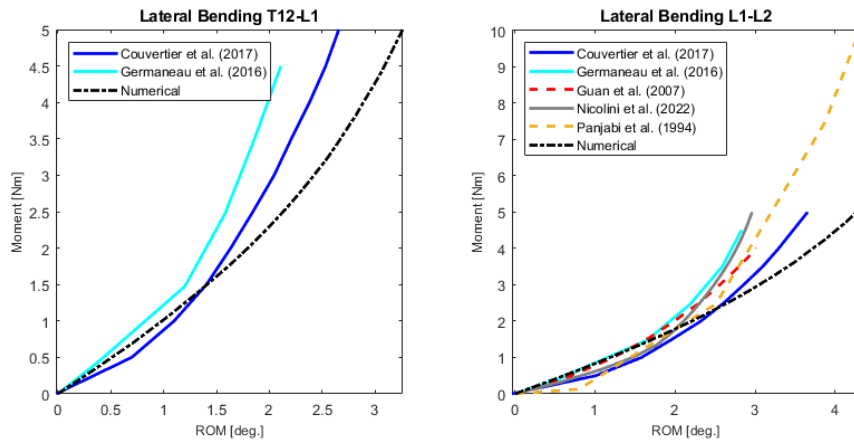
Source: Adapted from Oliveira et al. (2023).

Figure 45 – Comparison of the Moment-ROM curve of the T10-T11 and T11-T12 segments of the model with literature data in lateral bending.



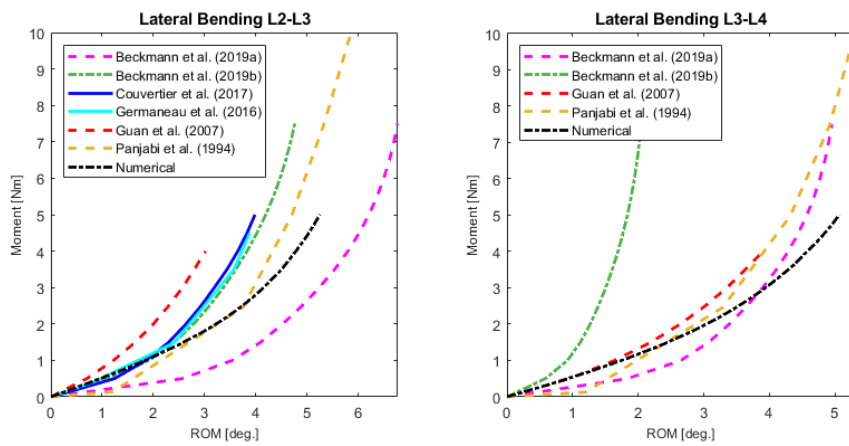
Source: Adapted from Oliveira et al. (2023).

Figure 46 – Comparison of the Moment-ROM curve of the T12-L1 and L1-L2 segments of the model with literature data in lateral bending.



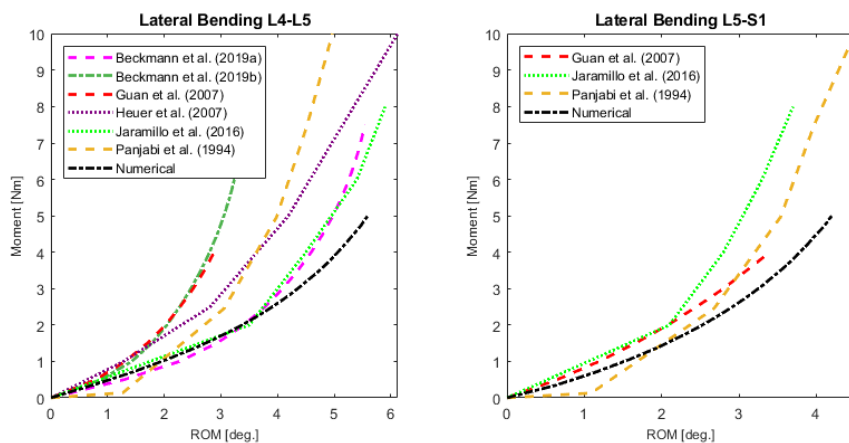
Source: Adapted from Oliveira et al. (2023).

Figure 47 – Comparison of the Moment-ROM curve of the L2-L3 and L3-L4 segments of the model with literature data in lateral bending.



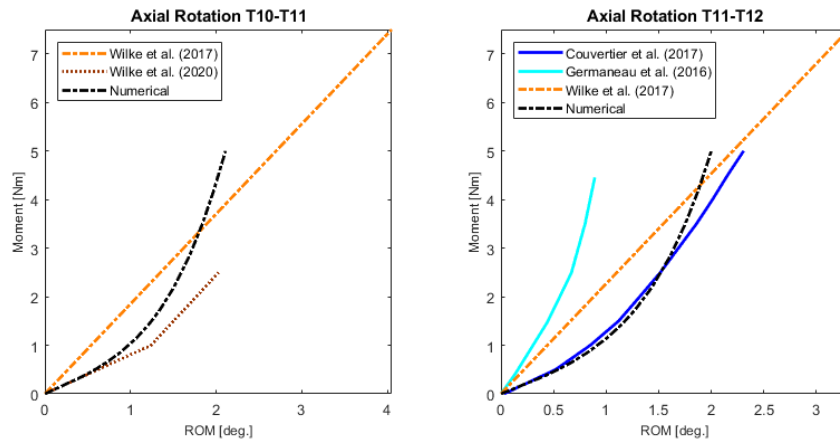
Source: Adapted from Oliveira et al. (2023).

Figure 48 – Comparison of the Moment-ROM curve of the L4-L5 and L5-S1 segments of the model with literature data in lateral bending.



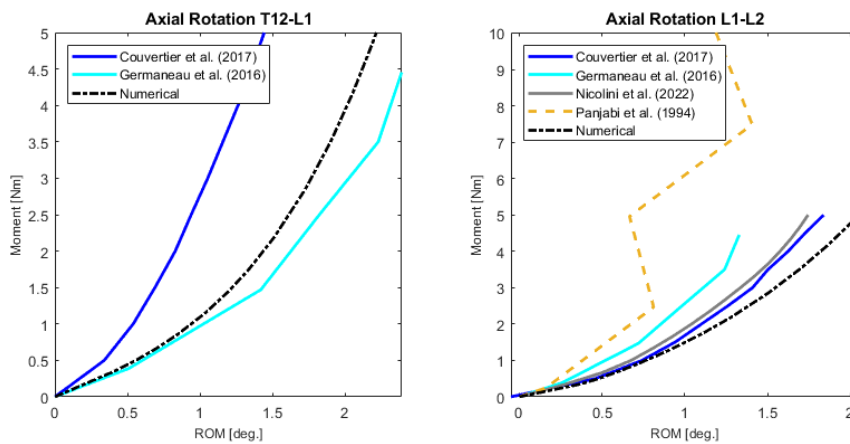
Source: Adapted from Oliveira et al. (2023).

Figure 49 – Comparison of the Moment-ROM curve of the T10-T11 and T11-T12 segments of the model with literature data in axial rotation.



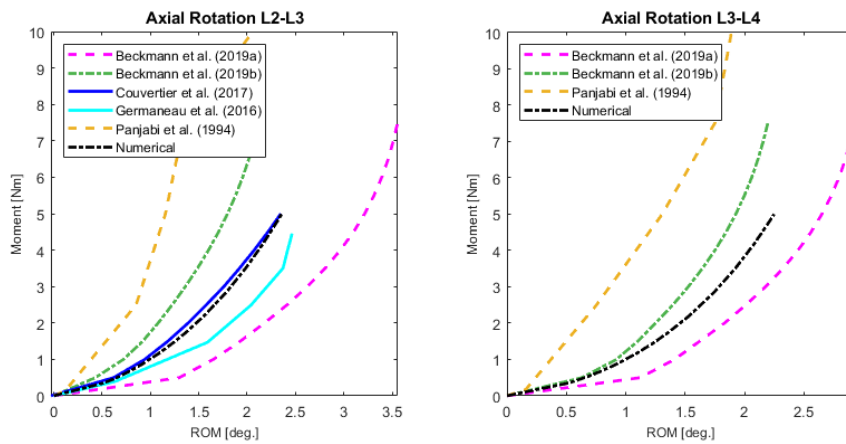
Source: Adapted from Oliveira et al. (2023).

Figure 50 – Comparison of the Moment-ROM curve of the T12-L1 and L1-L2 segments of the model with literature data in axial rotation.



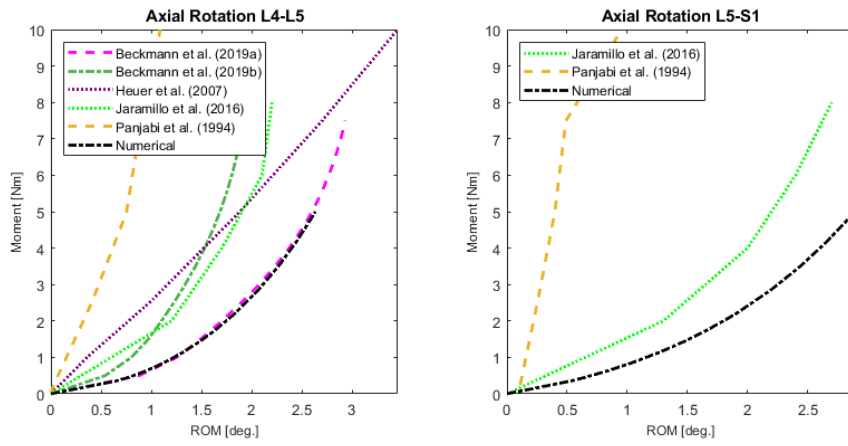
Source: Adapted from Oliveira et al. (2023).

Figure 51 – Comparison of the Moment-ROM curve of the L2-L3 and L3-L4 segments of the model with literature data in axial rotation.



Source: Adapted from Oliveira et al. (2023).

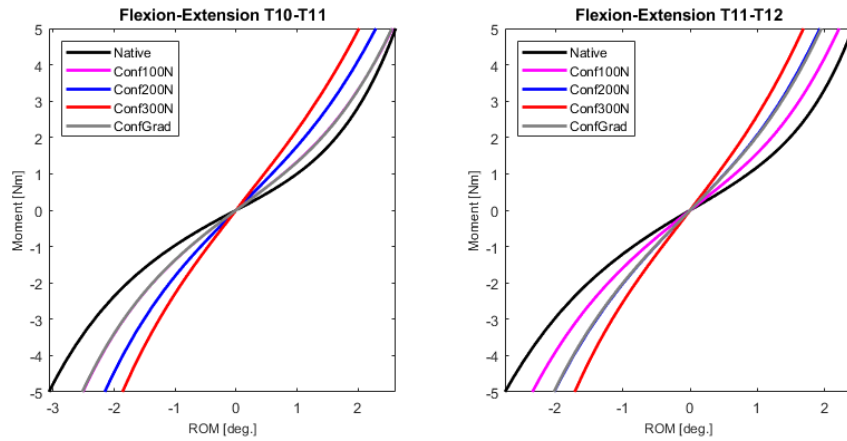
Figure 52 – Comparison of the Moment-ROM curve of the L4-L5 and L5-S1 segments of the model with literature data in axial rotation.



Source: Adapted from Oliveira et al. (2023).

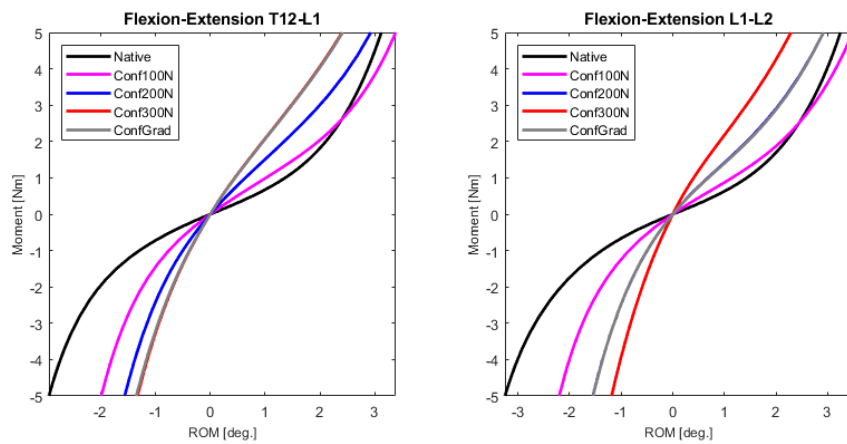
## APPENDIX B – Moment-ROM graphs of the instrumented spine under different pre-tension configurations

Figure 53 – Moment-ROM curves of the T10-T11 and T11-T12 segments of the spine in different pre-tension configurations under pure flexion-extension moment loading.



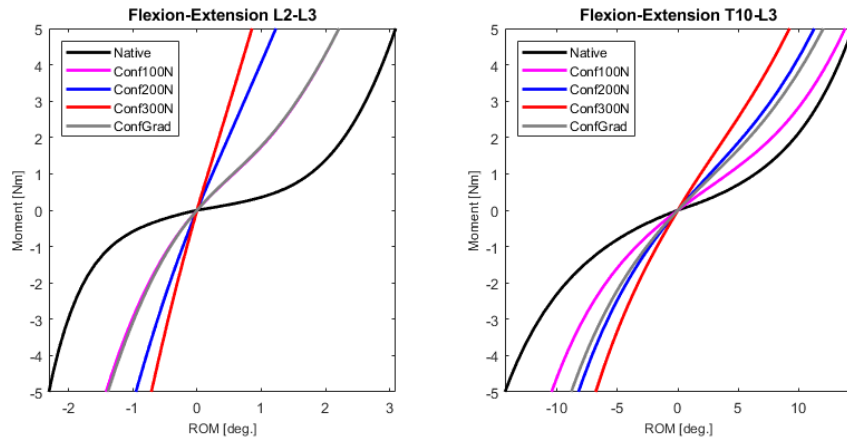
Source: Author.

Figure 54 – Moment-ROM curves of the T12-L1 and L1-L2 segments of the spine in different pre-tension configurations under pure flexion-extension moment loading.



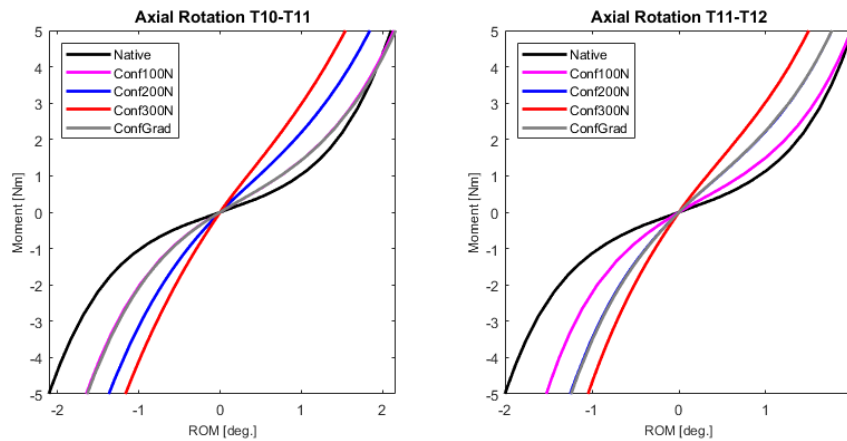
Source: Author.

Figure 55 – Moment-ROM curves of the L2-L3 segment of the spine and the whole instrumented spine (T10-L3) in different pre-tension configurations under pure flexion-extension moment loading.



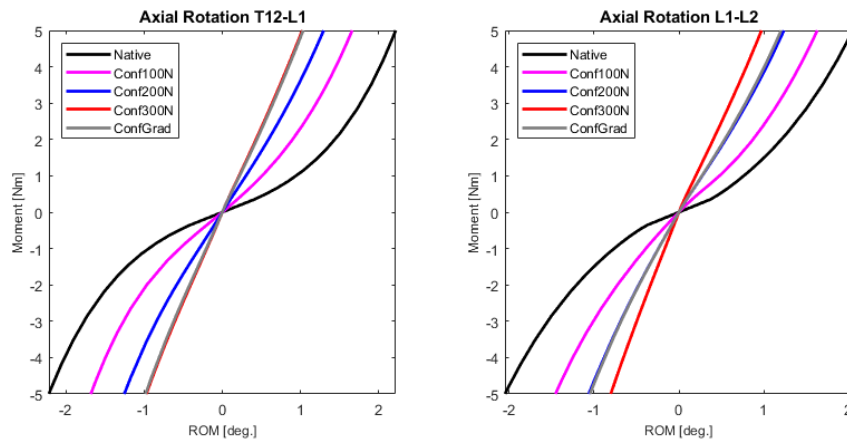
Source: Author.

Figure 56 – Moment-ROM curves of the T10-T11 and T11-T12 segments of the spine in different pre-tension configurations under pure axial rotation moment loading.



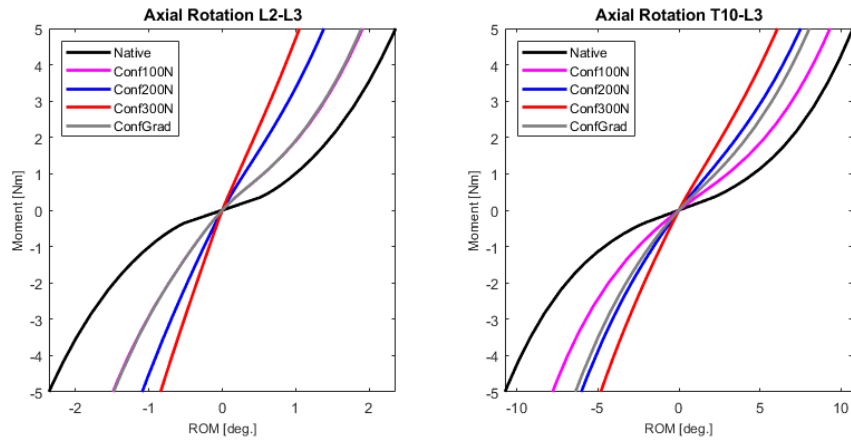
Source: Author.

Figure 57 – Moment-ROM curves of the T12-L1 and L1-L2 segments of the spine in different pre-tension configurations under pure axial rotation moment loading.



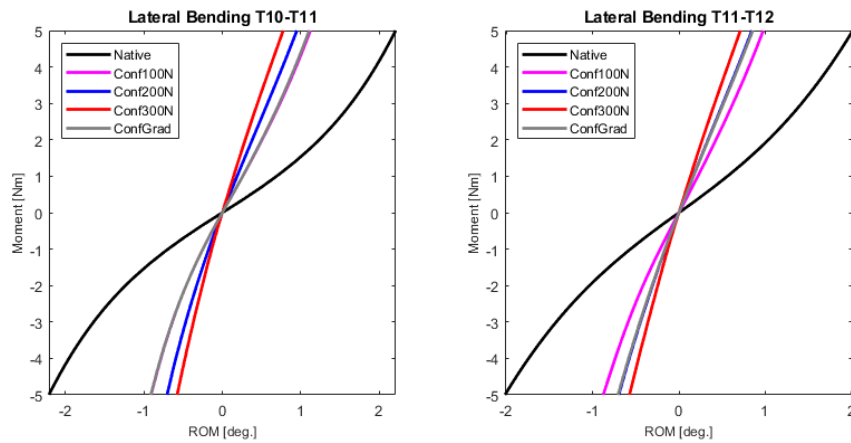
Source: Author.

Figure 58 – Moment-ROM curves of the L2-L3 segment of the spine and the whole instrumented spine (T10-L3) in different pre-tension configurations under pure axial rotation moment loading.



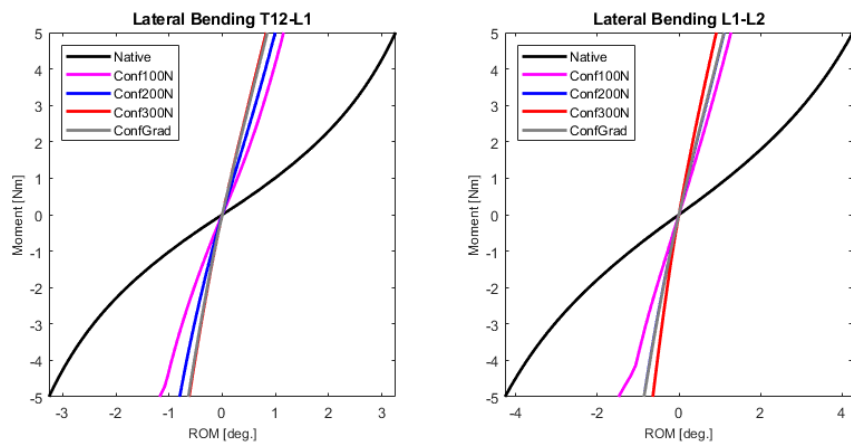
Source: Author.

Figure 59 – Moment-ROM curves of the T10-T11 and T11-T12 segments of the spine in different pre-tension configurations under pure lateral bending moment loading.



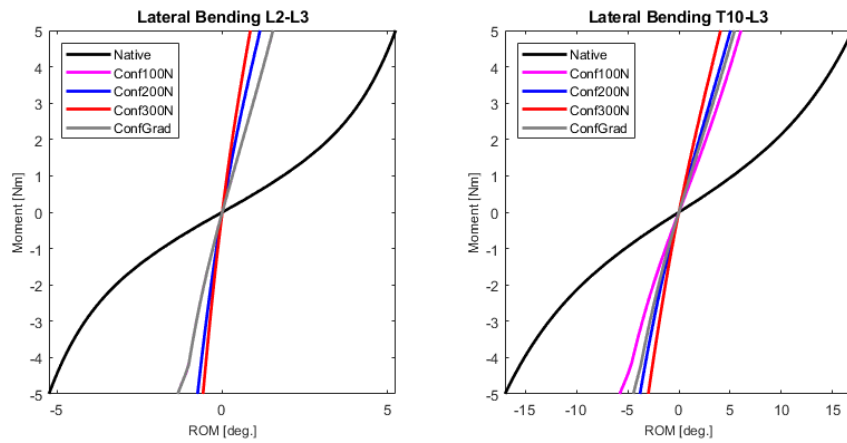
Source: Author.

Figure 60 – Moment-ROM curves of the T12-L1 and L1-L2 segments of the spine in different pre-tension configurations under pure lateral bending moment loading.



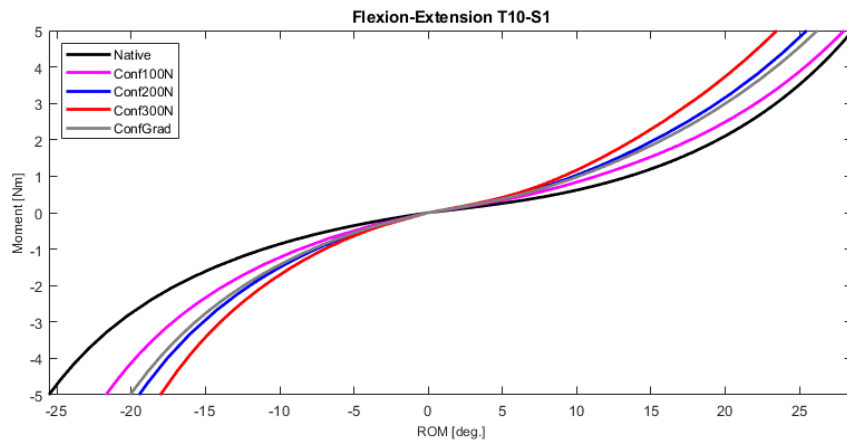
Source: Author.

Figure 61 – Moment-ROM curves of the L2-L3 segment of the spine and the whole instrumented spine (T10-L3) in different pre-tension configurations under pure lateral bending moment loading.



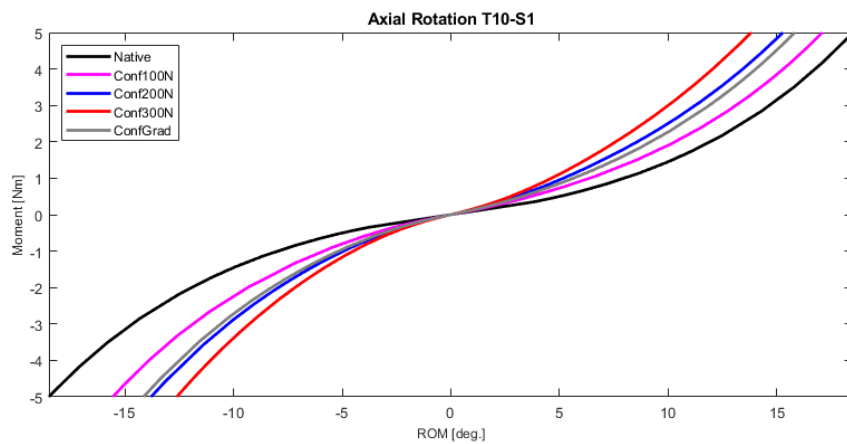
Source: Author.

Figure 62 – Moment-ROM curves of the whole thoracolumbar spine model (T10-S1) in different pre-tension configurations under pure flexion-extension moment loading.



Source: Author.

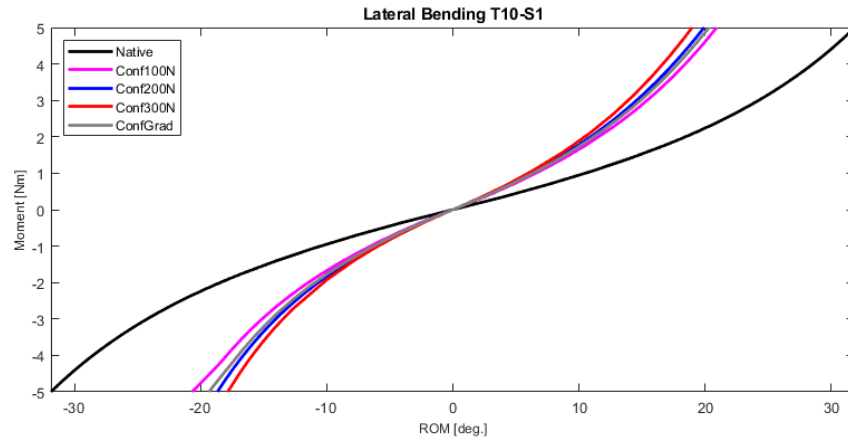
Figure 63 – Moment-ROM curves of the whole thoracolumbar spine model (T10-S1) in different pre-tension configurations under pure axial rotation moment loading.



Source: Author.



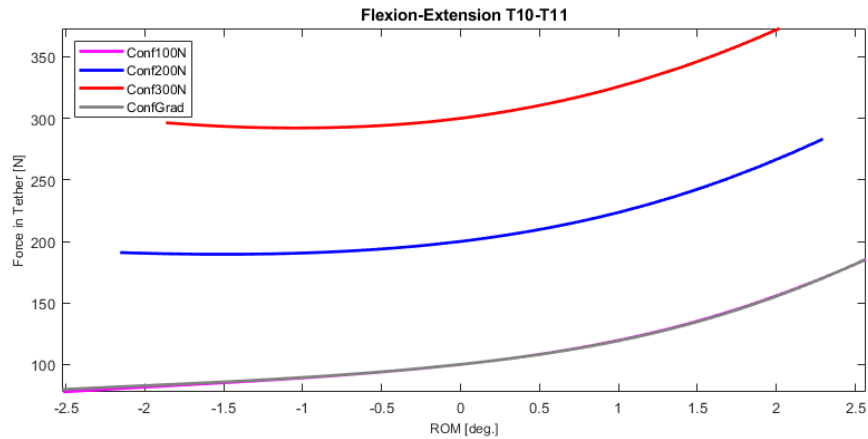
Figure 64 – Moment-ROM curves of the whole thoracolumbar spine model (T10-S1) in different pre-tension configurations under lateral bending moment loading.



Source: Author.

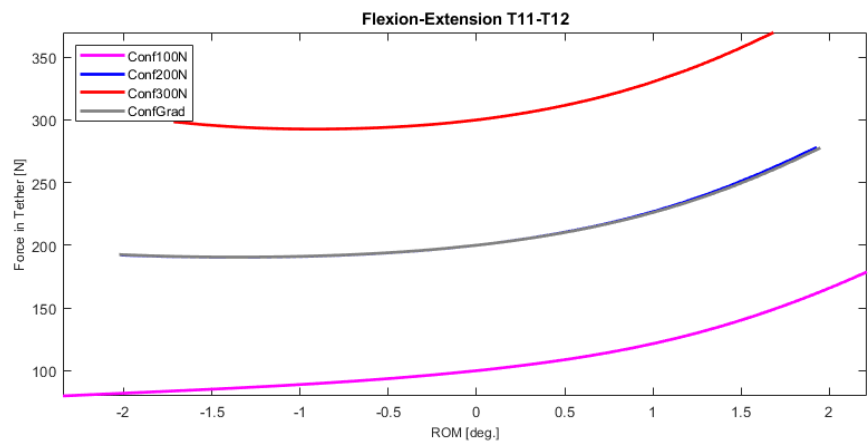
## APPENDIX C – Tether Force-ROM graphs of each segment of the instrumented spine under different pre-tension configurations

Figure 65 – Tether Force-ROM curves of the T10-T11 segment of the spine in different pre-tension configurations under pure flexion-extension moment loading.



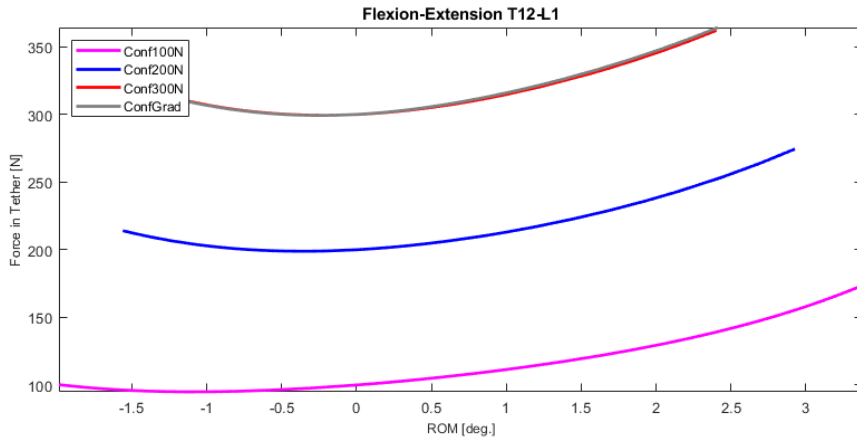
Source: Author.

Figure 66 – Tether Force-ROM curves of the T11-T12 segment of the spine in different pre-tension configurations under pure flexion-extension moment loading.



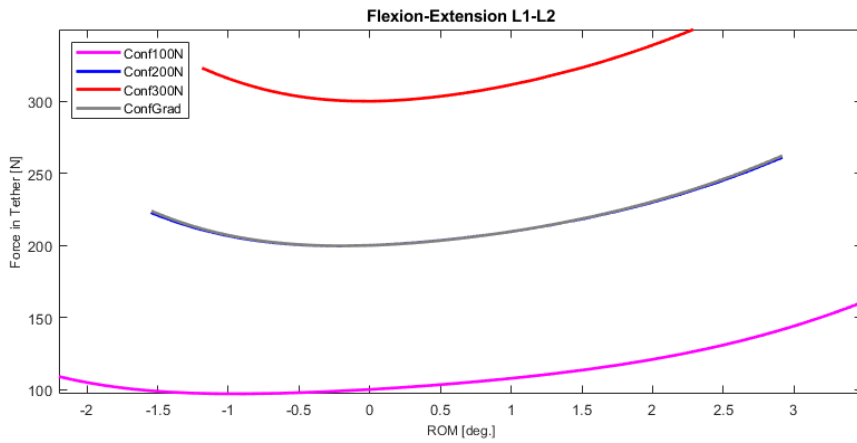
Source: Author.

Figure 67 – Tether Force-ROM curves of the T12-L1 segment of the spine in different pre-tension configurations under pure flexion-extension moment loading.



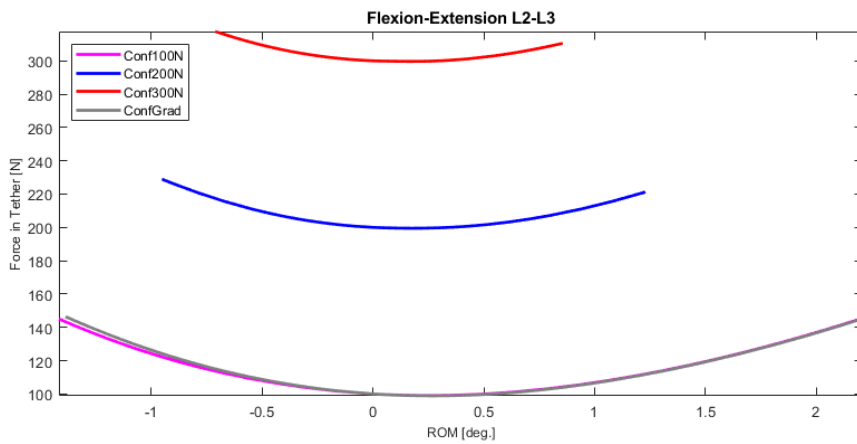
Source: Author.

Figure 68 – Tether Force-ROM curves of the L1-L2 segment of the spine in different pre-tension configurations under pure flexion-extension moment loading.



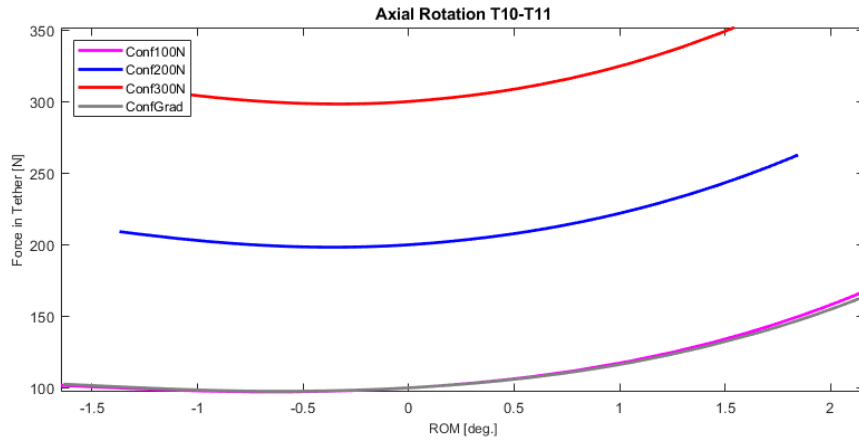
Source: Author.

Figure 69 – Tether Force-ROM curves of the L2-L3 segment of the spine in different pre-tension configurations under pure flexion-extension moment loading.



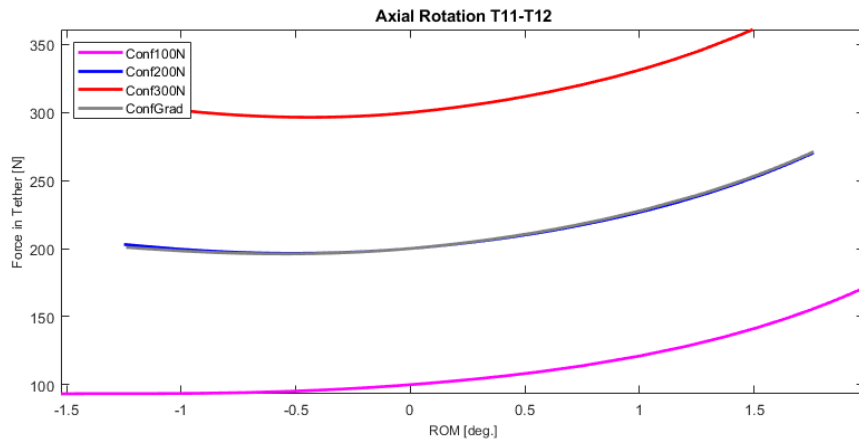
Source: Author.

Figure 70 – Tether Force-ROM curves of the T10-T11 segment of the spine in different pre-tension configurations under pure axial rotation moment loading.



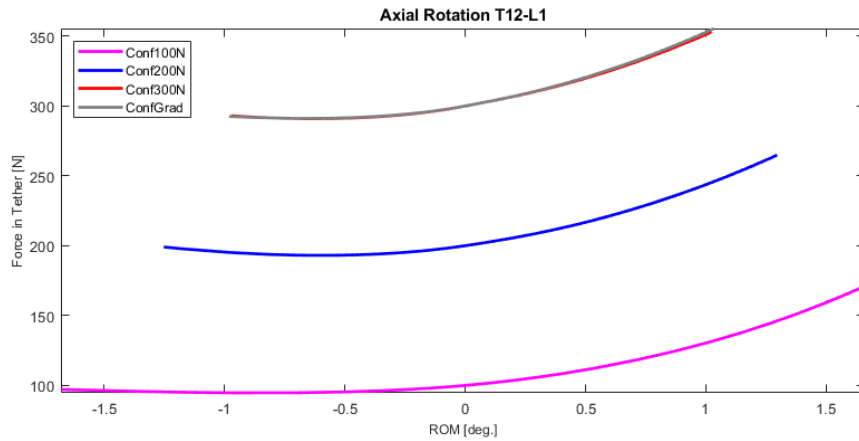
Source: Author.

Figure 71 – Tether Force-ROM curves of the T11-T12 segment of the spine in different pre-tension configurations under pure axial rotation moment loading.



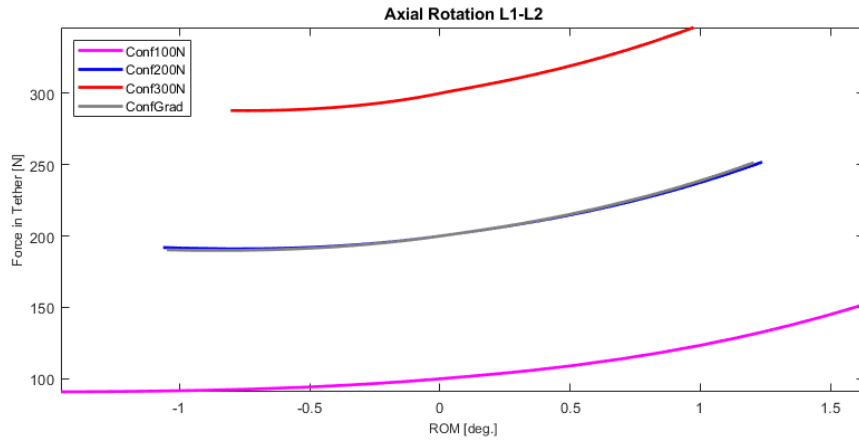
Source: Author.

Figure 72 – Tether Force-ROM curves of the T12-L1 segment of the spine in different pre-tension configurations under pure axial rotation moment loading.



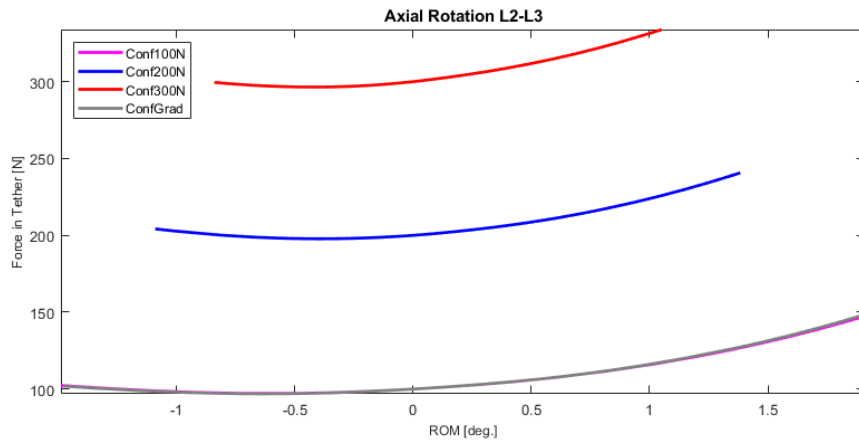
Source: Author.

Figure 73 – Tether Force-ROM curves of the L1-L2 segment of the spine in different pre-tension configurations under pure axial rotation moment loading.



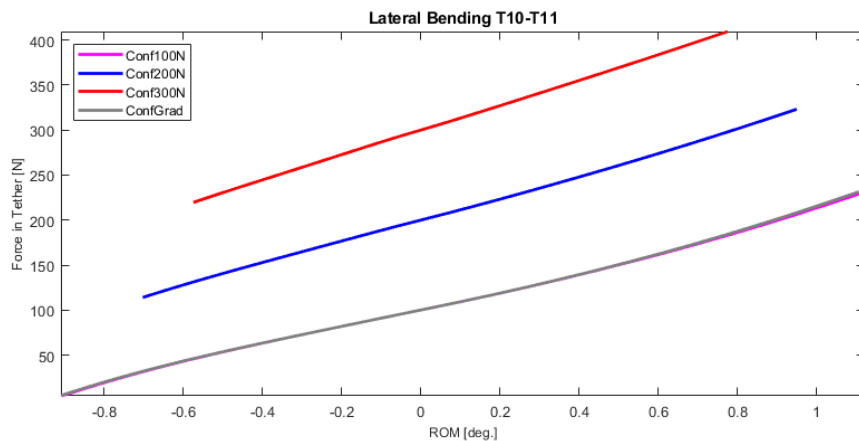
Source: Author.

Figure 74 – Tether Force-ROM curves of the L2-L3 segment of the spine in different pre-tension configurations under pure axial rotation moment loading.



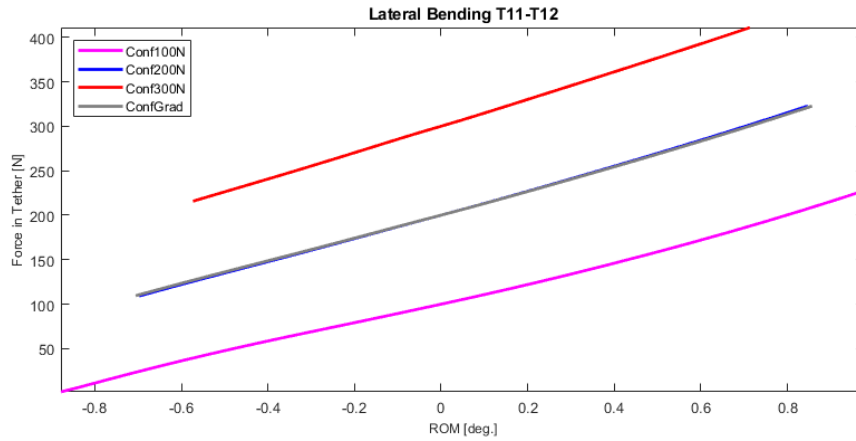
Source: Author.

Figure 75 – Tether Force-ROM curves of the T10-T11 segment of the spine in different pre-tension configurations under pure lateral bending moment loading.



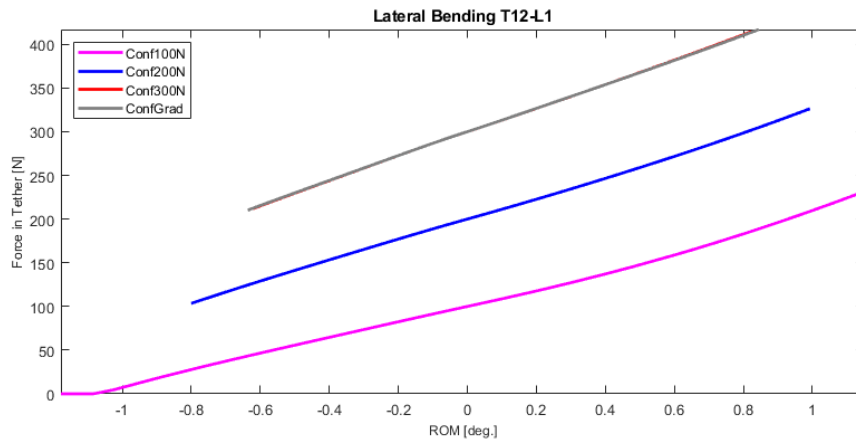
Source: Author.

Figure 76 – Tether Force-ROM curves of the T11-T12 segment of the spine in different pre-tension configurations under pure lateral bending moment loading.



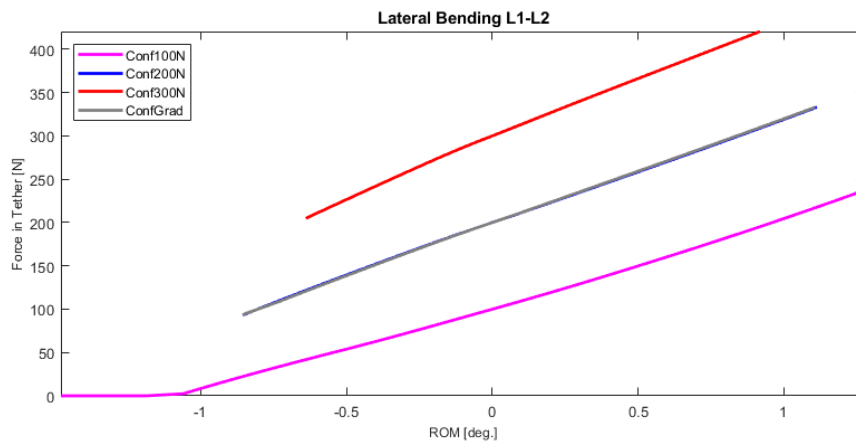
Source: Author.

Figure 77 – Tether Force-ROM curves of the T12-L1 segment of the spine in different pre-tension configurations under pure lateral bending moment loading.



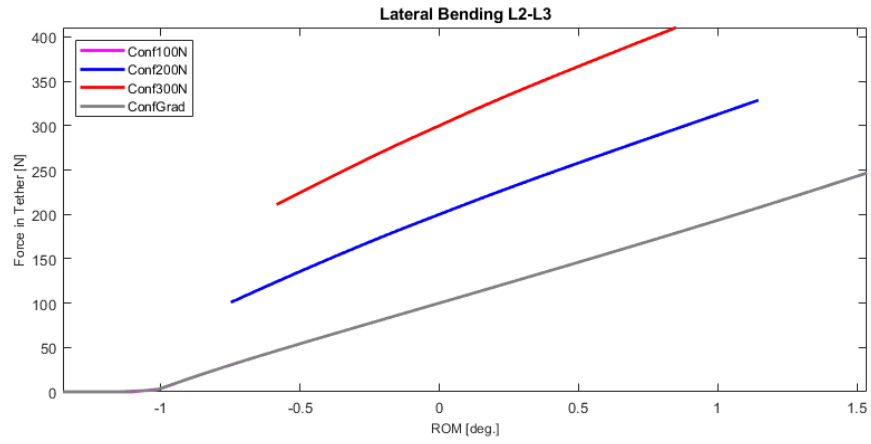
Source: Author.

Figure 78 – Tether Force-ROM curves of the L1-L2 segment of the spine in different pre-tension configurations under pure lateral bending moment loading.



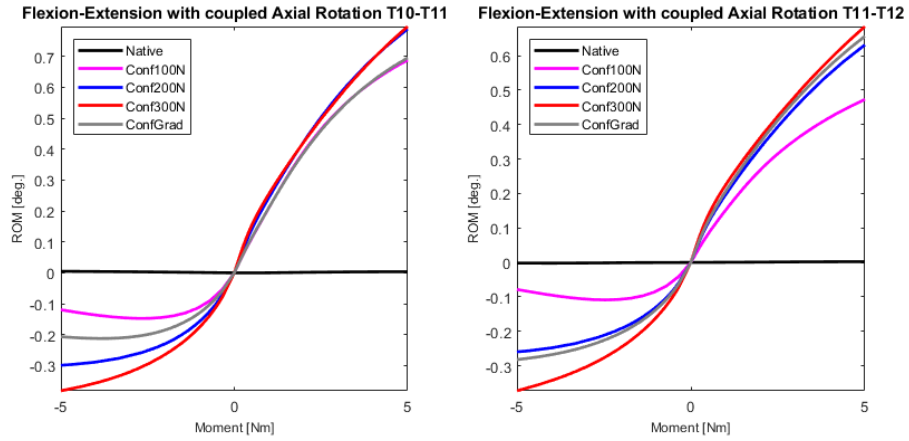
Source: Author.

Figure 79 – Tether Force-ROM curves of the L2-L3 segment of the spine in different pre-tension configurations under pure lateral bending moment loading.



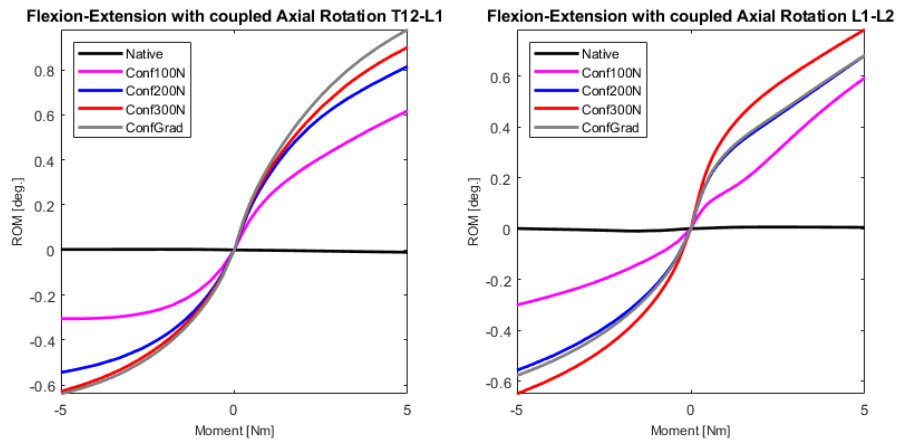
**APPENDIX D – Coupled Motion-Moment graphs of each individual segment of the spine under different pre-tension configurations**

Figure 80 – Coupled Axial Rotation Motion versus Flexion-Extension Moment curves of the T10-T11 and T11-T12 segments of the spine in different pre-tension configurations.



Source: Author.

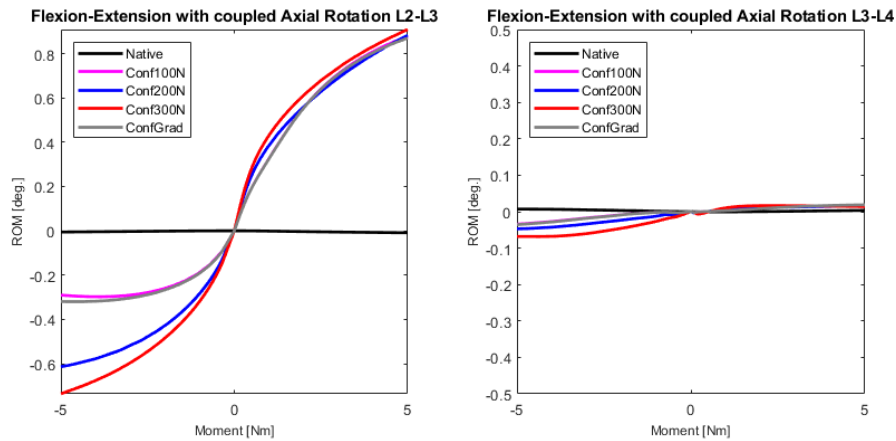
Figure 81 – Coupled Axial Rotation Motion versus Flexion-Extension Moment curves of the T12-L1 and L1-L2 segments of the spine in different pre-tension configurations.



Source: Author.

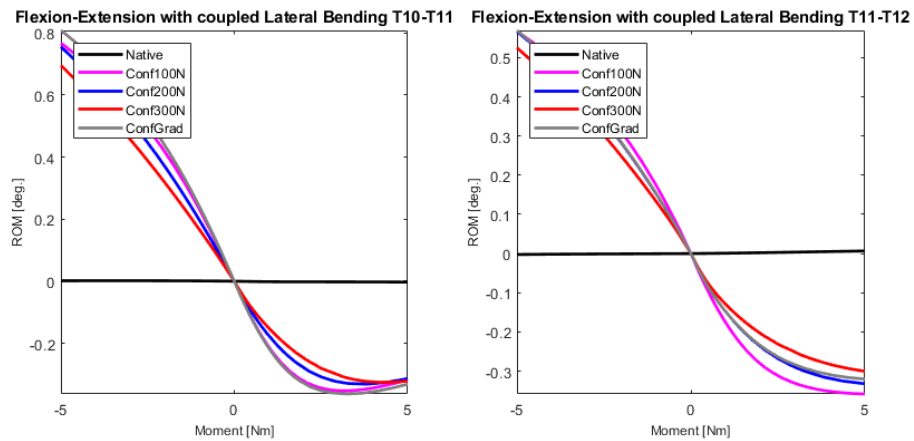


Figure 82 – Coupled Axial Rotation Motion versus Flexion-Extension Moment curves of the L2-L3 and L3-L4 segments of the spine in different pre-tension configurations.



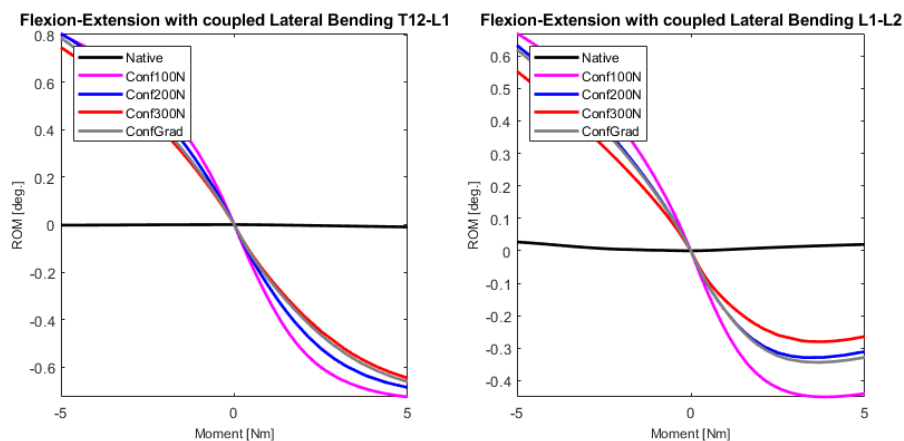
Source: Author.

Figure 83 – Coupled Lateral Bending Motion versus Flexion-Extension Moment curves of the T10-T11 and T11-T12 segments of the spine in different pre-tension configurations.



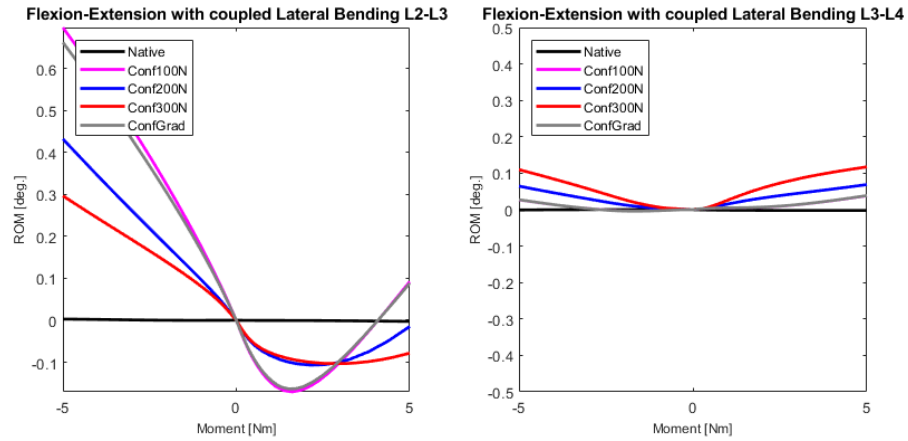
Source: Author.

Figure 84 – Coupled Lateral Bending Motion versus Flexion-Extension Moment curves of the T12-L1 and L1-L2 segments of the spine in different pre-tension configurations.



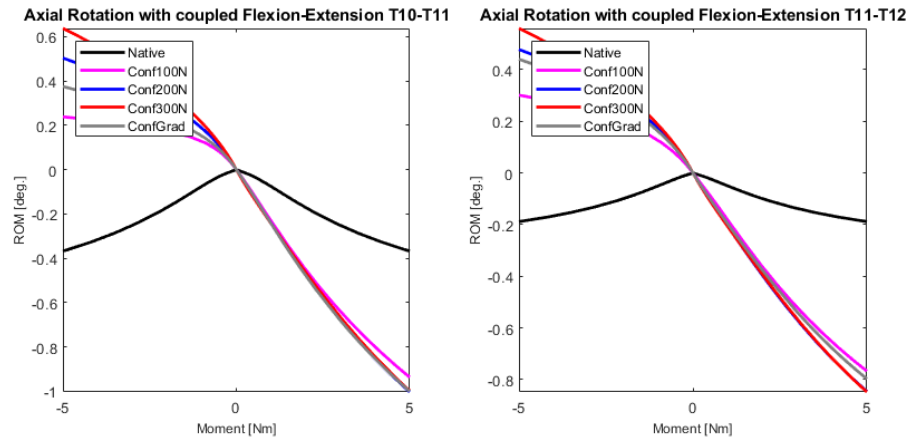
Source: Author.

Figure 85 – Coupled Lateral Bending Motion versus Flexion-Extension Moment curves of the L2-L3 and L3-L4 segments of the spine in different pre-tension configurations.



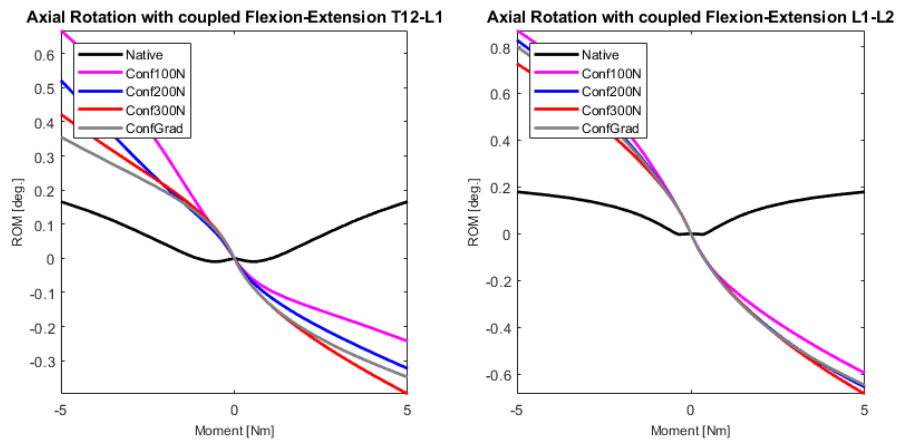
Source: Author.

Figure 86 – Coupled Flexion-Extension Motion versus Axial Rotation Moment Coupled Flexion-Extension Motion curves of the T10-T11 and T11-T12 segments of the spine in different pre-tension configurations.



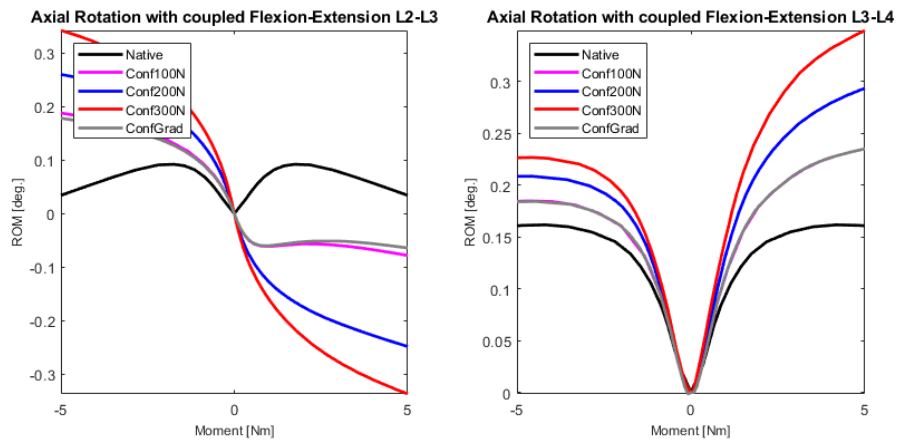
Source: Author.

Figure 87 – Coupled Flexion-Extension Motion versus Axial Rotation Moment curves of the T12-L1 and L1-L2 segments of the spine in different pre-tension configurations.



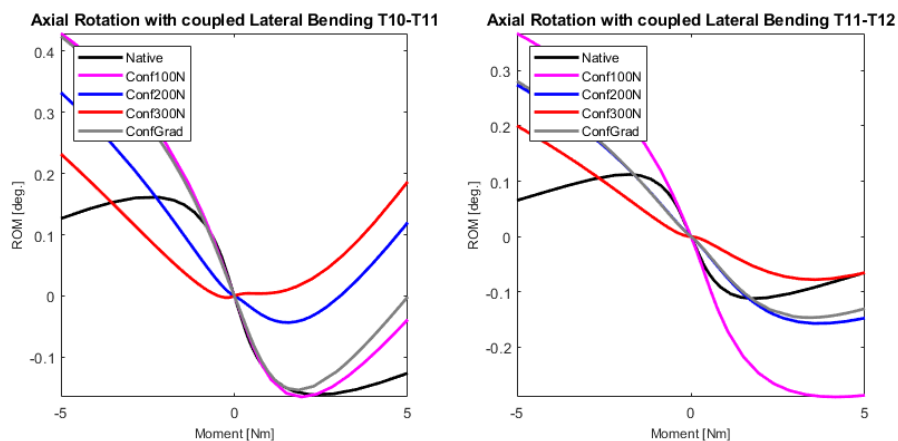
Source: Author.

Figure 88 – Coupled Flexion-Extension Motion versus Axial Rotation Moment curves of the L2-L3 and L3-L4 segments of the spine in different pre-tension configurations.



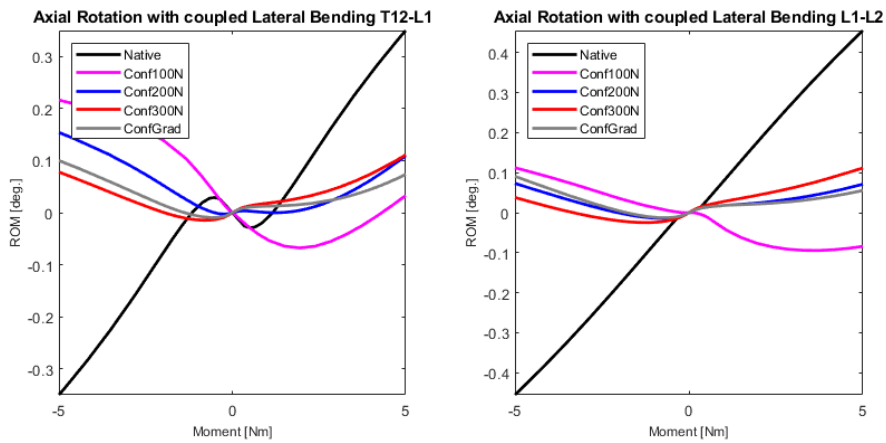
Source: Author.

Figure 89 – Coupled Lateral Bending Motion versus Axial Rotation Moment curves of the T10-T11 and T11-T12 segments of the spine in different pre-tension configurations.



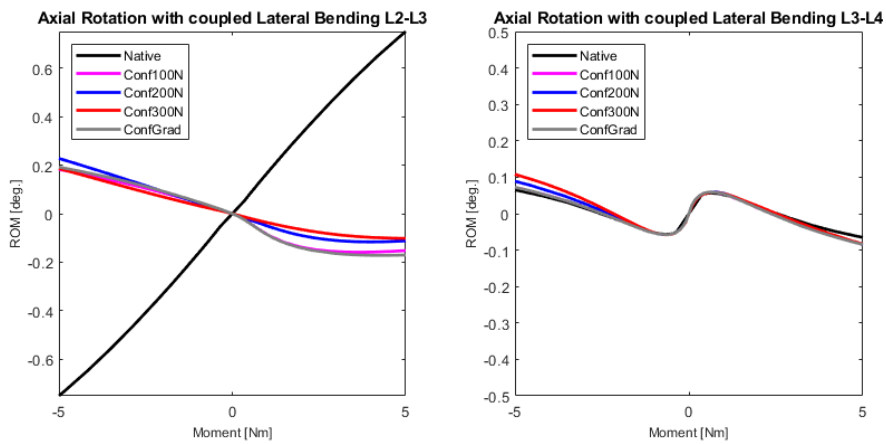
Source: Author.

Figure 90 – Coupled Lateral Bending Motion versus Axial Rotation Moment curves of the T12-L1 and L1-L2 segments of the spine in different pre-tension configurations.



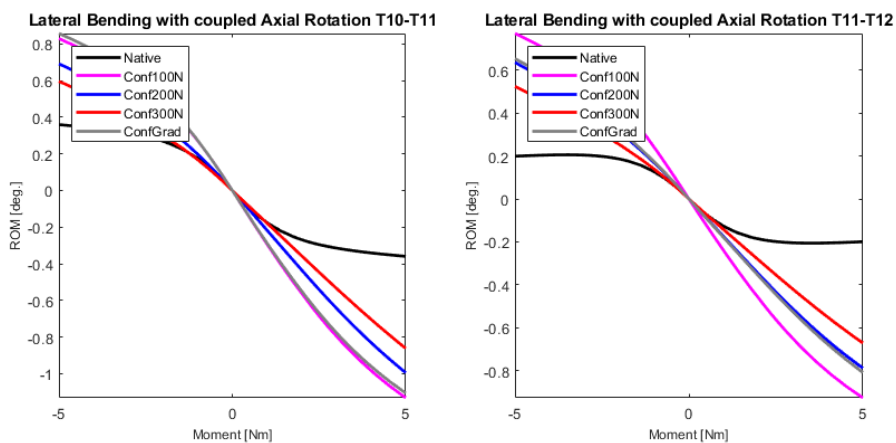
Source: Author.

Figure 91 – Coupled Lateral Bending Motion versus Axial Rotation Moment curves of the L2-L3 and L3-L4 segments of the spine in different pre-tension configurations.



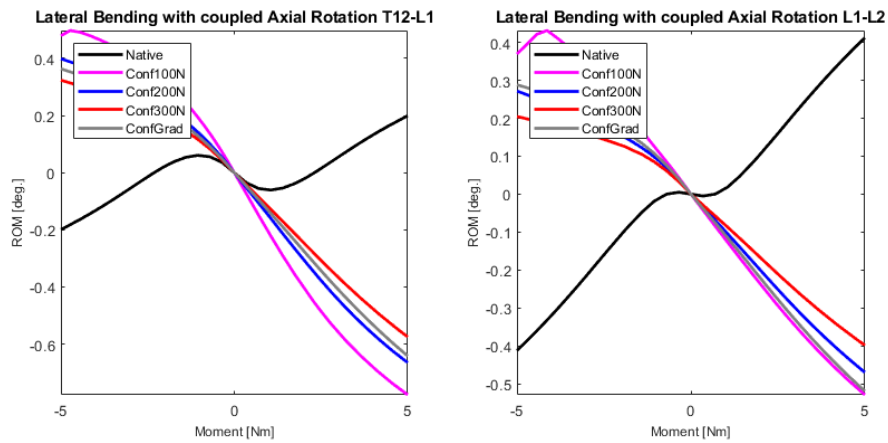
Source: Author.

Figure 92 – Coupled Axial Rotation Motion versus Lateral Bending Moment curves of the T10-T11 and T11-T12 segments of the spine in different pre-tension configurations.



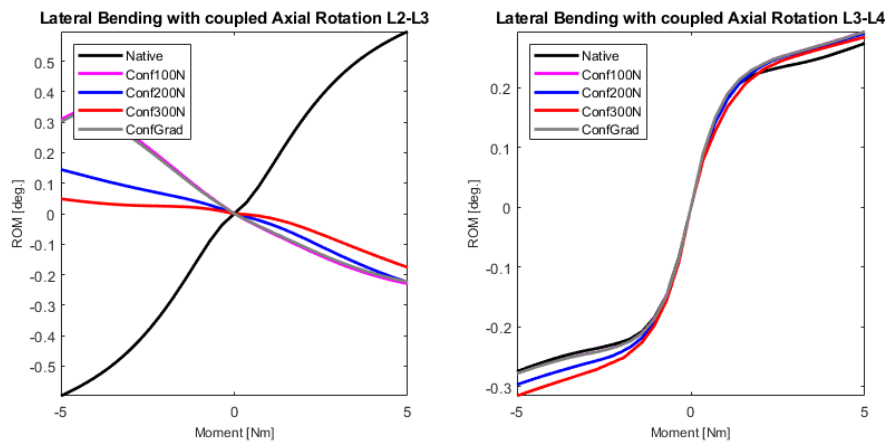
Source: Author.

Figure 93 – Coupled Axial Rotation Motion versus Lateral Bending Moment curves of the T12-L1 and L1-L2 segments of the spine in different pre-tension configurations.



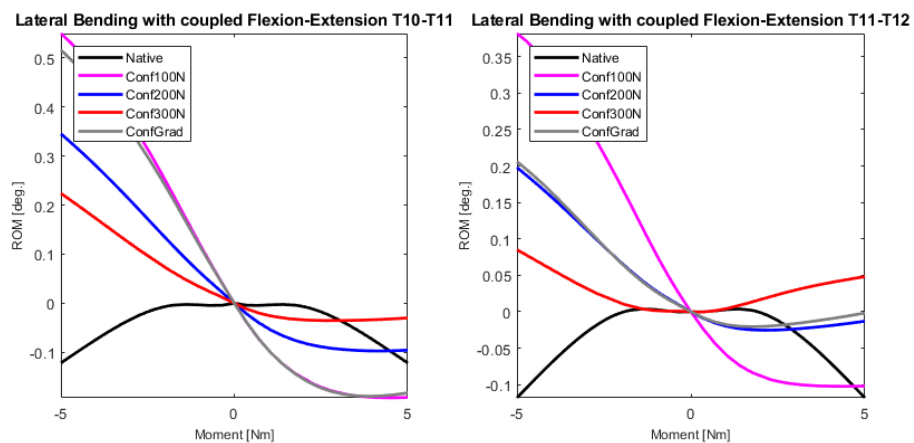
Source: Author.

Figure 94 – Coupled Axial Rotation Motion versus Lateral Bending Moment curves of the L2-L3 and L3-L4 segments of the spine in different pre-tension configurations.



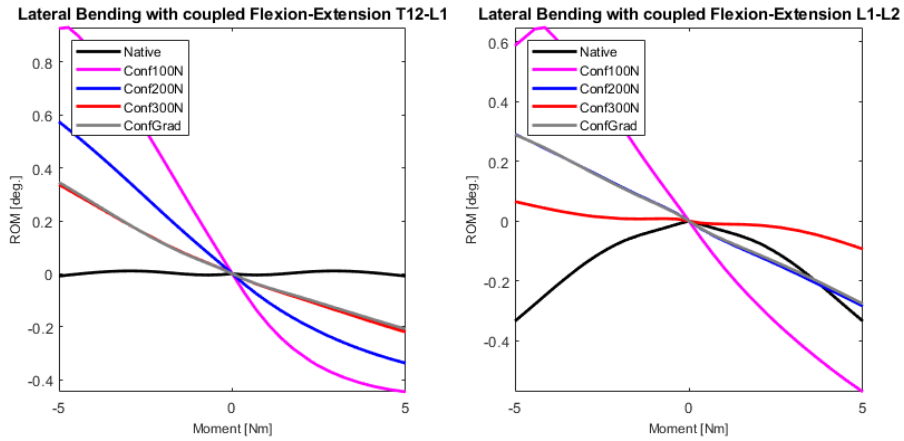
Source: Author.

Figure 95 – Coupled Flexion-Extension Motion versus Lateral Bending Moment curves of the T10-T11 and T11-T12 segments of the spine in different pre-tension configurations.



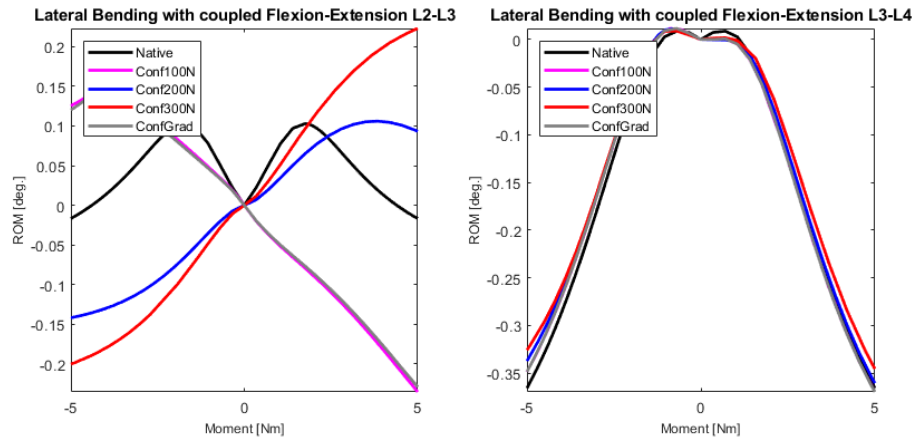
Source: Author.

Figure 96 – Coupled Flexion-Extension Motion versus Lateral Bending Moment curves of the T12-L1 and L1-L2 segments of the spine in different pre-tension configurations.



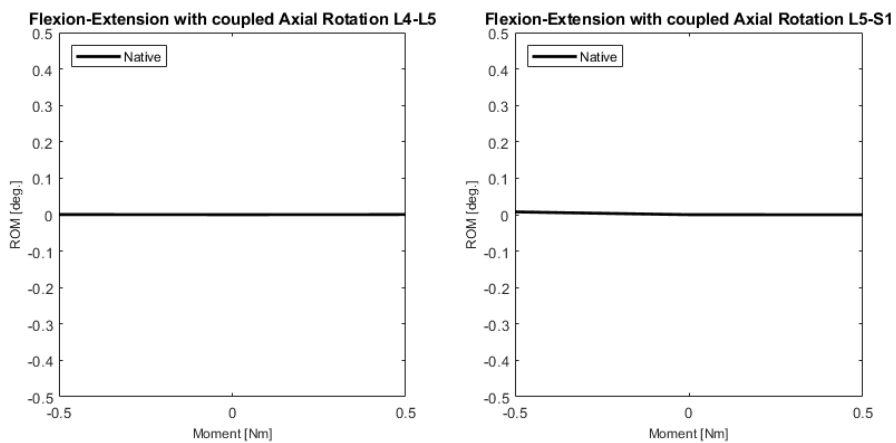
Source: Author.

Figure 97 – Coupled Flexion-Extension Motion versus Lateral Bending Moment curves of the L2-L3 and L3-L4 segments of the spine in different pre-tension configurations.



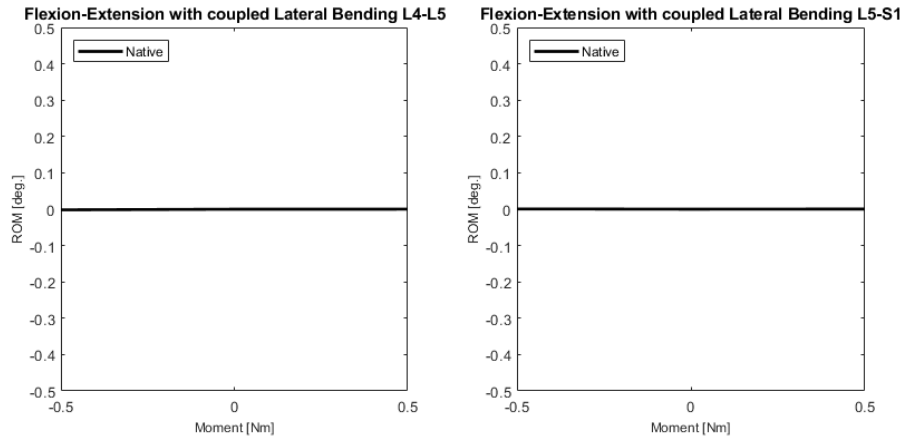
Source: Author.

Figure 98 – Coupled Axial Rotation Motion versus Flexion-Extension Moment curve of the native L4-L5 and L5-S1 segments of the spine.



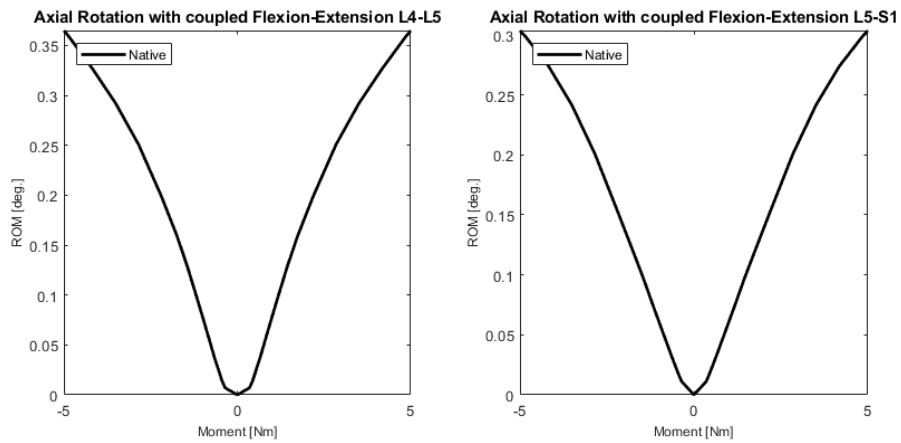
Source: Author.

Figure 99 – Coupled Lateral Bending Motion versus Flexion-Extension Moment curve of the native L4-L5 and L5-S1 segments of the spine.



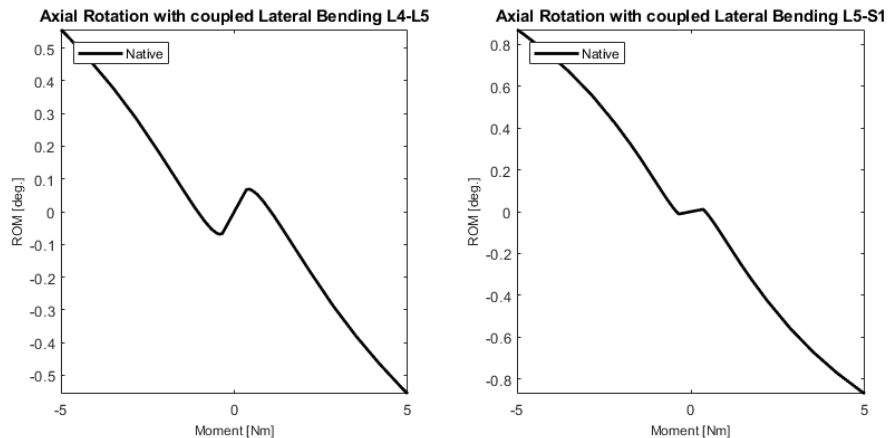
Source: Author.

Figure 100 – Coupled Flexion-Extension Motion versus Axial Rotation Moment curve of the native L4-L5 and L5-S1 segments of the spine.



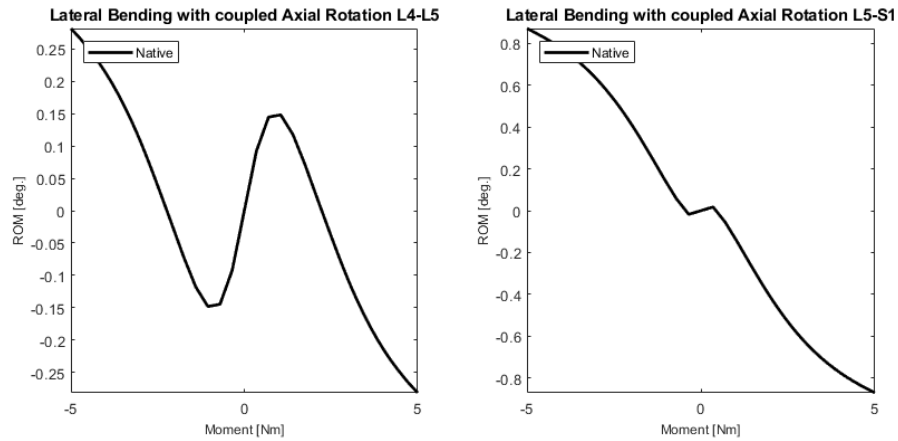
Source: Author.

Figure 101 – Coupled Lateral Bending Motion versus Axial Rotation Moment curve of the native L4-L5 and L5-S1 segments of the spine.



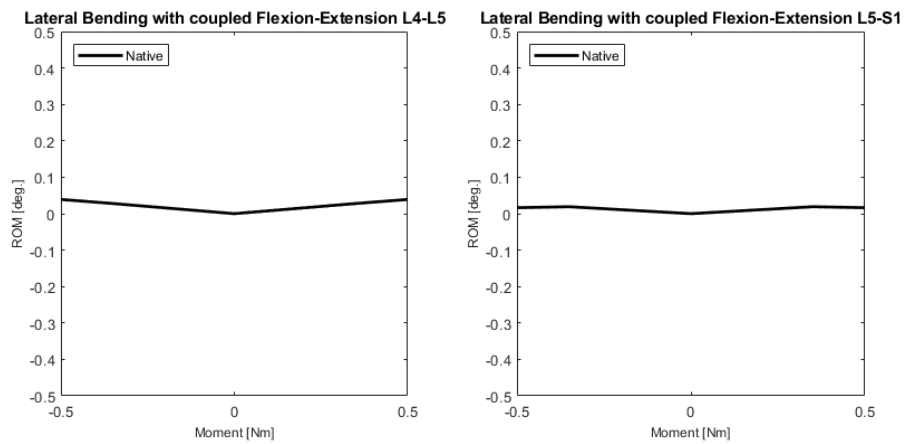
Source: Author.

Figure 102 – Coupled Axial Rotation Motion versus Lateral Bending Moment curve of the native L4-L5 and L5-S1 segments of the spine.



Source: Author.

Figure 103 – Coupled Flexion-Extension Motion versus Lateral Bending Moment curve of the native L4-L5 and L5-S1 segments of the spine.



Source: Author.